이학박사 학위논문

The Progenitor System of Type Ia Supernovae via Early-Time Observation using Small Telescope Network

폭발 초기의 소형망원경 네트워크 관측을 통해 살펴본 제 Ia형 초신성의 원형별계

2022년 08월

서울대학교 대학원
물리·천문학부 천문학전공
임 구

The Progenitor System of Type Ia Supernovae via Early-Time Observation using Small Telescope Network

폭발 초기의 소형망원경 네트워크 관측을 통해 살펴본 제 Ia형 초신성의 원형별계

지도교수 임 명 신

이 논문을 이학박사 학위논문으로 제출함
2022년 04월

서울대학교 대학원
물리·천문학부 천문학전공
임 구

임 구의 이학박사 학위논문을 인준함
2022년 06월

위 원 장 ______________________________

부 위 원 장 ______________________________

위 원 ______________________________

위 원 ______________________________

위 원 ______________________________

The Progenitor System of Type Ia Supernovae via Early-Time Observation using Small Telescope Network

by

Gu Lim
(lim9gu@snu.ac.kr)

A dissertation submitted in partial fulfillment of the requirements for
the degree of

Doctor of Philosophy

in
Astronomy

in
Astronomy Program
Department of Physics and Astronomy
Seoul National University

Committee:

Professor	Sung-Chul Yoon
Professor	Myungshin Im
Professor	Hyung Mok Lee
Professor	Soojong Pak
Professor	Hee-won Lee

ABSTRACT

Type Ia supernovae (SNe Ia) are the explosion at the final stage of stellar evolution. The progenitor star is believed to be a white dwarf (WD) and its light curve rises from the carbon ignition of WD (Thermonuclear runaway), forming heavy elements. These elements enrich their environments and contribute to star formation and galaxy evolution. Especially, SNe Ia plays an important role in measuring extragalactic distance as a good candidate for a standard candle. However, the progenitor system of SNe Ia is still in debate: a system of WD primary and non-degenerate companion (single degenerate; SD) or a WD binary (double degenerate; DD). One way to constrain them is to detect the signature of shock-heated cooling emission predicted from the collision between SN ejecta and the companion star in the early light curve. Intensive Monitoring Survey of Nearby Galaxies (IMSNG) program has been performed by us to catch this predicted feature with a high cadence (within a day) using a small telescope network. In this thesis work, we establish an additional telescope to improve this system. Among the early observational data of SNe in IMSNG, we present the results of early light curve analysis of two Type Ia supernovae, 2019ein and 2021hpr.

First, we introduce the 0.36-m automated system of the KIAS Chamnun Telescope (KCT), installed at DeepSkyChile in Chile in 2020 March. KCT aims to perform time-series observation mainly focused on transient objects under the dark sky in Chile and improve synergy with other telescopes around the world. Here, we present the basic characteristics of the system, automated operation, performances, and plans. KCT uses a public software of ACP Observatory Control Panel (ACP) that performs scheduled observations based on the script ("Observing plan") uploaded by a user in its scheduling dispatcher. In the imaging data, we find uniform PSFs but slightly elongated over the field of view, and no shutter pattern in very short exposures. In addition, a 5σ limiting magnitude of $g = 18.9\,\mathrm{AB}$ mag for a point source with 10 minutes of integrated exposures in the clear sky affected by a small amount of the moonlight and the seeing condition of $3''.0$. The operation of the KCT system will be improved to deal with future rapid transient follow-up programs via customization of the observing plans.

Second, we present a high cadence optical/Near-IR light curve of normal but slightly faint type Ia SN 2019ein from the IMSNG program. We fit the early light curve ($t <$ $+8.3$ days from the first detection) with various models to find the shock-heated cooling emission from SN ejecta-companion interaction. No significant shock-heated cooling emission is found, from which we constrain the progenitor star size as the following.The upper limit ($R_{\mathrm{upper},*}$) of the companion size in R-band is $\sim 0.2\,R_{\odot}$ when forcing the first light time (t_{fl}) to have one value and $\sim 0.9\,R_{\odot}$ when using the mean value of t_{fl} from the fitting in each band. These results allow us to at least rule out large stars like red giants as a companion star of WD of this supernova. $B-R$ and $V-R$ color do not show any significant signs of a red bump, which is not explained by a sub-M_{ch} with a thin helium shell ($M_{\mathrm{He}} < 0.01\,M_{\odot}$) (double detonation model). In addition, we estimated the distance to NGC 5353 as 37.098 ± 0.028 Mpc.

Third, we present a high-cadence monitoring observation of SN 2021hpr in a spiral galaxy, NGC 3147. SN 2021hpr shows typical characteristics as a normal type Ia supernova from its photometric ($\Delta m_{15}(B) = 0.98 \pm 0.03$, dust-free $M_{\mathrm{B,max}} = -19.56 \pm 0.11$) and spectroscopic data. We found a significant feature of "an early excess" on the light curve and its blue color. To explain this, we fit the early part of $BVRI$-band light curves simultaneously with a two-component model of the ejecta-companion interaction and a simple power-law model. As a result, the companion model can explain this feature with the reduced chi-square (χ^2_{ν}) of 2.3 giving us the companion radius of $5.95 \pm 0.35\,R_{\odot}$ assuming the optimal viewing angle. Compared to a recent Hubble Space Telescope (HST) detection image of SN 2021hpr, we could not detect possible progenitor candidates in the HST pre-explosion imaging, but the detection limit excludes massive stars with an initial mass $M_{\mathrm{init}} > 12\,M_{\odot}$. However, we could not find any signs of the stripped mass ($\lesssim 0.002\,M_{\odot}$ for Hα emission) from the companion star predicted in the SD system, being contradictory with the early light curve fitting. We discuss this discrepancy with the SD system in large binary separation, leaving the possibility of other progenitor scenarios. This indicates SN 2021hpr is a good sample to verify various progenitor scenarios of Type Ia supernovae.

In conclusion, we found that high-cadence observation using small telescopes is a powerful way to study the early light curves of SNe Ia. Early light curves from the IMSNG program provide us with observational evidence to rule out some of the currently suggested models of the progenitor system of SNe Ia, but our results also suggest possible multiple origins.

Keywords: galaxies: distances and redshifts – supernovae: general – supernovae: individual (SN 2019ein) – supernovae: individual (SN 2021hpr) – methods: observational – telescopes – techniques: photometric

Student Number: 2015-20364

Contents

List of Figures

List of Tables

Chapter 1

Introduction

1.1 Supernovae (SNe)

Supernovae (SNe) are one of the most explosive transient events in the sky. The explosion occurs when massive energy is released in the final stage of stellar evolution. Generally, its luminosity is as bright as a galaxy that hosts the supernova (Total kinetic energy of $E_k = 10^{51}\,\mathrm{ergs} = 1\,\mathrm{Bethe}{=}1\,\mathrm{B}$; Branch & Wheeler 2017). Figure 1 shows the emergence of a Type Ia supernova 2014J in a nearby galaxy M82. The term "Supernovae" is referred to objects brighter than classical novae that originated from the thermonuclear reaction on the surface of the white dwarf in a close binary system.

We can understand many aspects of modern astronomy by studying supernovae. They give us clues to the nature of the physical mechanisms. We can ask ourselves: What induces this tremendous explosion? Many studies have revealed that some supernovae are originated from the gravitational collapse of a single massive star such as a red super-giant and Wolf-Rayet star, or thermonuclear runaway of a white dwarf in a close binary system. In addition, since the stellar interior is not visible from the outside, we can examine the pathway of stellar evolution when the ejecta expands away. The ejecta also sweeps the interstellar medium (ISM) away and injects the energy. Heavy elements (Higher atom number than helium in the periodic table) are synthesized during explosion and enrich the ambiance of its progenitor system, and stimulate

Figure 1.1. Hubble Space Telescope (HST) image of the Type Ia supernova 2014J in M82 adopted from Foley et al. (2014).

star formation, leading to the chemical evolution of their host galaxies. These heavy elements are included in molecular clouds and they become ingredients forming stellar/planetary systems, and even contribute to life evolution. Lastly, since supernovae are very luminous, they can be used as cosmic distance indicators to distant objects. Distance measurements of high redshift (z) type Ia supernovae support the accelerating expansion of the universe and the presence of dark energy.

1.1.1 Classification of SNe

Supernovae are, in the early times, classified as Type I with Hα emission line and Type II without it (Minkowski 1941). Figure 2 summarizes the supernovae classification. This basic classification became a basis for the classification in the modern era including other distinct sub-classes. Among Type I supernovae, some with strong silicon broad lines (Si II) near 6100 Å are divided into Type Ia supernovae (SNe Ia), but other populations showing no or weak features of Si II have neutral helium emissions He I, now called Type Ib supernovae (SNe Ib). Those without distinctive He I feature are known as Type Ic supernovae (SNe Ic)*. Type II supernovae show many differences in the observable quantities in both the light curve and the spectrum. Type IIP supernovae (SNe IIP) show a flat light curve after the first maximum brightness (Plateau) than a linear feature of Type IIL supernovae (SNe IIL). In addition, Type IIn supernovae (SNe IIn) are "narrow-lined" on their spectrum, which is originated from the interaction with CSM. Type IIb supernovae (SNe IIb) show transitional behavior from SNe II with hydrogen features to SN Ib with strong helium lines and no hydrogen. We often refer to SN Ib/c and SN IIb as stripped-envelope supernovae since helium features come into view after the H-rich envelope is stripped. One of the most spectacular views of the supernovae is SN 1987A due to its proximity to the Earth. SN 1987A shows a sub-luminous and peculiar shape of the light curve but it has a strong hydrogen feature in its spectrum (SN II-pec in Figure 3). Since the progenitor system of SNe Ib/c and SNe II is known to be resulted from a single massive star, they are also collectively called core-collapse supernovae (CCSNe) while SNe Ia are referred to as thermonuclear supernovae. In this thesis work, we are going to focus on SNe Ia.

1.2 Type Ia supernovae

1.2.1 Observational Properties in the Light Curve

Many observations support the progenitor star of Type Ia supernovae originated from a low-mass star. First, there are no hydrogen and helium emissions in their spectra, suggesting that its envelope is stripped off. In addition, some of SNe Ia show carbon and oxygen absorption from the unburned matter in the pre-maximum spectra. Second, SNe Ia are discovered in both late-type and early-type galaxies. Since the stars in early-type galaxies consumed most of their fuels for star formation, low mass stars with long lifetimes are the dominant population. Therefore, a thermonuclear explosion of a degenerate stellar core, a white dwarf, is suggested by Hoyle & Fowler (1960). Third, it is known that a white dwarf exceeding the Chandrasekhar mass ($M_{\mathrm{ch}} \sim 1.4\,M_{\odot}$)

---

[*] We refer SNe Ib and SNe Ic to SNe Ib/c

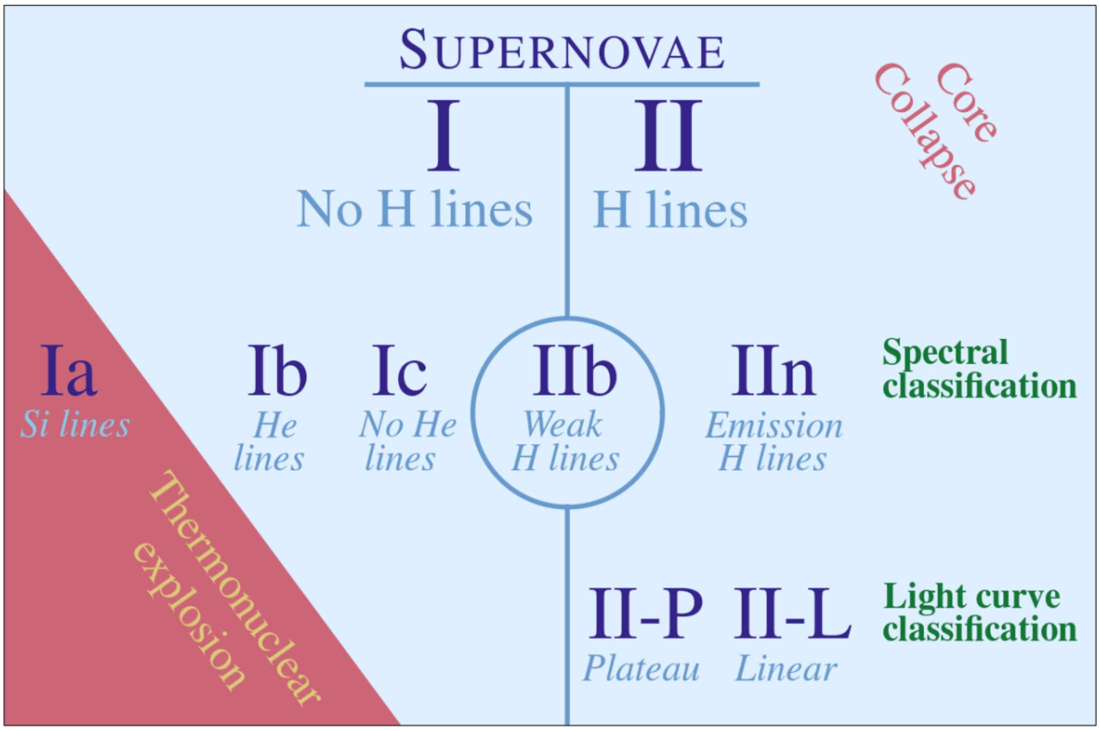

Figure 1.2. A schematic classification of supernovae adopted by Pruzhinskaya & Lisakov (2016).

explodes producing energy of $\sim 10^{51}$ergs that agrees with the observation.

The light curve of a SN Ia is directly related to the physical properties such as the total mass of ejecta, the mass of synthesized radioactive elements (Iron group elements). Using carbon and oxygen as fuel, the unstable ^{56}Ni is produced. Next, ^{56}Ni decays to ^{56}Co with a short half-life time of 6.1 days, and it finally decays to stable ^{56}Fe (77 days). The light curve is primarily powered by ^{56}Ni decay.

Generally we observe SNe Ia through standard filters. Figure 4 shows the light curves of some typical (or 'normal') SNe Ia observed in multiple filters. For a typical SN Ia, its light curve generally rises in ~ 20 days (Jha et al. 2019). The peak brightness is approximately ~ -19.4 AB mag in B-band, then it declines 1.1 magnitudes in 15 days in B-band, which is suggested as a decline rate or $\Delta\, m_{15}(B)$ by (Phillips 1993), until an exponential decay is shown after ~50 days. The longer the wavelength is observed,

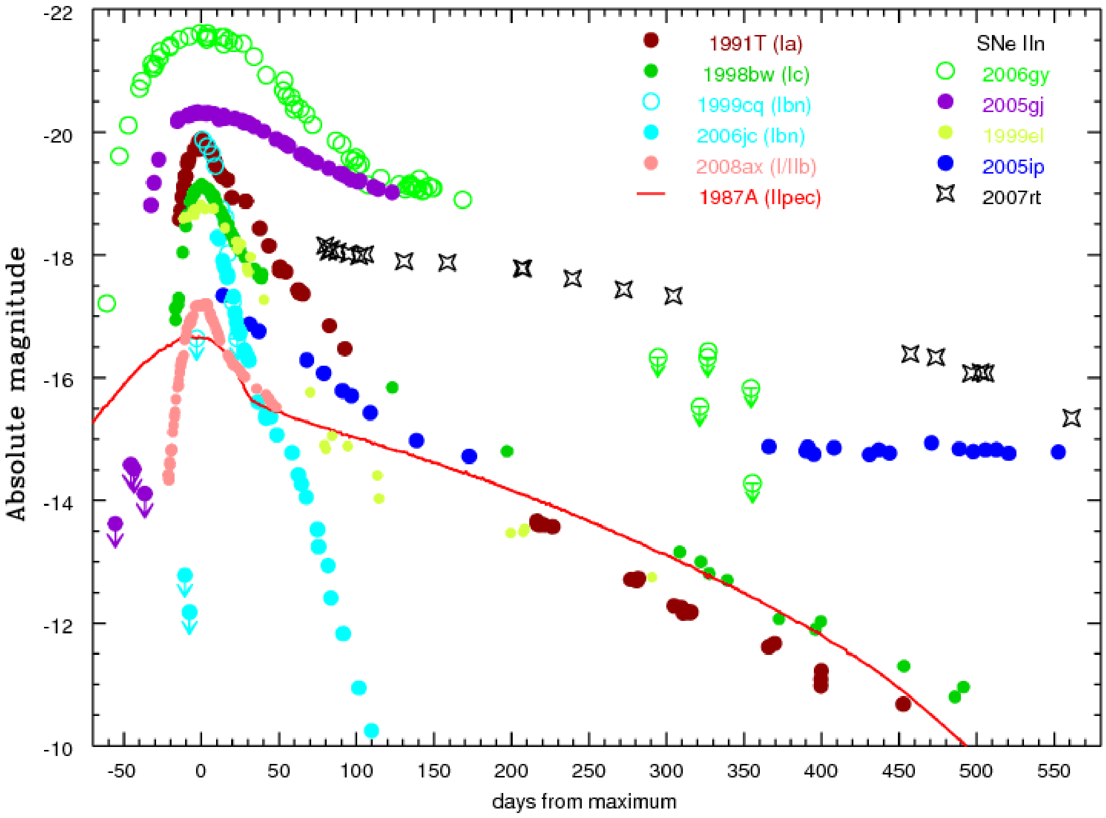

Figure 1.3. Light curves of many types of supernovae adopted by Trundle et al. (2009).

the more distinct the shape of the secondary peak (shoulder) becomes. The shape of light curves are remarkably homogeneous for typical SNe Ia. The uniformity of the light curves has given many researchers' attention to the possibility that SNe Ia can be used as cosmological standardizable candles.

However, this expectation was challenged by a discovery of peculiar supernovae (91bg-like SNe) with a peak luminosity fainter than that of normal supernovae and a contamination of host galaxies in SNe photometry (Boisseau & Wheeler 1991). Furthermore, Phillips (1993) found the empirical correlation between the absolute magnitude and the decline rate of SNe Ia samples with well-determined distance to their host galaxies (Phillips relation), showing flatter slopes in filters at the longer wavelengths which is affected by the reddening of Milky way and host galaxy. This motivated Phillips et al. (1999) to establish the reddening-free relation between the peak absolute magnitude

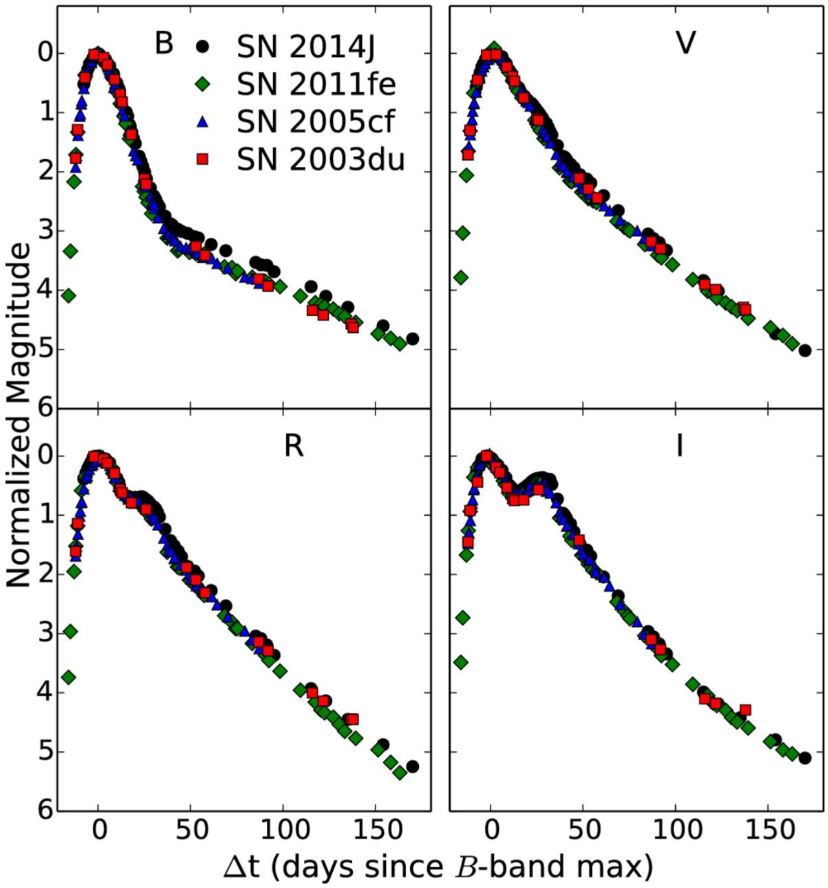

Figure 1.4. The light curve of SN 2014J is significantly similar to 3 other normal SNe Ia (SN 2011fe, SN 2005cf, SN 2003du) adopted from (Srivastav et al. 2016).

and the B-band decline rate as a method to determine the host galaxy reddening using samples of "un-reddened" SNe Ia (The top panel of Figure 5). The advantage of this method is that we do not need to obtain $(B-V)$ color curves ranging from $30-90$ days at post-peak (Lira's relation; The bottom of Figure 5), while the observation only at peak and 15 days since the peak is required for $(B_{\max}-V_{\max})$ and the decline rate.

The bolometric light curve, which intensity is integrated with all wavelengths, is used to estimated the ejecta and nickel mass. Typically the pseudo (or quasi)-bolometric light curve such as the UVOIR light curve (filters from ultraviolet to infrared) is obtained. The peak luminosity reaches to $\sim 1.5\times10^{45}\,\mathrm{erg\,s^{-1}}$, which is corresponding to $M_{\rm Ni}=0.7\,M_{\odot}$.

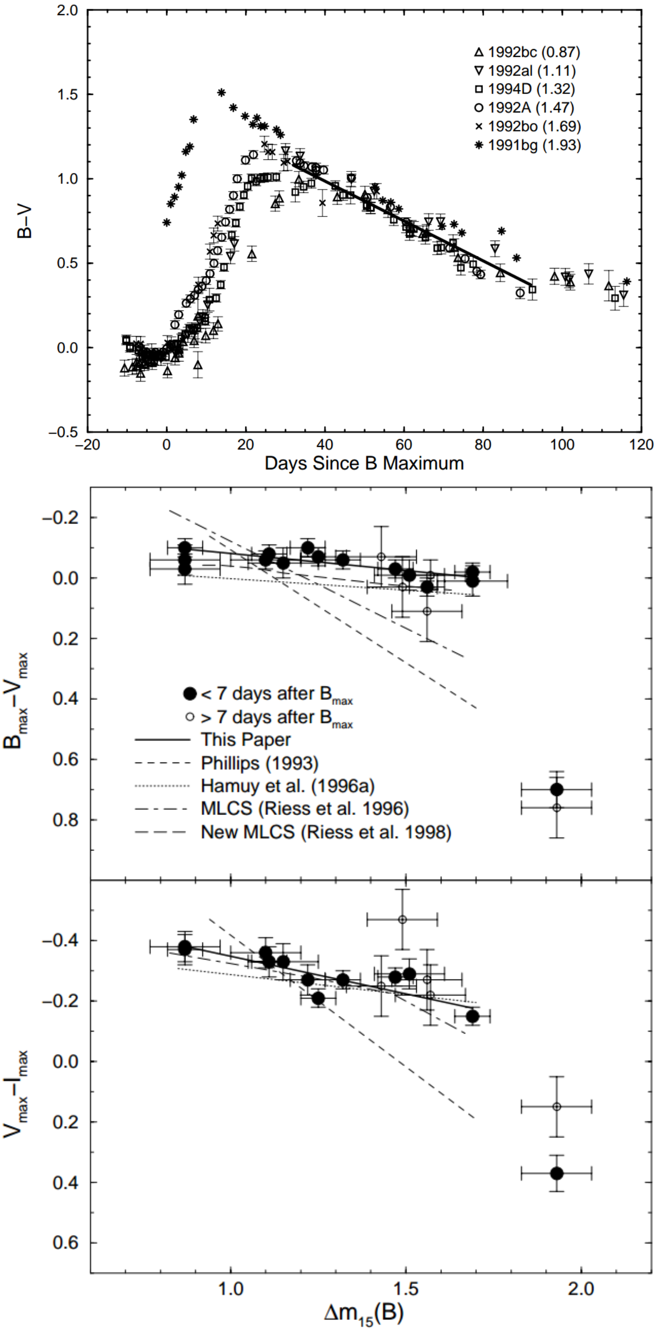

Figure 1.5. (Top) The Lira's relation described in Phillips et al. (1999). (Bottom) The Phillips relation established by Phillips et al. (1999) for the host reddening estimation.

1.2.2 Diversity of thermonuclear supernovae

Many different sub-types of SNe Ia have been discovered. Their increasing observational data show the diversity of SNe Ia. They result from different evolutionary paths. We encounter the issue of a relation between these diverse evolutionary paths and many sub-classes of SNe Ia. Figure 6 summarizes the diversity of SNe Ia in the plane of the B-band decline rate (width) and the peak absolute B magnitude. Normal SNe Ia follow the Phillips relation, but there are many outliers on the side of slowly-declining over-luminous 91T-like SNe and fast-declining sub-luminous 91bg-like SNe. SNe Iax have typically low luminosity and they are typically discovered in star-forming galaxies. Especially the blue progenitor system of SN 2012Z (SN Iax) was detected in the pre-explosion Hubble Space Telescope image, suggesting a possible helium companion star (McCully et al. 2014). 02es-like SNe are similar to SNe Iax but they are relatively slowly decliners. Other extremes include luminous super-Chandrasekhar SNe Ia, SNe Ia with CSM interaction features (SNe Ia-CSM), and Ca-rich transients.

1.3 Progenitor Scenarios

Many studies support the progenitor star of Type Ia supernovae is a thermonuclear explosion of C/O white dwarf, which mass ($M_{\rm WD}$) approaches or exceeds the critical mass limit, or Chandrasekhar mass ($M_{\rm ch} \sim 1.4\,M_\odot$). However, it is not easy for a single white dwarf star to explode. A single massive star would evolve to SN II or neutron star (NS), or black hole (BH). So a carbon/oxygen white dwarf (CO WD) in a close binary system can be a possible solution to the explosion. Researchers have given efforts to explain how this explosion occurs in this binary system. Proposed progenitor scenarios are largely divided into the single degenerate (SD) scenario and the double degenerate (DD) scenario. Figure 7 summarizes the detailed description.

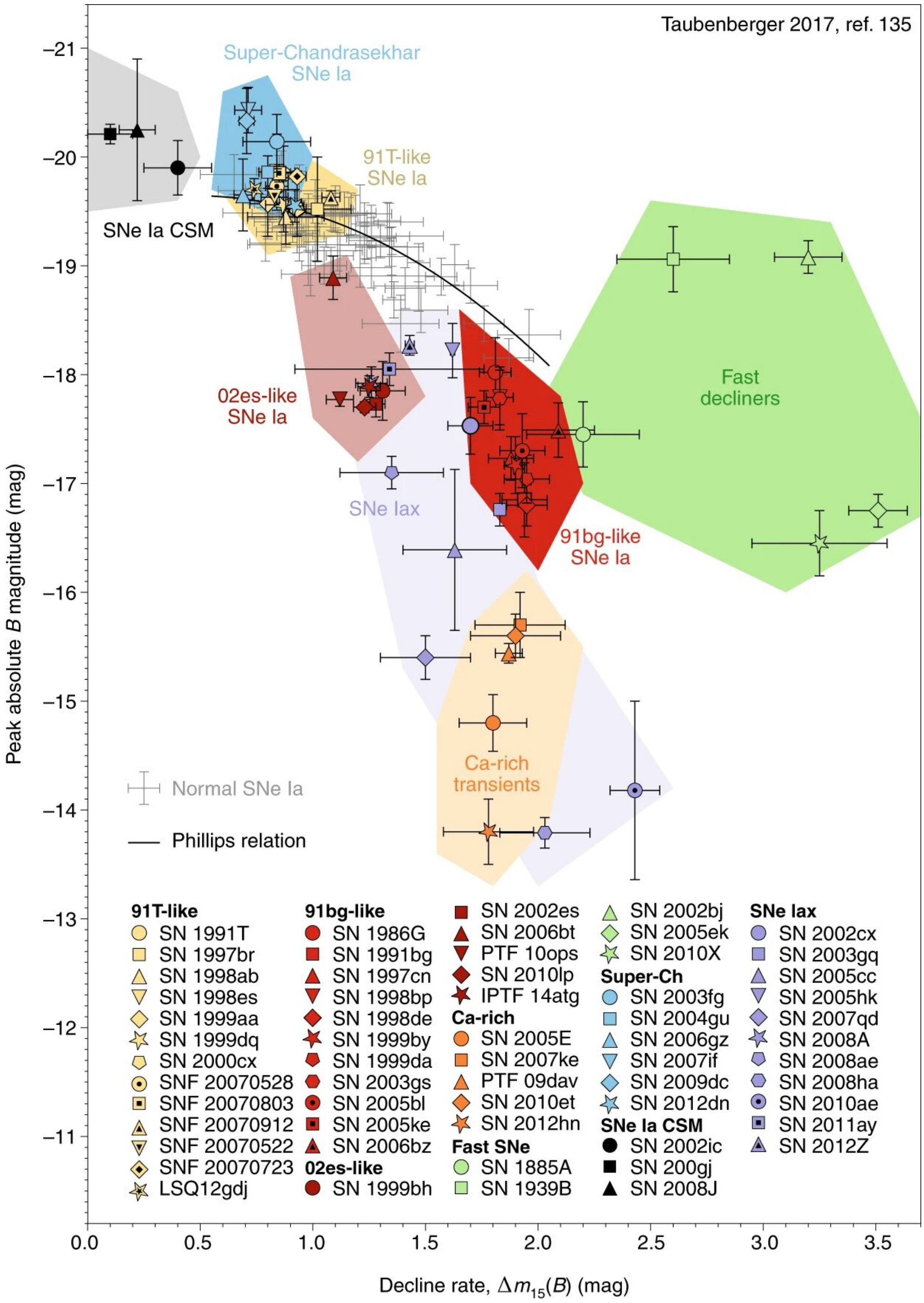

Figure 1.6. The parametric plane of B-band decline rate versus the peak luminosity of diverse SNe Ia adopted from Jha et al. (2019).

1.3.1 Single Degenerate (SD) Scenario

In the SD scenario, it is important for a primary WD to gain its mass from the non-degenerate companions such as a main-sequence (MS; $1 - 2\,M_{\odot}$ Pakmor et al. 2008; Liu et al. 2012) or a sub-giant (SG; $2\,M_{\odot}$ Han & Podsiadlowski 2004), or a low mass red-giant (RG; $\sim 1\,M_{\odot}$ Whelan & Iben 1973; Hachisu et al. 1999), or a helium star (He star; $1.0 - 2.5\,M_{\odot}$ Nomoto 1982). The primary WD grows its mass up to $\sim 1.4\,M_{\odot}$ from the mass accretion transferred from Roche-lobe overflow (Roche-lobe overflow channel; RLOC) or through a strong stellar wind from the companion.

For the stable H-burning on the surface of the WD, a certain range of the accretion rate is required. For example, $\sim 10^{-7}\,M_{\odot}\,\mathrm{yr}^{-1}$ for a WD with $M_{\mathrm{WD}} = 0.8\,M_{\odot}$ whereas $\sim 10^{-5}\,M_{\odot}\,\mathrm{yr}^{-1}$ for $M_{\mathrm{WD}} \sim M_{\mathrm{ch}}$ (Maoz et al. 2014). An accretion rate below this range would lead the binary system to occur a nova eruption. With a higher rate of the accretion beyond this range, it is shown the binary system enters a common-envelope (CE) stage, not leading to an SN Ia explosion but it is also predicted that, when the donor star has a deep convective envelope, the strong stellar wind can stabilize the mass transfer (Hachisu et al. 1996).

When a CO WD reaches almost the Chandrasekhar mass, a thermonuclear reaction occurs rapidly from the center of the carbon core. The way to ignite up the interior of WD has been theorized by many studies. Pure detonation or deflagration (The burning front proceeds in a velocity of supersonic or sub-sonic, respectively) are suggested at early times but they had some issues, such as the amount of Fe-peak elements (Too much or not enough; Arnett 1969; Nomoto et al. 1976). To resolve these issues, the deflagration to detonation (or Deflagration-to-detonation transition; DDT) model is proposed as a 1-dimensional simulation by Khokhlov (1991). The DDT model demonstrates that deflagration changes to detonation at the point where the density reaches the critical density. This model also has been studied in 2D and 3D simulations. If the transition is failed, the energy is not enough to unbind the whole WD, leaving a compact remnant so-called ‘failed-deflagration’ scenario.

It has also been studied that the SD system with a helium donor can produce SNe

Ia. A helium shell accumulated around the WD is unstable leading to detonation. The shock wave induced by the detonation converges into the center or off-center of the WD core depending on the assumption of a spherical symmetric shock wave or not (Woosley & Weaver 1994). This helium detonation causes the secondary detonation of the carbon core (Double detonation; DDet) in two different ways of the “edge-lit” that the shock hits the core directly (“direct-drive” or “prompt detonation”) or the “delayed” that detonation occurs with some delays. (Woosley et al. 1986; Fink et al. 2007, 2010). Many simulation studies have investigated how supernova explosions occur in the DDet frame, varying the mass of white dwarfs and helium shells (M_{He}). The recent results found that secondary detonation can also occur in various ranges of M_{WD} and M_{He} (Fink et al. 2007; Polin et al. 2019), even in a very small amount of helium shell (Fink et al. 2010). M_{WD} do not need to be beyond the Chandrasekhar mass so this model is so-called the “sub-Chandrasekhar double detonation scenario”.

The “spin-up/down scenario” describes that a WD can grow beyond the Chandrasekhar mass at a high accretion rate (Yoon & Langer 2005; Hachisu et al. 2012). As the accretion rate decreases, angular momentum is also lost, density and temperature increase inside the WD, and carbon ignition suddenly begins. This model is suggested to explain the super-Chandrasekhar SNe Ia.

1.3.2 Double Degenerate (DD) Scenario

In the DD scenario, the idea is basically that an SN Ia is produced by the collision of a close binary of two WDs with the gravitational wave emission losing their angular momentum (Iben & Tutukov 1984). There have been various combinations of the mass of two WDs, and the delay time[†] producing diverse explosions.

The classical DD system requires the total mass of the binary is over M_{ch} (Webbink 1984). More massive WD tidally disrupts the other less massive WD accreting its materials at a high rate. However, this model has the issue that its high accretion rate would not lead to detonation of the merged WD but would form a ONeMg WD of

---

[†] A timescale from the binary formation to the collision

near-$M_{\rm ch}$. The ONeMg WD collapses via electron capture into a single neutron star (Saio & Nomoto 1985). However, this can also lead to an SN Ia explosion avoiding off-center carbon deflagration (Yoon et al. 2007).

Next, the "violent merger" scenario is proposed as an alternative scenario. The simulation of Pakmor et al. (2010) found that a binary system of two equal-mass WDs (the mass ratio $= 1$; $0.89\,M_\odot$) can interact violently and disrupt one of the two WDs, leading to a sub-luminous SN Ia. In the subsequent study of Pakmor et al. (2011), a nearly equal-mass WD binary (the mass ratio $= 0.8 - 1.0$) can be exploded as a sub-luminous SN Ia. A normal SN Ia can also be reproduced in the DD scenario ($0.9\,M_\odot$ & $1.1\,M_\odot$; Pakmor et al. 2012). Even the merger of two WDs with thin helium shell ($M_{\rm He} = 0.01\,M_\odot$) can explain light curves of both normal and fast decling SNe Ia (Pakmor et al. 2013).

Another scenario is proposed such as a nearly head-on collision of the two WDs in a triplet system (Kushnir et al. 2013). WD collisions are known to be relatively frequent in the dense environment such as a globular cluster (Aznar-Siguán et al. 2013).

1.4 Observational constraints

There have been many observational efforts to explain the proposed progenitor system of SNe Ia so far because both the SD and DD scenarios have aspects that cannot explain all of the observational properties of SNe Ia. To distinguish and examine which scenario is prevalent, observational studies especially focus on searching for the signatures of the progenitor system, especially a companion star.

1.4.1 Direct pre/post-SN imaging of the companion star

The most direct method to solve the progenitor system issue is to detect a companion star in pre/post-supernova images. This way requires deep and high spatial resolution images, so studies are limited to very close SNe Ia. There are some examples: two normal SNe of 2011fe in M101 (Li et al. 2011), 2014J in M82 (Kelly et al. 2014), and an SN Iax 2012Z in NGC 1309 (McCully et al. 2014). For normal SN Ia,

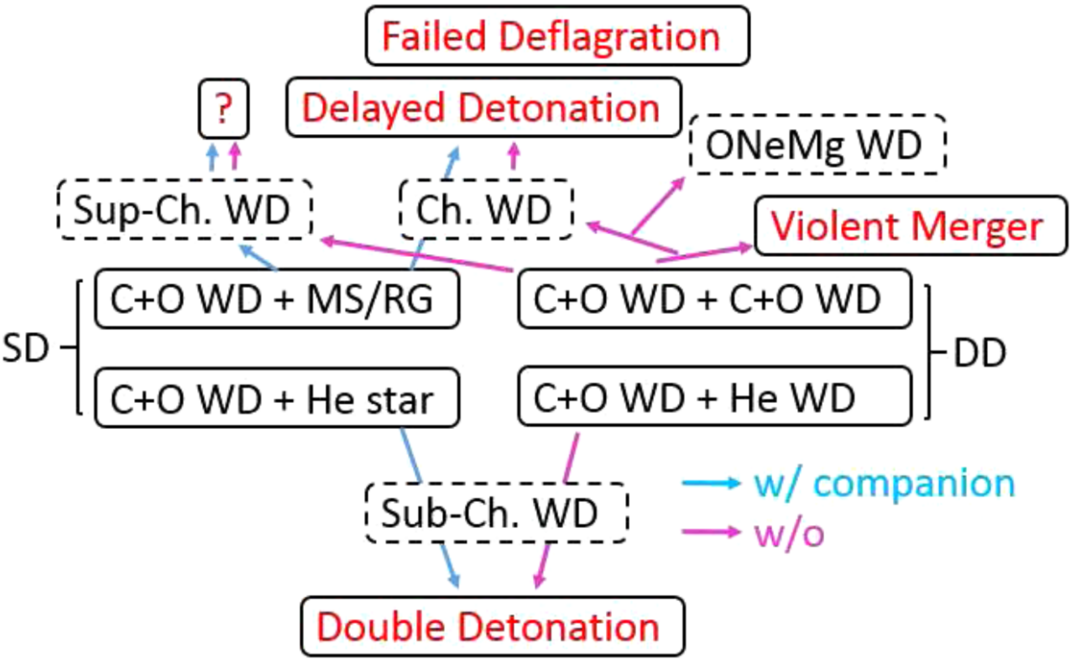

Figure 1.7. The progenitor scenarios (SD and DD) of SNe Ia summarized in a schematic chart adopted from Maeda & Terada (2016)

no significant source was found at the SN position. The detection limit rejected an RG as a companion star. On the other hand, a blue-luminous source was detected in the HST image at the position of SN 2012Z, which favors a helium companion. However, McCully et al. (2022) found the source was still brighter than the expected flux from the radioactive decay (The right bottom panel in Figure 8). They suggested that the observed flux may be originated from the CSM shock-heated companion star or a radioactively heated bound remnant.

1.4.2 Hα emission in the late spectrum

In the SD system, it is predicted that the H or He-rich matter of the companion star is stripped or ablated by the ejecta from analytic works (Wheeler et al. 1975; Chugai 1986) and numerical results (Marietta et al. 2000). When an SN Ia enters the "nebular phase" at which ejecta becomes optically thin after $\sim$ 200 days from the explosion,

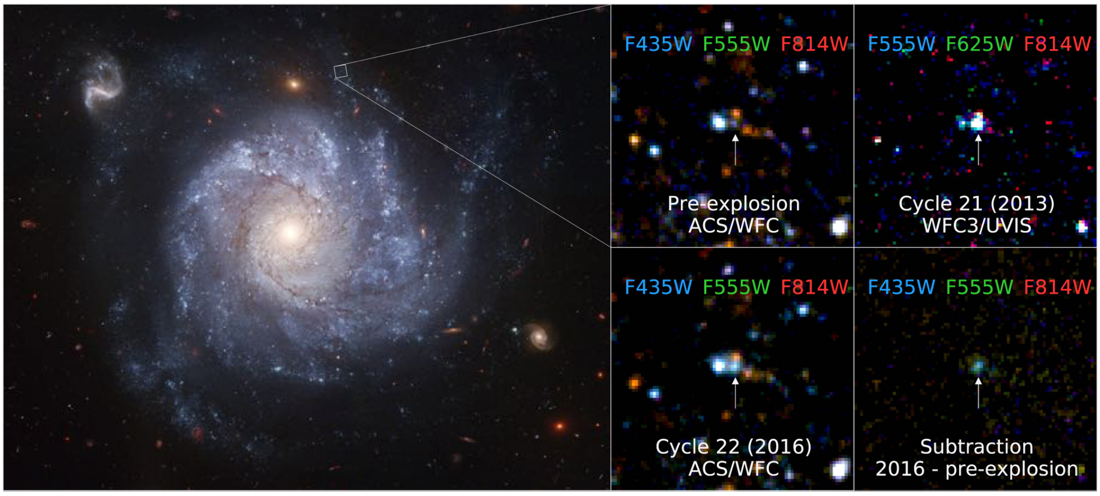

Figure 1.8. Pre/post-explosion HST image of SN 2012Z adopted from McCully et al. (2022).

narrow emission lines (velocity$\sim$ 1000 km/s) can be shown by this stripped matter in the late-time spectra. The recent simulation works provided the quantity of the unbound matter depending on the companion stars: MS, RG, and He-star companions of $\sim 0.1-0.2\,M_\odot$, $0.6\,M_\odot$, and $0.02-0.06\,M_\odot$ (Liu et al. 2012, 2013). Likewise, Boehner et al. (2017) provided a similar amount of the stripped material of RG, MS, and SG stars as approximately $0.33\,M_\odot$, $0.25\,M_\odot$, and $0.17\,M_\odot$. Therefore, finding these emission lines from the H- or He-rich matter can be one of the methods to distinguish the proposed SD or DD scenarios since they are not predicted in the DD system so far. Many observational studies have shown the results supporting the DD system with non-detections of the emission lines from more than 100 SNe Ia (Tucker et al. 2020). There are relatively a few detections of Hα emission: a normal SN 2013ct (Maguire et al. 2016), 3 sub-luminous SNe Ia of ASASSN-18tb (Kollmeier et al. 2019), ATLAS18qtd (Prieto et al. 2020), and SN 2016jae (Elias-Rosa et al. 2021). However, Some explain this non-detection in terms of the observation or the lack of consistent theory. Some studies suggested that the large ratio of the binary separation distance or the low explosion energy can produce weaker Hα (Pakmor et al. 2008; Botyánszki et al. 2018). Tucker et al. (2020) mentioned the possibility of the lack of a consistent theory to explain the suppression of the Hα emission.

1.4.3 Early excess in the light curve

A detonation occurs on the progenitor during a supernova explosion ("shock-breakout"), radiating high energy emissions such as γ-ray or X-ray. This emission lasts in a very short timescale from tens to hundreds of seconds (Piro et al. 2010). Kasen (2010) showed that , after the shock-breakout, the collision of SN ejecta with the companion star produces a shock-heated cooling emission (SHCE) in UV/Optical wavelengths lasting hours and days after the explosion (Companion model). The duration and strength depend on the binary separation distance and the viewing angle. On the other hand, Rabinak & Waxman (2011) derived the analytic form of this luminosity originated from the collision between the ejecta and the envelope of the single star. The SHCE shows a distinct bumpy feature (referred to as "early excess") in the rising part of the light curve powered by radioactive decay of iron group elements which is known to follow t^2 law (or a "simple fireball model"; Nugent et al. 2011). Therefore, we can constrain the progenitor system through estimation of the companion radius by observing the early excess. For example, a peak luminosity of the SCHE from a $1\,R_\odot$ sized star is $R \sim -14\,\mathrm{AB}$ magnitudes whereas that of $R \sim -16\,\mathrm{AB}$ mag for a $10\,R_\odot$ sized star. On the other hand, for the DD system, since a WD companion has a very small radius ($R_{\mathrm{WD}} \sim 0.01\,R_\odot$), the luminosity would be so faint. Nugent et al. (2011) gave a constraint on the radius of the progenitor star (r_{p}) of SN 2011fe as $r_{\mathrm{p}} \sim 0.1\,R_\odot$, ruling out the red giant donor. Furthermore, Bloom et al. (2012) tightened this limit to $r_{\mathrm{p}} \lesssim 0.02\,R_\odot$. Since the shocked ejecta has high temperature, so the color evolution in the companion model is relatively blue ("blue early excess").

However, many recent studies have described the early excess in SNe Ia in different ways. Piro & Morozova (2016) investigated the impact of ^{56}Ni distribution, ^{56}Ni mixing in the WD on the early light curve. When the level of ^{56}Ni mixing is low, there would be a "dark phase" which is a time interval between the actual explosion time and the time when the ^{56}Ni decay powered light curve is shown. If ^{56}Ni distributes relatively shallower regions, the light curve rises steeply. They also found that the distribution of CSM affects the early light curve. Polin et al. (2019) presented that the early excess can be shown in the sub-M_{ch} system with a thin helium shell.

Many observational studies are trying to find consensus evidence for the progenitor system, but many aspects are not found yet. However, this methodology is still powerful in finding the signature of the progenitor system. Motivated by this, we try to understand the progenitor system of SNe Ia through the early-time observation using high-cadence monitoring data obtained from multiple small telescopes.

1.5 Intensive Monitoring Survey of Nearby Galaxies (IMSNG)

Intensive Monitoring Survey of Nearby Galaxies (IMSNG) is an observing program aimed to catch a moment of supernovae to constrain the progenitor system via their size estimation. IMSNG pursues high-cadence ($\lesssim 1\,\mathrm{day}$) monitoring of nearby galaxies with a high supernova rate (SNR) to observe SNe as many as possible (Im et al. 2019).

1.5.1 Sample Selection for Monitoring Targets

To increase the number of young SNe observed, we applied the selection criteria considering the relation between host galaxy properties and the SNR. It is known that both SNe Ia and CCSNe occur frequently in galaxies with a high star formation rate (SFR; Botticella et al. 2012; Gao & Pritchet 2013). Since the near-ultraviolet (NUV) is a good indicator of SFR so the NUV magnitude (M_{NUV}) can be used to trace SNR for both types of SNe.

First, we selected galaxies brighter than $M_{\mathrm{NUV}} < -18.4\,\mathrm{AB}$ mag from the Galaxy Evolution Explorer (GALEX) UV atlas of nearby galaxies (Gil de Paz et al. 2007) and an Updated UV Catalog of GALEX Nearby Galaxies (Bai et al. 2015) which is the extended version of Gil de Paz et al. (2007). This magnitude cut is corresponding to an SFR $\sim 1\,M_{\odot}\,\mathrm{yr}^{-1}$.

Second, we selected nearby galaxies within the distance ($D < 50\,\mathrm{Mpc}$) to detect the SHCE from the progenitor star with the radius down to $\sim 1\,R_{\odot}$ to distinguish the SD or DD system for SNe Ia. Figure 9 shows the early light curve of an SN Ia (SN 2015F) with the SHCE for different sizes of the progenitor star. For a single massive star (CCSNe), Rabinak & Waxman (2011) model is plotted and one for the companion model by Kasen (2010) in an assumption of the optimal viewing angle. "Optimal" assumes the observer looks down on the collision region (Kasen 2010). Note that the SCHE is an-isotropic so it can be ~ 10 times fainter than in the optimal viewing angle (The common viewing angle; Bloom et al. 2012). Considering the distance and the peak luminosity of SCHE from $\sim 1\,R_{\odot}$ sized star, the detection limit is expected to $R \sim 19.5\,\mathrm{AB}$ mag.

Third, we selected objects beyond the galactic latitude (b) of 20 degree not to include galaxies severely reddened by Galactic extinction and obscured by a high density of stars. However, some galaxies (NGC 6946 and ESO 182-G10) at low galactic latitude are included because of their high SNR and M_{NUV} magnitude. In addition, although there are 22 active galactic nuclei (AGN) of 60 IMSNG galaxies, we regarded their NUV luminosity is originated from star formation.

Our selection criteria are summarized below.

1. $M_{\mathrm{NUV}} < -18.4\,\mathrm{AB}$ mag
2. $D < 50\,\mathrm{Mpc}$
3. $b > 20\,\mathrm{deg}$

Finally, IMSNG galaxies are given in Table 1.

Table 1.1. IMSNG Target Galaxies adopted from Im et al. (2019).

Name [AGN type]	RA	Dec	D_L	NUV	Past SNe
	(J2000)	(J2000)	(Mpc)	(AB)	
(1)	(2)	(3)	(4)	(5)	(6)
NGC 289	00:52:42.348	−31:12:20.92	24.0	-18.77	
NGC 337 [LIN]	00:59:50.100	−07:34:41.45	23.0	-18.64	1998dn, 2011dq, 2014cx
NGC 488	01:21:46.836	+05:15:24.48	38.0	-18.88	1976G, 2010eb
NGC 895	02:21:36.468	−05:31:17.00	37.0	-19.02	2003id
NGC 1097 [LIN]	02:46:19.092	−30:16:29.89	14.0	-18.55	1992bd, 1999eu, 2003B
NGC 1309	03:22:06.600	−15:24:00.07	29.0	-19.04	2002fk, 2012Z
NGC 1365 [S1.5]	03:33:36.396	−36:08:25.84	18.0	-19.33	1957C, 1983V, 2001du, 2012fr
UGC 2855	03:48:20.736	+70:07:58.30	14.0	-18.75	2014dg
NGC 1672 [S2]	04:45:42.516	−59:14:50.42	19.0	-19.34	2017gax
NGC 2207/IC 2163^a	06:16:22.044	−21:22:21.76	38.0	-20.32	1975A, 1999ec, 2003H, 2010jp, 2013ai, 2018lab
NGC 2336 [S2]	07:27:04.068	+80:10:41.02	29.0	-18.83	1987L
NGC 2442 [LIN]	07:36:23.796	−69:31:50.70	21.0	-19.20	1999ga, 2015F
NGC 2775	09:10:20.100	+07:02:17.23	43.0	-18.69	1993Z
NGC 2776	09:12:14.508	+44:57:17.53	41.0	-19.34	
NGC 2782 [oLLAGN]	09:14:05.064	+40:06:49.57	41.0	-18.76	1994ak
NGC 2993/2992 [S2]^a	09:45:48.312	−14:22:06.17	34.0	-18.85	2003ao, AT2017ejx
IC 2537	10:03:51.876	−27:34:14.81	36.0	-18.40	2010lm
NGC 3147 [S2]	10:16:53.688	+73:24:02.63	40.0	-19.29	1972H, 1997bq, 2006gi, 2008fv
NGC 3169 [LIN]	10:14:14.892	+03:27:58.86	45.0	-19.25	1984E, 2003cg
NGC 3183	10:21:48.960	+74:10:37.16	49.0	-18.56	

Table 1.1. (cont'd)

Name [AGN type] (1)	RA (J2000) (2)	Dec (J2000) (3)	D_L (Mpc) (4)	NUV (AB) (5)	Past SNe (6)
NGC 3244	10:25:28.848	−39:49:39.00	38.0	-18.63	2010ev
NGC 3294	10:36:16.236	+37:19:28.63	30.0	-18.43	1990H, 1992G
NGC 3344	10:43:31.116	+24:55:19.74	20.0	-19.42	2012fh
NGC 3367 [S2]	10:46:35.004	+13:45:02.09	45.0	-19.84	1986A, 1992C, 2003aa, 2007am, 2018kp
NGC 3359	10:46:36.840	+63:13:26.83	23.0	-19.07	1985H
NGC 3445	10:54:35.712	+56:59:23.32	33.0	-18.55	
NGC 3629	11:20:31.776	+26:57:47.84	38.0	-18.55	
NGC 3646	11:21:43.092	+20:10:11.10	44.0	-19.47	1989N, 1999cd
NGC 3938	11:52:49.368	+44:07:14.88	19.0	-18.87	1961L, 1964I, 2005ay, 2017ein
NGC 4030	12:00:23.580	−01:06:00.00	27.0	-19.11	2007aa
NGC 4038 (Arp 244)	12:01:53.004	−18:52:04.76	21.0	-19.40	1921A, 1974E, 2004gt, 2007sr , 2013dk
NGC 4039 (Arp 244)	12:01:53.616	−18:53:11.11	21.0	-19.39	
NGC 4108	12:06:44.316	+67:09:46.12	41.0	-18.50	ASASSN-15lf
NGC 4254 (M 99) [LIN]	12:18:49.572	+14:24:59.08	16.0	-19.03	1967H, 1972Q, 1986I, 2014L
NGC 4303 (M 61) [S2]	12:21:54.936	+04:28:27.05	18.0	-19.54	1926A, 1961I, 1964F, 1999gn, 2006ov, 2008in, 2014dt
NGC 4314 [LIN]	12:22:31.980	+29:53:43.48	44.0	-18.46	1954A
NGC 4321 (M 100) [LIN]	12:22:54.768	+15:49:18.80	14.0	-18.65	2006X
NGC 4500	12:31:22.152	+57:57:52.81	48.0	-18.47	
NGC 4653	12:43:50.916	−00:33:40.54	39.0	-18.66	1999gk, 2009ik
NGC 4814	12:55:21.936	+58:20:38.80	40.0	-18.53	

Table 1.1. (cont'd)

Name [AGN type] (1)	RA (J2000) (2)	Dec (J2000) (3)	D_L (Mpc) (4)	NUV (AB) (5)	Past SNe (6)
NGC5194 [S2]/5195[a] (M51)	13:29:52.692	+47:11:42.54	8.4	-19.03	1945A[b], 1994I, 2005cs, 2011dh
NGC 5236 (M83)	13:37:00.876	−29:51:56.02	4.9	-18.82	1923A, 1945B, 1950B, 1957D, 1968L, 1983N
NGC 5371 [LIN]	13:55:39.936	+40:27:41.90	33.0	-19.09	1994Y
NGC 5430	14:00:45.720	+59:19:42.24	47.0	-18.70	PTF10acbu (PSN)
NGC 5457 (M101)	14:03:12.600	+54:20:56.62	6.9	-19.36	1909A, 1951H, 1970G, 2011fe
NGC 5584	14:22:23.772	−00:23:15.32	25.0	-18.43	1996aq, 2007af
NGC 5668	14:33:24.300	+04:27:01.19	25.0	-18.72	1952G, 1954B, 2004G
NGC 5850 [LIN]	15:07:07.644	+01:32:40.74	38.0	-18.65	1987B
NGC 5962	15:36:31.680	+16:36:28.15	30.0	-18.68	2016afa, 2017ivu
NGC 6070	16:09:58.680	+00:42:34.31	27.0	-18.58	
NGC 6555	18:07:49.188	+17:36:17.53	35.0	-18.54	
ESO 182-G10[c]	18:18:30.600	−54:41:39.41	49.0	-19.00	2006ci
NGC 6744 [LIN]	19:09:45.900	−63:51:27.72	9.3	-19.05	2005at
NGC 6814 [S1.5]	19:42:40.608	−10:19:25.32	23.0	-18.61	
NGC 6946[c,d]	20:34:52.572	+60:09:13.57	6.1	-19.12	1980K, 2002hh, 2004et, 2008S, 2017eaw
NGC 6951 [S2]	20:37:14.088	+66:06:20.45	25.0	-18.66	1999el, 2000E, 2015G
NGC 7083	21:35:44.592	−63:54:09.79	34.0	-18.98	1983Y, 2009hm
NGC 7479 [S2]	23:04:56.676	+12:19:22.12	30.0	-18.96	1990U, 2009jf
NGC 7552	23:16:10.776	−42:35:03.41	29.0	-18.84	2017bzc
NGC 7714/7715[a]	23:36:14.112	+02:09:18.07	41.0	-19.18	1999dn, 2007fo

(1) Galaxy name. The name in the parenthesis is another notable name of the galaxy, and the AGN types in the large parentheses are S (Seyfert), LIN (LINER), and oLLAGN; (2) & (3): Equatorial coordinates in J2000; (4) the luminosity distance; (5) NUV absolute magnitude in AB mag; (6) the past SNe in the galaxy.

[a] Galaxies in pair, the primary, NUV-selected galaxy number is given first; [b] In NGC 5195; [c] Low Galactic latitude target; [d] This object had five additional SNe before 1980: 1917A, 1939C, 1948B, 1968D, and 1969P.

1.5.2 Facilities : Small Telescope Network (Somangnet)

In the modern era, large aperture telescopes (> 8-m) have revealed unsolved natures of astrophysical objects. However, small optical telescopes still play an essential role in studying time-variant events, or "transients". To maximize the usage of small telescopes with apertures of $\sim 0.4 - 1.0$-m in Korea for transient science, Small telescope network (SomangNet[‡]) is established (Im et al. 2021). SomangNet currently utilizes more than 10 telescopes operated by Korean institutions. Some telescopes are special in that (i) they have a wide field of view (> 1 deg), (ii) they are located in the USA, Chile, and Australia allowing us to use the Southern sky and many time zones, and (iii) they are possible to perform medium band observation and low-dispersion spectroscopy ($R \sim 1000$). Figure 10 shows the distribution of SomangNet facilities. IMSNG uses these telescopes. Besides, Some telescopes are also included for IMSNG observation: Mt. Sobaek Optical Astronomy Observatory (SOAO) 0.6-m telescope in Korea, Maidanak Astronomical Observatory (MAO) 1.5-m telescope in Uzbekistan, and the United Kingdom InfraRed Telescope (UKIRT) 3.6-m in Hawaii.

1.5.3 Observation & Data reduction

Since each telescope has different characteristics, the exposure time is also set differently for each facility to the detection limit of $R \sim 19.5$ AB mag for the point source. The filterset also varies among telescopes but mainly broad-band (Bessell $BVRI$ and SDSS $g'r'i'z'$) and medium-band filters are equipped. Typical monitoring is performed using B, R, g, and r-band filters due to their high sensitivity. Other filters can be also used when the follow-up begins. Data are transferred to our server after finishing our daily observing run. Our python-based data processing pipeline so-called "gppy" automatically detects new raw data and starts the data processing (Paek et al. in prep.). The processing consists of standard reduction (bias, dark subtraction, and flat fielding). Subsequent processes are conducted such as cosmic-ray removal, astrometry, registration, photometric calibration, and image subtraction. Reference images previ-

---

[‡] It is a Korean abbreviation for a small telescope network.

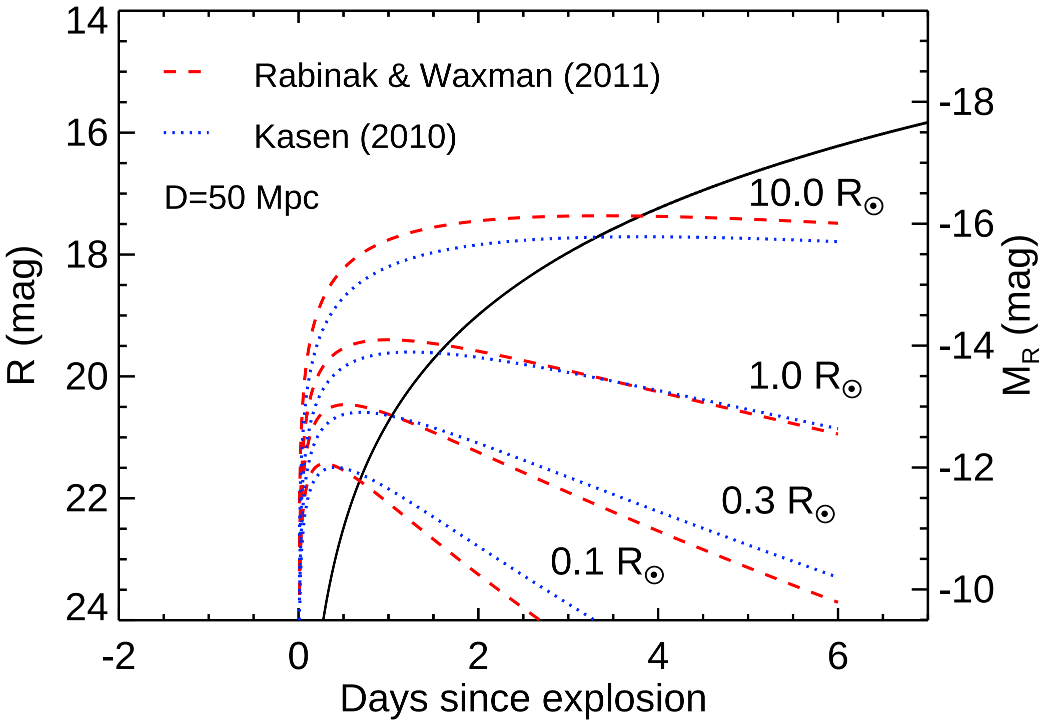

Figure 1.9. An early light curve of a typical SN Ia (Solid black line) with the predicted SHCE in the dotted lines for Kasen (2010) and the dashed lines for Rabinak & Waxman (2011). The black solid line is the best-fit early light curve of SN 2015F (Im et al. 2015) shifted to $D = 50\,\mathrm{Mpc}$ at the optimal viewing angle. This figure is adopted by Im et al. (2019).

ously produced using images in the good weather condition are subtracted from science images to detect new transients. After the calibration, the gppy algorithm explores new transients in the subtracted images, uploading them to our database "IMSNG Transient Viewer". Our database updates their information such as light curves, image thumbnails, daily observing status, etc.

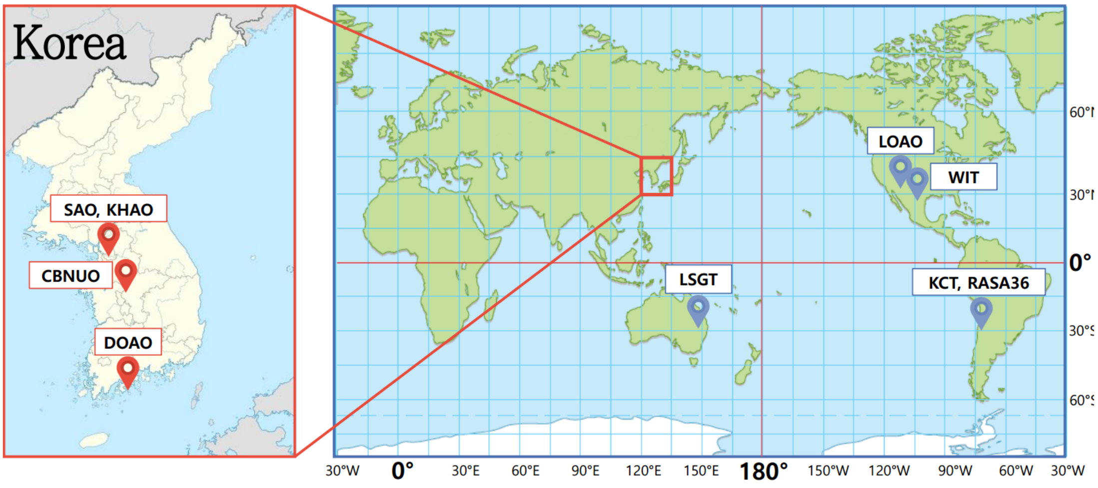

Figure 1.10. The distribution of the SomangNet facilities adopted from Im et al. (2021).

1.5.4 Current Observing Status

IMSNG has performed its run since 2014, observing many various transients so far. There are 46 supernovae occurred in the IMSNG galaxies from 2014 to autumn 2021 (Poster presented in the KAS fall meeting 2021, Kim et al. 2021), which SNR is $5.75\,\mathrm{SNe\,yr^{-1}}$ or $0.096\,\mathrm{SNe\,yr^{-1}}$ per galaxy. This number is ~ 1.8 times larger than $0.05\,\mathrm{SNe\,yr^{-1}}$ predicted in Im et al. (2019). In 2015, a possible SHCE of SN 2015F was detected (Im et al. 2015) and intensively monitored by our robotic telescope, Lee Sang Gak Telescope (LSGT; Im et al. 2015; Choi & Im 2017). After that, the early light curves of SNe Ia (SN 2018kp), Ic (SN 2017ein and SN 2017gax) allowed us to constrain the radius of the progenitor system (Choi in prep.). Furthermore, there are many other transients including fast-evolving blue optical transients (FBOTs), luminous blue variables (LBVs), luminous red novae (LRNe), variable stars (Choi et al. 2018), AGN (Kim et al. 2019), and the optical afterglows of Gamma-ray burst (GRB). In particular, IMSNG played an important role in the field of multi-messenger astronomy (MMA) in the follow-up observation: AT 2017gfo, the electromagnetic (EM) counterpart of a gravitational source GW170817 (Abbott et al. 2017; Troja et al. 2017; Im et al. 2017) and TXS 0506+056, an optical counterpart of the neutrino source IceCube-170922A (Hwang et al. 2021). With further improvements such as the participation of new telescopes, automated observation, and transient classification using artificial intelligence (AI), IMSNG will discover new transients and contribute to the understanding of the nature of transients.

1.6 Outline of the Thesis

This thesis aims to look for observational evidence for the progenitor system finding the signatures of the companion star focused on the early-time observation. Many observations using the MAO 1.5-m, the SAO 1-m, the McDonald 0.8-m, 2.1-m telescopes, and WIT have performed. To improve an observing cadence also in the southern sky, we installed KIAS Chamnun Telescope (KCT) at DeepSkyChile located in Chile in March 2020, and I have established automated operations for several years. In Chapter 2, we introduce characteristics of the KCT system and describe how the operation was established. Among many early detections of SNe, we studied two SNe Ia 2019ein and 2021hpr.

In Chapter 3, we present the early-time observation of SN 2019ein based on optical and near-infrared (NIR) data. Basic characteristics are investigated through the long-term light curve and a series of low-dispersion long-slit spectroscopy. The radius of the companion star is constrained from the early light curve together with the color curve using the companion model. With this result, we discuss the possible progenitor system of SN 2019ein.

In Chapter 4, we successfully detected the significant feature of a blue early excess of SN 2021hpr in IMSNG optical data. Likewise, using the companion model, we constrained the radius of the companion star. Furthermore, we subsequently analysed the late spectroscopic data observed in the nebular phase to find the Hα emission resulting from the stripped companion matter. We discuss the discrepancy between the early light curve analysis and the late spectroscopy, leaving other progenitor scenarios.

Finally, we summarize the results of chapters above and provide conclusions with future prospects in Chapter 5

Table 1.2. SomangNet Telescopes adopted from Im et al. (2021). The contents of KCT are modified for the currently used CCD.

Telescope Name	Aperture/ F-ratio	Instruments	Imager Field of View	5-σ Depth[a] Med. Seeing	Location	Longitude/ Latitude	Altitude (m)
SAO 1 m[b]	1.0 m f/6	4k x 4k CCD $R \sim 600$ Spec.	$21'.2 \times 21'.2$	$R = 19.7$ $2''$	Seoul, Korea	126:57:15.7E 37:27:25.7N	175
KHAO 0.8 m	0.8 m f/7.0	4k × 4k CCD	$23'.7 \times 23'.7$	$R = TBD$ TBD	Yongin, Korea	127:04:54.6E 37:14:19.2N	141
KHAO 0.4 m	0.4 m f/6.7	3.3k x 2.5k CCD	$21' \times 16'$	$R = 18.4$ $2''$	Yongin, Korea	127:04:56.1E 37:14:20.7N	119
DOAO 1 m[b]	1.0 m f/8.0	2k x 2k CCD Echelle Spec.	$13'.2 \times 13'.2$	$R = 20.6$ $2''.4$	Goheung, Korea	127:26:48.6E 34:31:34.5N	81
CBNUO 0.6 m	0.6 m f/2.92	4k × 4k CCD	$1^{\circ}.19 \times 1^{\circ}.19$	$R = 18.6$ $2''.5$	Jincheon, Korea	127:28:31.2E 36:46:53.5N	87
LSGT[c]	0.43 m f/6.8	SNUCAM-II 1k x 1k CCD	$15'.7 \times 15'.7$	$r = 20.1$ $3''.0$	Siding Spring Obs., Australia	149:04:11.2E 31:16:24.1S	1122
LOAO 1 m	1.0 m f/8.0	4k x 4k CCD	$28'.1 \times 28'.1$	$R = 20.7$ $3''.1$	Mt. Lemmon, Arizona, US	110:47:19.2W 32:26:32.2N	2776
WIT[c]	0.25 m f/3.6	4k x 4k CCD	$2^{\circ}.34 \times 2^{\circ}.34$	$V = 19.3$ $6''.0$	McDonald Obs., Texas, US	104:01:22.1W 30:40:17.5N	2057
KCT[d]	0.36 m f/7.2	4k × 4k CCD	$49'.4 \times 49'.4$	$r = 18.5$ $3''.0$	Río Hurtado Valley, Chile	70:51:11.8W 30:31:34.7S	1710
SNU RASA36[e]	0.36 m f/2.2	4k × 4k CMOS	$2^{\circ}.67 \times 2^{\circ}.67$	$r = 19.2$ $6''.5$	Río Hurtado, Coquimbo, Chile	70:45:47.2W 30:28:20.8S	1525

Observatories are ordered toward E in longitude from the Prime Meridian. The accuracy of the longitudes, latitudes, and the altitudes are a few tenths of seconds, and a few meters, respectively. More accurate coordinates of some of the telescopes will be presented elsewhere (Sung et al. 2021, in preparation).

[a] 5-σ depths are given for an exposure time of 10 min under median seeing.

[b] Telescopes with spectroscopic capabilities (see text for details).

[c] Telescopes with low resolution imaging spectroscopic capabilities.

[d] Managed and maintained by DeepSkyChile.

[e] Managed and maintained by ObsTech.

Chapter 2

KIAS CHAMNUN TELESCOPE (KCT)

2.1 Introduction

Time-domain astronomy studies astrophysical phenomena that have time-dependence on their brightness with a time scale from the moments to order of years (or "transients"), which is considerably associated with their various physical origins and mechanisms.

Small telescopes (aperture size $<$ 1-meter) have some advantages for observing these transients despite the modern era of the very large telescopes. Small telescopes are relatively low-priced and easily installed. In addition, they slew fast and have a wide field of view (fov) due to their short focal ratios. These characteristics allow transients to be monitored with adequate observing cadences to know their unknown physics. Automated observation (or robotic observation) that makes observing runs every day from initiation, and image acquisition to shutdown without human intervention can achieve time series observation.

Small telescope network (SomangNet; Im et al. 2021) is a facility that uses multiple 0.4-1.0 meter class telescopes in Korea and some of the systems abroad (more than 10 telescopes). SomangNet has contributed to maximizing the usage of telescopes in Korea for time-series follow-up observations. Seoul National University (SNU) has already operated a robotic telescope of 0.43 meter Lee Sang Gak Telescope (LSGT; Im et al. 2015; Choi & Im 2017) to observe many time-variant objects in the dark skies in Australia, uncovering their astrophysical origins such as supernovae (SNe), active galactic nuclei (AGN), kilonova (KN), and asteroids (Im et al. 2015; Kim et al. 2019; Abbott et al. 2017; Kwon et al. 2019). However, LSGT was the only telescope in the southern hemisphere. To increase the chance to catch the transient events with higher cadence, we decided to install KIAS* Chamnun Telescope (KCT) in Chile. The name "Chamnun" is a Korean word meaning of eyes that see the truth. KCT is originally a research asset of KIAS and it is agreed to be operated by SNU to use in time-domain studies.

KCT is a 0.36-m observing system installed in a roof dome with other telescopes managed by DeepSkyChile† SpA located at Río Hurtado Valley, Chile (1710 meters above sea level). The roof dome is controlled automatically by the weather monitoring system. Here, we present the overall characteristics and performance of KCT based on the observational data.

2.2 Characteristics of the KCT System

2.2.1 Hardware & Software

KCT uses a Corrected Dall-Kirkham (CDK) optical tube manufactured by PlaneWave Instruments‡. The primary mirror is an ellipsoidal mirror with a 0.36-meter (14-inch) diameter, and other components consist of a spherical secondary mirror and lens group. All components of this optics are designated to obtain astronomical images with coma-free, no off-axis astigmatism. Its effective focal ratio is f/7.2 or 2536 mm. To achieve rapid observing performance, we do not use an auto-guiding system. The telescope is installed on the German equatorial Paramount MX+ mount manufactured by Software

---

[*] Korea Institute for Advanced Study

[†] https://www.deepskychile.com/en/

[‡] https://planewave.com/

Figure 2.1. KCT right after installation at DeepSkyChile (taken by Franck Jobard).

Bisque on the fixed pier (Figure 1).

We use STX16803 CCD camera of Santa Barbara Instrument Group (SBIG), which

Table 1. Specifications of KCT camera (STX16803).

Properties	Values
Sensor chip	KAF-16803 (36.8 mm × 36.8 mm)
Gain[a]	1.27 e$^-$/ADU
Full well[a]	100000 e$^-$
QE peak	60%
Dark current[b]	0.04 e$^-$/pix/sec at $-10\,^\circ$C
Readout noise[a]	9 e$^-$ (4 MHz)
Readout time[a]	9 sec
Pixel size	9 μm × 9 μm
Pixel number	4096 × 4096
Pixel scale	$0\overset{''}{.}724$ per pixel
Field of view	$49\overset{'}{.}4 \times 49\overset{'}{.}4$

[a] The manufacturer's data are adopted.

[b] Dark frame taken with 300 sec exposure is used.

is now acquired by Diffraction Limited. It uses a KAF-16803 sensor chip with the size of 36.8 mm × 36.8 mm. Its quantum efficiency (QE) is peaked at $\sim 60\%$. Pixel scale is calculated as $0\overset{''}{.}724$ per pixel and the field of view (fov) is $49\overset{'}{.}4 \times 49\overset{'}{.}4$. In front of the camera, the SBIG FW7-STX filter wheel with the SDSS Gen2 filter set of $u'g'r'i'$ is attached. Table 1 summarizes the specifications of STX16803.

We calculated the total throughput of the KCT imaging system (Colored solid lines) by multiplying the filter transmission curves (Colored dashed lines) and the QE curve (Black solid line) of the CCD (Figure 2). We also considered the sky model using the

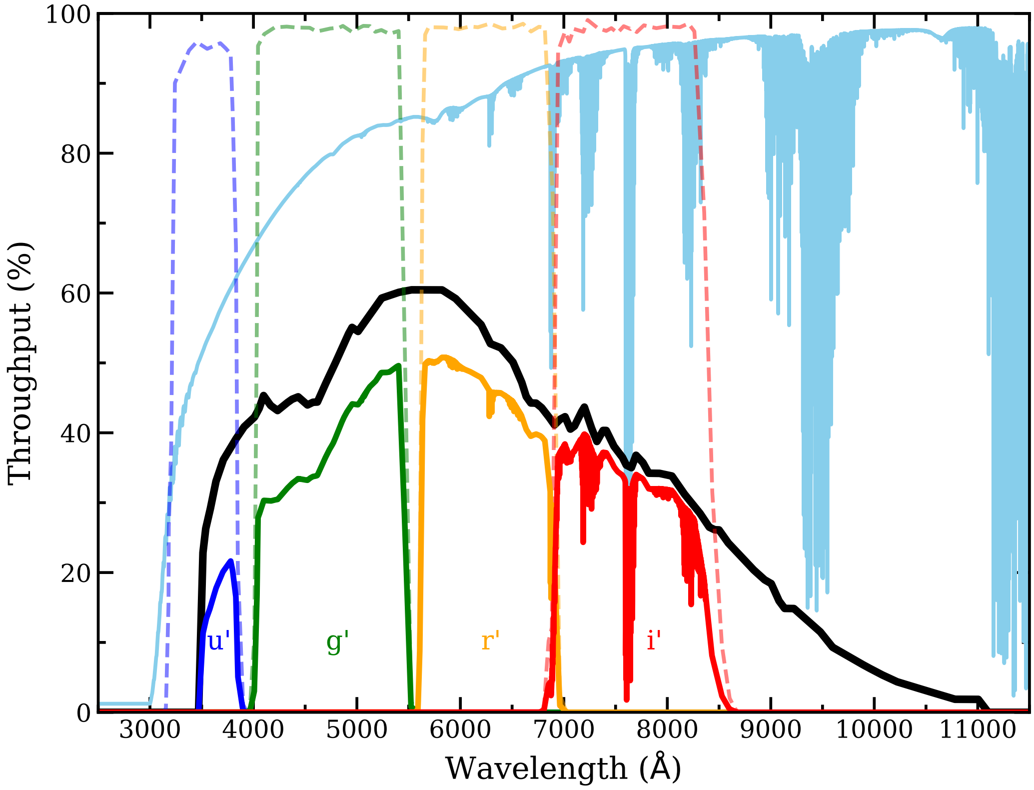

Figure 2.2. The transmission curve of the SDSS *ugir* filters (colored dashed lines). The total throughput of KCT is shown as colored solid lines after considering the QE of STX16803 CCD (Black solid line) and the transmission curve of the sky model (sky blue line).

web-based `skycalc`[§] with an assumption of the observation under the sky with airmass 1.3, dark night with the scattered starlight, and the location of La Sila 2400m above sea level where is the nearest of the other location.

2.2.2 Automated Operation

Observations have been performed with script-based "observing plans" using ACP Observatory Control Panel[¶] (referred to as ACP). In the plans, observing configurations

---

[§] https://www.eso.org/sci/software/pipelines/skytools/skycalc

[¶] https://acpx.dc3.com/

such as filter, binning, exposure time, number of frames, etc., for specific targets can be written. All the software (Maxim DL version 6.26 for the camera, The Sky X for the mount, Planewave Interface 3 for the focuser.) are connected with ACP. Here we use the ACP scheduler dispatcher[‖] which decides “the best choice” for the uploaded observing plans in advance considering the altitude of the target, weather condition, and other constraints (Denny 2004). Since we are now focusing on the monitoring observation of nearby galaxies to detect transients, the ACP scheduler allows us to make the observation reducing many parts of operator intervention.

Figure 3 shows a scheme of the KCT automated operation. When the dome is open, the ACP scheduler recognizes the weather is under the good condition to begin the observing run. ACP starts up software, unparks the scope, cools the camera, and performs initial auto-focusing (referred to as “startup”). Auto-focus takes less than 5 minutes. Next, if a pending target satisfies constraints in the observing plan script, the scope slews to the target, and start exposure. If no targets to observe, ACP waits until there is a target satisfying the constraints (“sleep”). When the dome is closed by the poor weather or the sun rises, a shutdown procedure which is the same as a startup but in the opposite way begins. Acquired data is transferred to the server after the shutdown every day. For calibration images such as bias, dark frames, they are obtained when the dome is closed. Skyflats are also taken before the dome closed in the morning since there is no domeflat so far.

2.3 Performance

We have performed the observation of nearby galaxies since the installation in March 2020. So the performance of KCT is tested with these data. Here, we present the performance of the telescope so far based on these data.

[‖] http://scheduler.dc3.com/

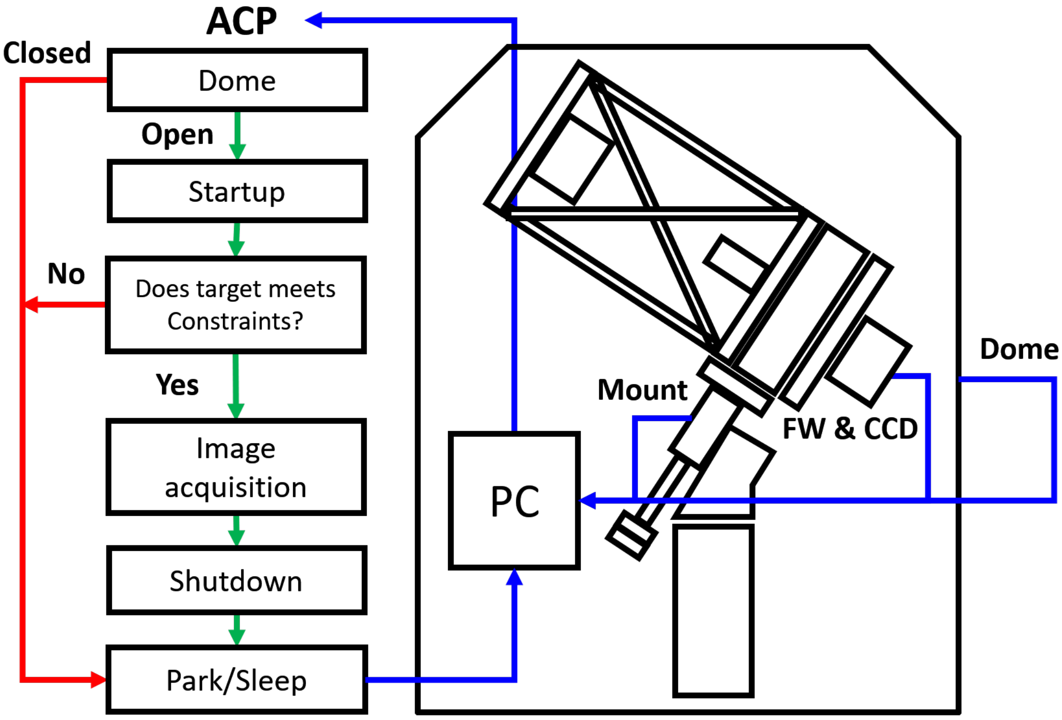

Figure 2.3. A schematic overview of the KCT automated observation using ACP.

2.3.1 Limiting magnitudes

We used images of NGC 6744 to measure the limiting magnitudes of g, r, i-bands observed on August 3 2021 with 120 sec exposure at $3\overset{''}{.}0$ seeing, and the moon phase was 26% (Figure 4). We added a u-band image of NGC 6902 taken on August 9 2021 with the same exposure but the seeing was at $3\overset{''}{.}7$ (1% moon phase). These images were combined into 600 sec after image reduction of bias and dark subtraction, and flat-fielding. Image quality is good with no fringe and vignetting pattern in overall regions. To calculate zero-points, we performed photometric calibration using stars having data release 9 (DR9) of the AAVSO photometric all-sky survey (APASS; Henden et al. 2016). For the u-band image, we used the second data release (DR2) of the SkyMapper Southern Survey (Onken et al. 2019). We used the stars for the calibration only located in a region within $0\overset{'}{.}5$ radius from the center of the chip to avoid the effect on the corner. The 5σ limiting magnitudes for point sources using the 2×FWHM (Full-Width

Figure 2.4. A color composite test image of NGC 6744 (gri) taken by STX16803 CCD. The field of view is $49\rlap{.}'4 \times 49\rlap{.}'4$. A feature on the top middle of the image is a bad pixel column.

Half Maximum) diameter sized aperture are calculated as 15.6, 18.9, 18.5, and 17.8 AB magnitudes in u, g, r, and i-bands.

2.3.2 Shutter pattern

STX16803 uses a mechanical shutter so we obtained a series of test images to investigate from which exposure time the shutter pattern begins to be seen. After the shutdown, the telescope was slewed to the southwestern sky during the dawn giving $0.1 - 6.0$ sec exposure (0.1 sec is the minimum exposure supported by CCD). Figure 5 shows a series of these light frames. We divided 6.0 sec image with 0.1 sec image to see any significant feature produced by the movement of the shutter. However, we cannot find the pattern, indicating that images taken with an exposure time longer than 0.1 sec are not influenced by the shutter pattern.

2.3.3 Point Spread Functions (PSFs) & Seeing

We investigated whether the shape of point spread functions (PSFs) is uniform in different regions of the field of view or not. Figure 6 shows the single exposure (120 sec) r-band image divided by 16×16 sections and PSF in each image section. PSF in each section is produced using stars with S/N higher than 5 with PSF Extractor (`PSFEx`; Bertin 2011).

We found PSFs are uniform overall with slight elongation of an axis ratio (b/a) of ~ 0.95. To check if this elongation is from the long-exposure time, so we separately obtained the test images of very short exposures (1 sec). However, these elongated PSFs can be also seen in these images so this issue mainly seems to result from the optic system. In addition, we obtain the seeing FWHM distribution using the observational data taken from 2021 September to 2021 December 10 (Figure 7). The median value is $3\overset{\prime\prime}{.}36$ which appears to be large considering the astro-climate in Chile. It is possibly associated with the elongated issue.

2.4 Scientific programs

Automated observation of the KCT system involves many scientific topics, mainly focusing on time-series observations. The Intensive Monitoring Survey of Nearby Galax-

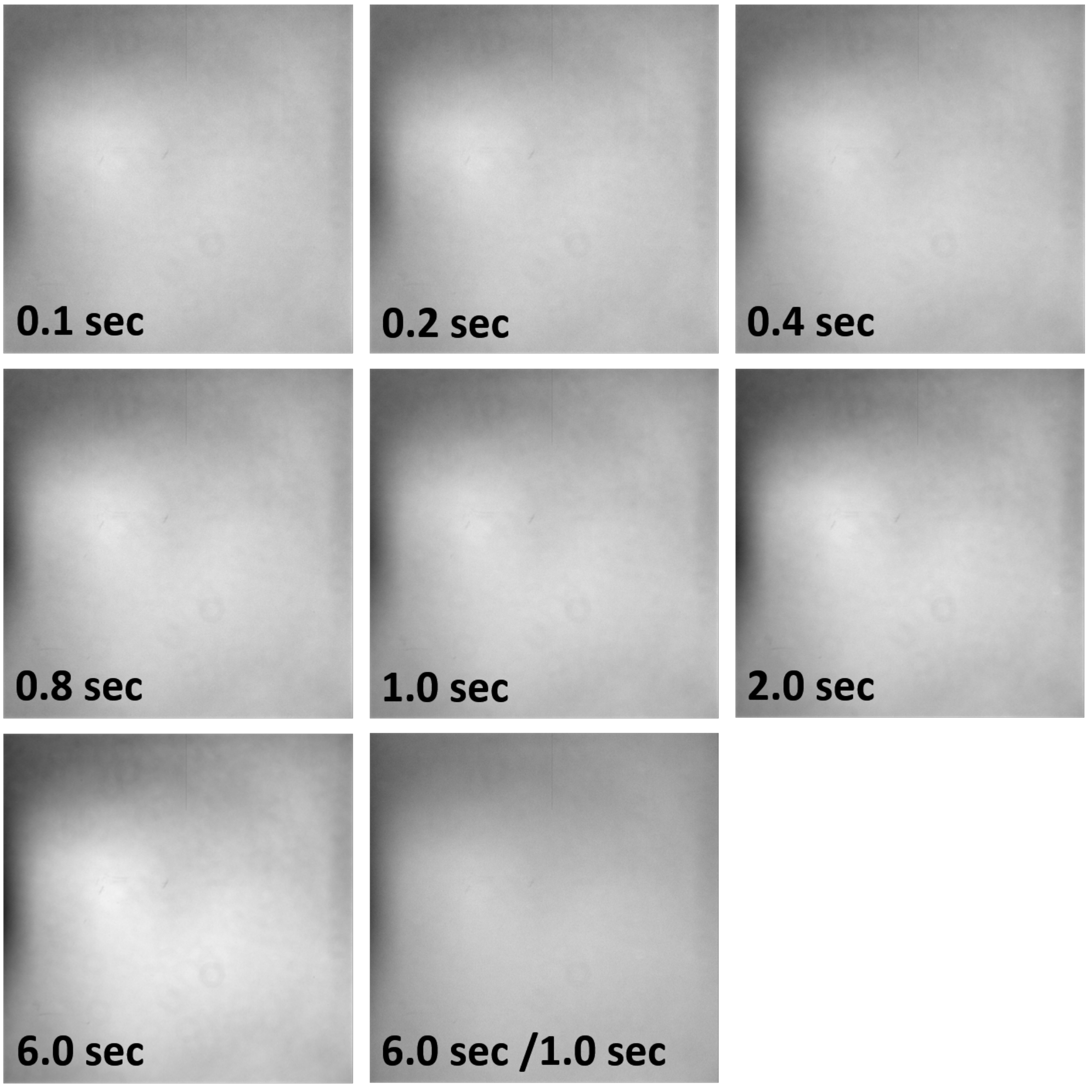

Figure 2.5. Light frame images from 0.1 − 6.0 sec for the shutter pattern inspection including 6.0 sec image divided by 0.1 sec image. No significant pattern is seen in this image, suggesting the shutter pattern is negligible even in 0.1 sec exposure which is the minimum exposure available on STX16803.

ies (IMSNG) is our main scientific program to observe nearby galaxies with a high cadence within $\sim$ 0.5 day. Using telescopes located at other observing sites (Im et al. 2019), we expect to catch young supernovae (SNe) that occurred within a few days since the explosion to constrain their unknown aspects of the progenitor system. Sample

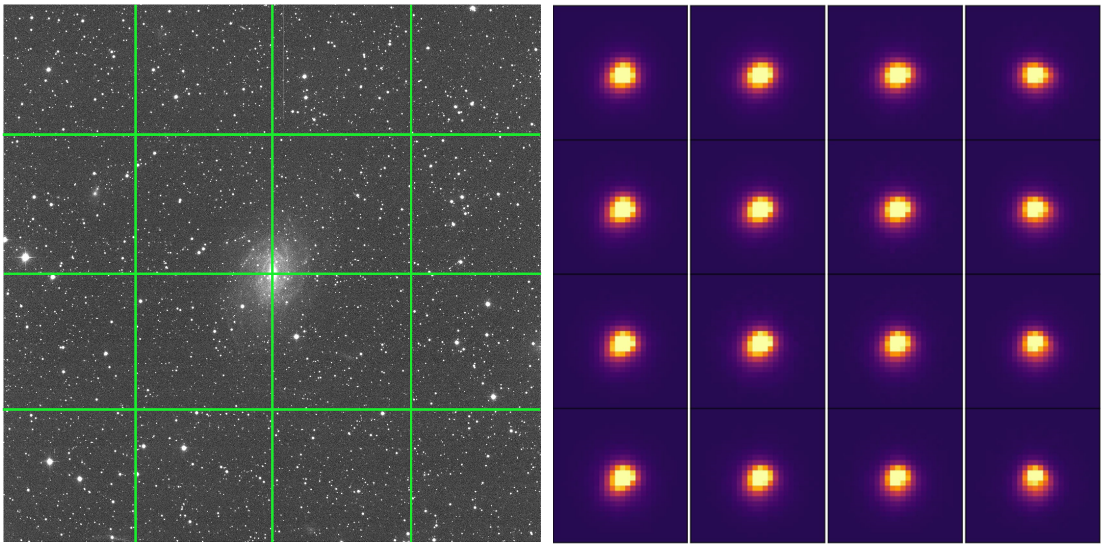

Figure 2.6. (Left) The same image in Figure 4 but a single image in r-band divided into 16 sections. (Right) The PSF model in each image section.

galaxies have high star-forming rates (SFR) with bright NUV magnitudes (< -18.4 AB) to increase the possibility to observe SNe. The galaxies at distances less than 50 Mpc are selected to reach $R \sim -14$ AB magnitudes if possible. This criterion is corresponding to the brightness of thermal emission from the collision between SN ejecta and $1\,M_{\odot}$ main sequence companion (Kasen 2010). For example, we detected the early phase of a Type Ia supernova, SN 2021aefx, on 2021 November 12 (UT) after the first report in Transient Name Server** (TNS). The left panel in Figure 8 shows NGC 1566 before and after the detection of SN 2021aefx (Choi in prep.). We can also study other transient events. KCT participates in the monitoring of the SMBHB candidate SDSS J1430+2303 showing its rapidly decreasing period (Jiang et al. 2022) (Right panel in Figure 8). These monitoring data indicate the KCT system has the potential to contribute to revealing the origin of transients although there are still improvements required.

**https://www.wis-tns.org/

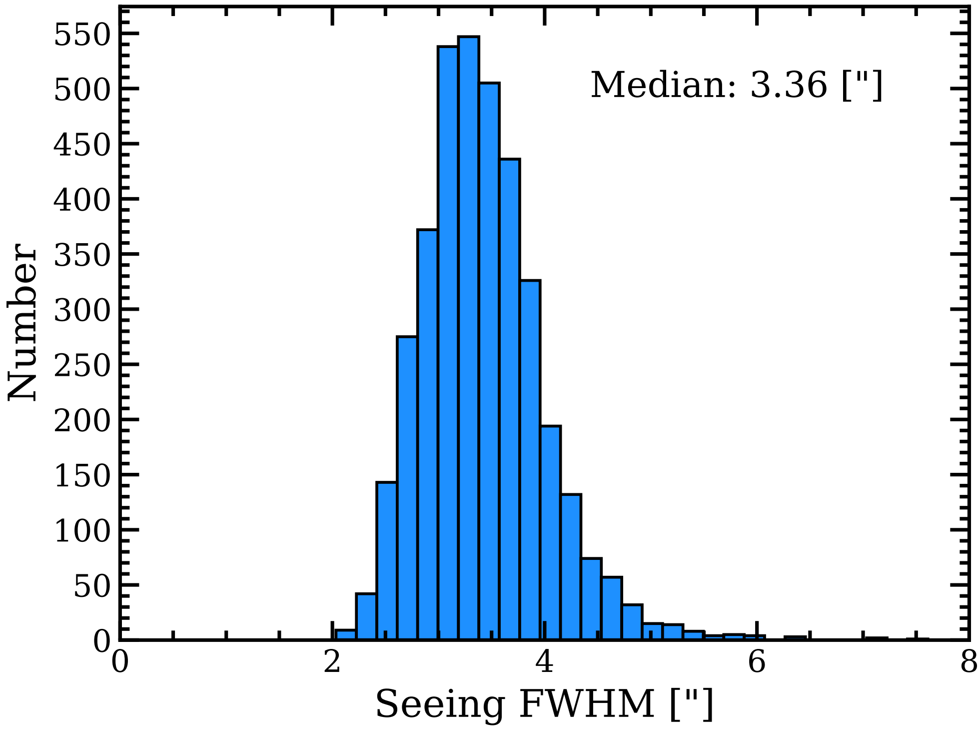

Figure 2.7. A histogram of the seeing FWHM of 1 sec exposure r-band images observed from 2021 September to 2021 December 10.

2.5 Future plans

KCT system will be upgraded in its operation and performance. To increase the efficiency of monitoring, we plan to reduce overhead and waiting time between the monitoring targets by add more targets or duplicated observation. Furthermore, customizing observing plans will be done by replacing on-going plans with other Time of Opportunity (ToO) observation to cope with the rapid follow-up of emergent transients.

In preparation for the LIGO-Virgo O4 observing run, which will resume operation in the fall of 2022, KCT is expected to produce high-quality observational data with the advantages of a wide field of view and a excellent night sky in Chile, along with other small telescopes.

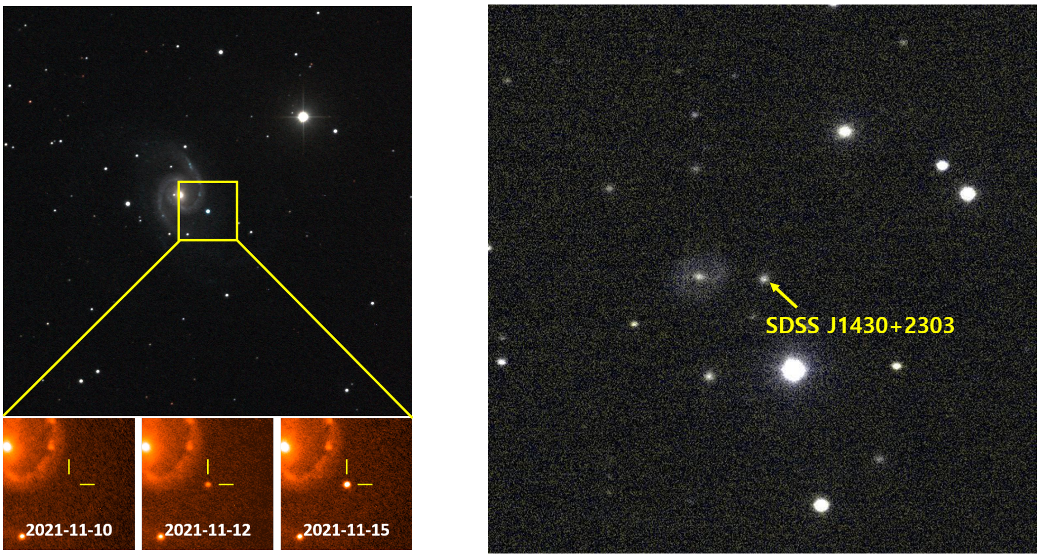

Figure 2.8. (Left) A gri-band color image of SN 2021aefx in NGC 1566 on the top panel with the image size of $15\farcm0 \times 15\farcm0$ and the total integration time of 600 sec. The rising of SN 2021aefx remarked with yellow reticle is shown in the series of images (r-band) on the bottom panel. (Right) A gr-band color image of a SMBHB candidate SDSS J1430+2303 (Yellow arrow). The image size is $8\farcm0 \times 8\farcm0$ and the total integration time of $g = 3600$ sec, $r = 1080$ sec.

2.6 Summary

We present the current characteristics and performance of the KCT system in this paper. KCT is a 0.36-meter telescope installed at DeepSkyChile in Chile, which is mainly focused on the time-series observation of transients. we established the automated system of KCT using the software “ACP observatory control panel (ACP)”. ACP controls the mount, CCD, filter wheel, and focuser. The daily operation is performed by the ACP scheduler (ACPS) dispatcher based on the script-based observing plan uploaded by the user in advance. The 5σ limiting magnitude of KCT can reach $g = 18.9$ AB mag with 10 min exposure under the weather condition of FWHM$\sim 3\farcs0$, and clear night sky affected by slight moonlight. The KCT system is now participating in the time-series observation to understand the origin of transients via the monitoring of nearby galaxies and the rapid follow-up such as supernovae. We will improve its operating schedule to achieve high-cadence or for immediate ToO observation shortly.

Chapter 3

Constraints on the Progenitor System of A Type Ia SN 2019ein from the Early Light Curve

3.1 Introduction

Type Ia supernovae (SN Ia) are one of the most energetic astrophysical phenomena. Its peak luminosity reaches $L_{\mathrm{max}} \sim 10^{51}$ ergs comparable to that of a single galaxy. Many normal Type Ia SNe follow an empirical correlation between the peak luminosity and the decline rate in the B-band ($\Delta m_{15}(B)$; B-band magnitude difference between at the peak and the 15 days from the peak; Phillips (1993)). This correlation shows that fast-declining SNe tends to have faint peak luminosity, allowing us to calibrate the observed light curve (Standardization). We can measure the distance to extragalactic objects using this standardized light curve (Cosmic distance indicator) and find the accelerating expansion of the universe (Riess et al. 1998; Perlmutter et al. 1999).

Despite their importance in cosmology, however, their progenitor systems have not been identified in observation. The thermonuclear runaway of a CO WD in close binary system is mainly believed to be the explosion mechanism. Some progenitor scenarios are proposed by many studies. Whelan & Iben (1973) suggested a close binary system of a CO WD with mass close to the Chandrasekhar mass ($M_{\rm ch}$) accreting the materials from its red giant companion over the Roche lobe at the pre-supernova stage (Single degenerate scenario; SD). Deposit of hydrogen and helium shell capped on the surface of WD changes into carbon increasing the mass of the core until it reaches $M_{\rm ch}$. This can cause the runaway of nuclear reaction of carbon which lets the WD explode as an SN Ia. The donor star can also be a main sequence (MS), a sub-giant (SG), or a helium star (Pakmor et al. 2008; Han & Podsiadlowski 2004; Nomoto 1982). Woosley et al. (1986); Fink et al. (2007, 2010); Polin et al. (2019) predicted that a sub-$M_{\rm ch}$ WD of which the surface is surrounded by a helium shell from a helium companion star can also explode as SN Ia (Double detonation; DDet). A shock from the explosion of the surface ignites the carbon core or the direct ignition of a helium shell is linked to the carbon core (direct-drive). On the other hand, Iben & Tutukov (1984); Webbink (1984); Pakmor et al. (2010) suggested that double CO white dwarfs can merge by losing their orbital angular momentum with the gravitational wave and explode as SN Ia (Double degenerate; DD).

Recently, it became possible to obtain information about the progenitor from the early part of the light curve. Kasen (2010) suggested that the early bump appears on the light curve resulting from the cooling of shock-heated material from the SN ejecta-companion interaction. When the ejecta sweeps its surface away, a thermal X-ray flash occurs from the heated material. As the material cools down due to the adiabatic expansion, the wavelength of the radiation becomes longer and detectable in UV/optical bands. Its duration ranges from <a few hours to a day depending on the size of the companion. Large stars are expected to have a long duration and show a high luminosity of the cooling emission.

To find this early signature of the SN Ia explosion, many researchers give efforts for observing an early moment of SNe Ia. They gave a constraint of the progenitor ($R_{\rm p}$) or companion size ($R_{\rm c}$), giving a range of $R_{\rm p} < 0.1\,R_\odot$ (SN 2011fe; Nugent et al. 2011), $R_{\rm p} < 0.25 - 0.35\,R_\odot$ (SN 2013dy; Zheng et al. 2013), $1.5\,R_\odot < R_{\rm p} < 2.7\,R_\odot$ (SN 2012ht; Yamanaka et al. 2014), the progenitor with $R_{\rm p} \lesssim 0.1\,R_\odot$ and the companion with

$R_{\mathrm{c}} \lesssim 1.0\,R_{\odot}$ (SN 2015F; Im et al. 2015) with a possible signal of the cooling emission. There is some cases of SNe Ia showing the distinctive bumpy feature (Early excess) in their early light curves using the ejecta interaction model. Marion et al. (2016) found that SN 2012cg have the early excess and its blue $B-V$ color ($B-V \sim 0.1$) support the SD system of a $\sim 6\,M_{\odot}$ main-sequence companion star with the companion model. SN 2017cbv also shows a slightly bluer $B-V$ color than that of SN 2012cg with a $\sim 56\,R_{\odot}$ sized companion star although other explanations can be possible (Hosseinzadeh et al. 2017). In addition, iPTF14atg is a peculiar SN Ia with UV excess, which is possibly produced from a companion star with several tens of $R_{\odot}$ (Cao et al. 2015).

Figure 1 shows SN 2019ein reported by ATLAS in NGC 5353 on 2019 May 1.5 UT (Tonry et al. 2019) (MJD 58604.474). The location was reported as the J2000.0 coordinates of (α, δ) = (13:53:29.134, +40:16:31.40). Kawabata et al. (2020) estimated the size of the companion as $R_{\mathrm{c}} = 4.3 - 7.6\,R_{\odot}$, ruling out the possibility of its red giant companion. Pellegrino et al. (2020) also ruled out symbiotic progenitors and constrained its companion as a main-sequence or a slightly evolved star at accretion rates of $> 3 \times 10^{-7}\,M_{\odot}\mathrm{yr}^{-1}$ or optically thin shells around the progenitor from Very Large Array (VLA) radio observation.

In this paper, we constrain the progenitor size of SN 2019ein using our high-cadence monitoring data. We describe how the observation and data reduction were performed in section 2. We present fundamental characteristics of SN 2019ein and the companion radius estimated from the early light curve and color analysis in section 3. We discuss its possible progenitor systems in section 4.

3.2 Observation and data reduction

3.2.1 Imaging and Photometry

We performed a monitoring survey of nearby galaxies to catch a moment of supernova explosion within ~ 1 day named Intensive Monitoring Survey of Nearby Galaxies (IMSNG; Im et al. 2019). 60 galaxies having near-ultraviolet (NUV) magnitude

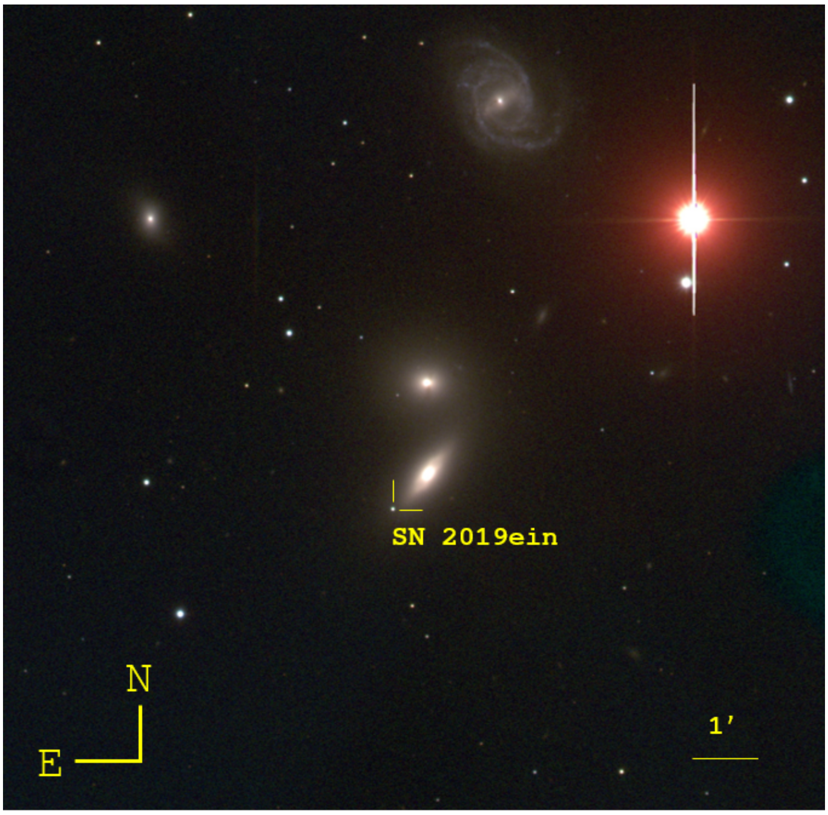

Figure 3.1. A cropped color composite image of SN 2019ein in NGC 5353. This image is composed of R-(Red), V-(Green), and B-(Blue) band images observed on 2019-06-14 (+30.06 days after B maximum) using SNUCAM at Maidanak astronomical observatory (MAO), Uzbekistan. SN 2019ein is marked as a yellow reticle. As shown in the figure, north is up and east is to the left.

($M_{\rm NUV} < -18.4\,$AB mag) at distance d$<$ 50 Mpc were selected since many massive stars emitting UV form in high star formation rate (SFR) galaxies. $BVRI$-band imaging data were obtained from 0.6-1.5 meter class telescopes at many locations in the northern hemisphere using SBIG STX-16803 camera on the 1-m telescope at Seoul national university Astronomical Observatory (SAO), SOPHIA camera on the 1-m telescope at Deokheung Optical Astronomical Observatory (DOAO), PIXIS 2048B camera on the 0.6-m telescope at Mt. Sobaek Optical Astronomy Observatory (SOAO) in South Korea, ARC camera on the 1-m telescope at Mt.Lemmon Optical Astronomical Obser-

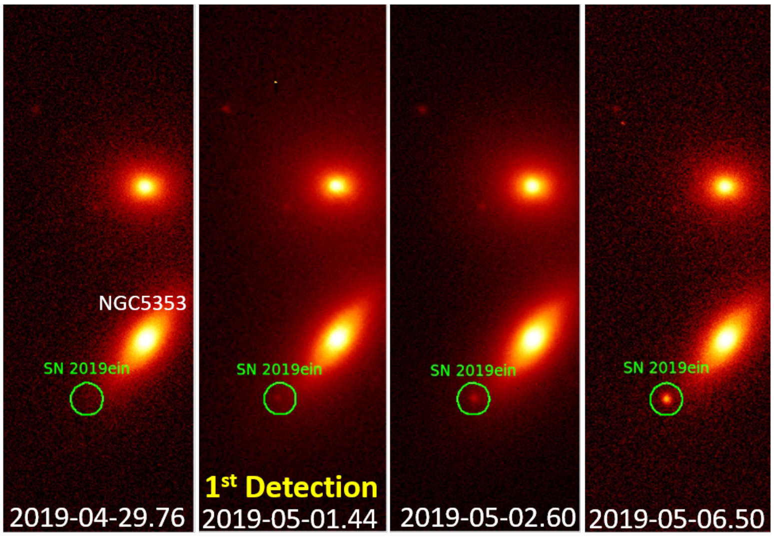

Figure 3.2. Successive R-images of SN 2019ein in NGC 5353 galaxy including the last non-detection and the first detection. The position of the supernova is in the green circle.

vatory (LOAO) at Arizona, $2k2k$ camera on the 0.8-m telescope and FLI-16803 camera on the 0.25-m Wide-field IFU Telescope (WIT) (Hwang et al. 2020) at McDonald Observatory (McD) in Texas, US, and SNUCAM installed on the AZT-22 1.5-m telescope at Maidanak Astronomical Observatory (MAO) in Uzbekistan (Im et al. 2010) with a cadence from a few hours to a day. (See table 2 in Im et al. (2019) for details.) The near-infrared (NIR) observation was also performed using the infrared wide-field camera (WFCAM on the 3.9-m United Kingdom Infra-Red Telescope (UKIRT) at Hawaii in the US. SN 2019ein was firstly detected in our LOAO BR-band images taken on 2019 May 01.44 (MJD 58604.439) in Figure 2. These data were obtained $\sim$ 50 minutes earlier than the detection with the cyan filter from Tonry et al. (2019) and 1.68 days after the last-non detection. We started our follow-up observations with the other optical and NIR wavelengths.

Standard reduction procedures (bias, dark subtraction and flat fielding) were applied using `PyRAF` (Science Software Branch at STScI 2012) and `Astropy` package in Python programming (Astropy Collaboration et al. 2013). WCS coordinates were entered using

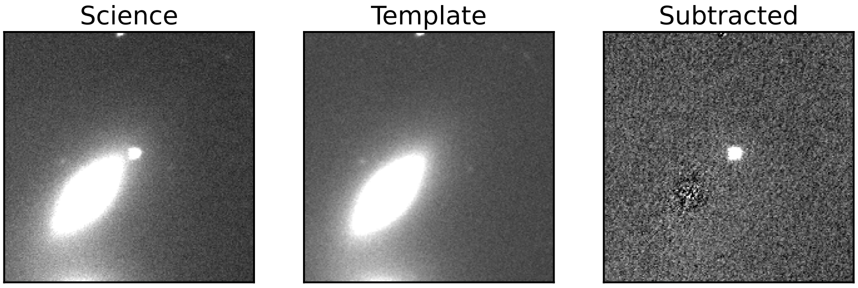

Figure 3.3. Image subtraction procedure. (left) Science image (middle) Template image (right) Science/Template subtracted image. The images were trimmed to FoV of $2.65' \times 2.65'$. SN 2019ein is located in the center of the images.

`astrometry.net` (Lang et al. 2010). When a new supernova appeared in the galaxy, we subtracted the light of the host galaxy in the science image from a template image produced in advance under the good weather condition to measure the flux of the supernova only using `hotpants` software (Becker 2015). Science images were aligned to the template using `wcsremap` and `gregister` task in `PyRAF`. We trimmed the aligned image letting the supernova on the center with the size of over 5 arcmin^2 to perform better subtraction. If there were no templates for V and I-band, we used the Panoramic Survey Telescope & Rapid Response System[*] (Pan-STARRS) and Sloan Digital Sky Survey[†] (SDSS) archival images. Figure 3 shows an example of the image subtraction procedure. For NIR data, only J band images were subtracted since there are no images for reference in HK-bands.

We performed aperture photometry with the radius of a 2×FWHM (Full-Width Half Maximum) aperture on the subtracted images using `SExtractor` (Bertin & Arnouts 1996). Flux calibration was conducted using stars from data release 9 (DR9) of the AAVSO photometric all-sky survey[‡] (APASS; Henden et al. 2012), data release 1 (DR1)

---

[*] http://ps1images.stsci.edu/cgi-bin/ps1cutouts

[†] https://dr12.sdss.org/fields

[‡] `https://www.aavso.org/apass`

of Pan-STARRS[§] (PS1), and Two Micron All Sky Survey[¶] (2MASS; Skrutskie et al. 2006) photometric catalogs for optical and NIR bands. SDSS magnitudes in the APASS catalog and Pan-STARRS magnitudes were transformed to Johnson-Cousins $BVRI$ filter system using equations in Blanton & Roweis (2007) and Tonry et al. (2012) based on the AB magnitude system. On the other hand, there are systematic differences between magnitudes measured from DOAO images and other images. We applied offset of 0.131, 0.049, 0.0, and 0.103 on each B, V, R, and I-band image adopting the method of Cho et al. (2020) by applying a linear correction factor to match measurements from each observatory.

3.2.2 Long-slit spectroscopy and classification

The optical spectrum of SN 2019ein was obtained on 2019 May 22 using a long-slit observation using the SAO 1-m telescope. This data was reduced with standard IRAF tasks. Figure 4 shows a spectrum of SN 2019ein (the coverage of 3000-9000Å) and we can identify iron (Fe), Silicon (Si), and Sulfur (S) spectral features in the spectrum. For the detailed classification, we used the `GELATO` library (Harutyunyan et al. 2008) for classification. The best match is SN Ia 1981B (Nugent et al. 1995) in phase -2 days from B maximum. SN 2019ein is close to a Type Ia supernova.

3.3 Analysis and results

3.3.1 Long-term light curve and distance to NGC 5353

A long-term light curve of SN 2019ein is presented from the $BVRIJHK$-imaging data in Figure 5. SN 2019ein data are marked differently with filters and observatories. The light curve of SN 2011fe, known as the most well-studied SN Ia ever, is over-plotted as a grey symbol (Zhang et al. 2016) for comparison. Its data points are shifted in the y-axis direction adding arbitrary constants to overlap with the maximum of SN 2019ein.

[§] `https://catalogs.mast.stsci.edu/panstarrs/`

[¶] `https://irsa.ipac.caltech.edu/Missions/2mass.html`

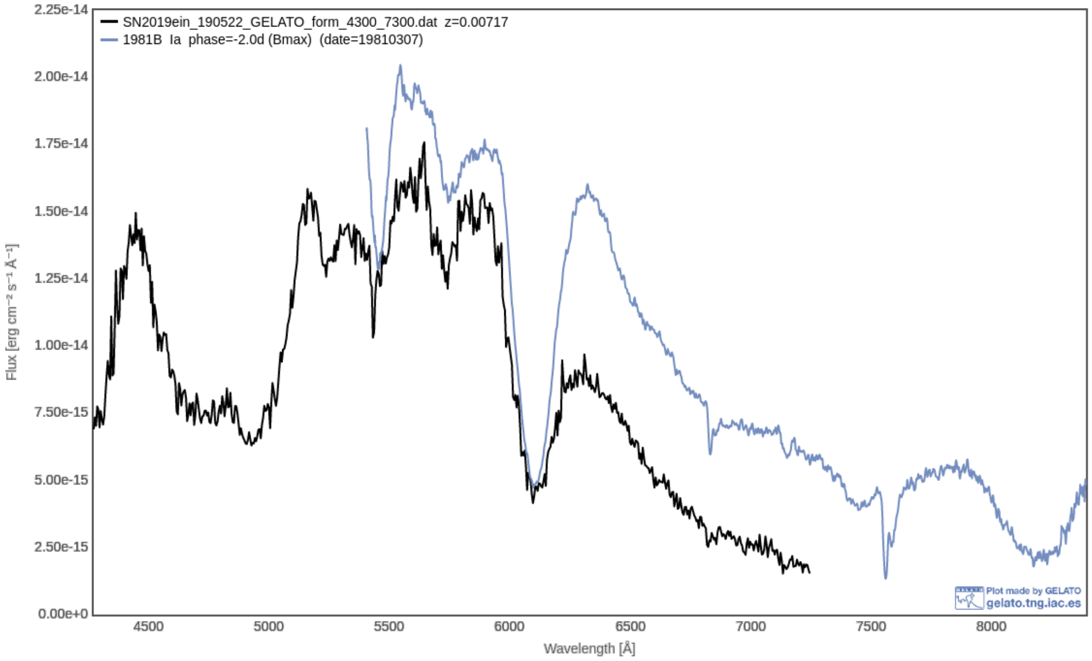

Figure 3.4. The `GELATO` best match result of SN 2019ein (Black) with SN 1981B (Blue).

For the B-band, we can find the light curve of SN 2019ein rises more steeply than that of SN 2011fe. We also plotted data from Kawabata et al. (2020). We performed the polynomial fit on the data around the peak brightness to obtain maximum dates, maximum magnitudes, and decline rates (Δm_{15}) in each filter. They are presented in Table 1, showing agreement with the measurements from Kawabata et al. (2020). Spline fit was also performed but it shows no significant difference so we adopted the former result. Using B-band parameters, we also measured host galaxy extinction with the relation of $\Delta m_{15}(B)$ - $(B_{\max} - V_{\max})$ (Equation 7; Phillips et al. 1999). The reddening value $E(B-V)_{\text{host}}$ is measured as 0.088±0.042 from the observed $(B-V)$ color at maximum[‖]. Two measurements are consistent with those estimated from Kawabata et al. (2020) within the uncertainty, suggesting the small amount of extinction from the host galaxy.

[‖] To prevent confusion, we note that $B_{\max} - V_{\max}$ means the difference between B-band magnitude at B maximum and V-band magnitude at V maximum

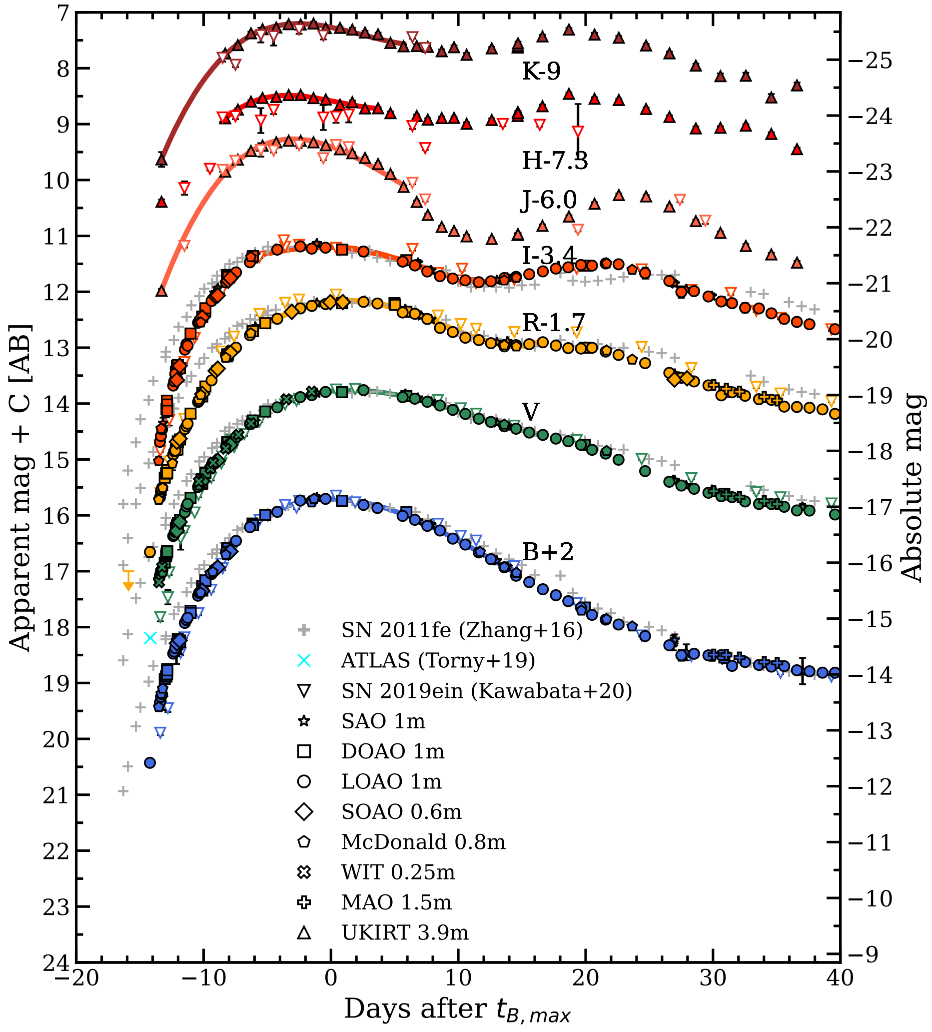

Figure 3.5. Long-term light curve of SN 2019ein up to 30 days after *B*-band maximum. Each symbol shows the observatories where the data were obtained. SN 2011fe data from Zhang et al. (2016), SN 2019ein data from Kawabata et al. (2020), and the polynomial fit are overplotted as gray crosses, inverted triangles, and solid lines. Milky way and host galaxy reddening are corrected.

Table 1. Polynomial fit results of the SN 2019ein light curve.

Band	Max. Date (MJD)	Max. Magnitude (AB mag)	Δm_{15} (mag)
B	58618.651±0.164	14.071±0.009	1.393±0.027
V	58620.147±0.105	14.020±0.008	0.813±0.015
R	58620.081±0.204	14.070±0.008	0.738±0.059
I	58617.246±0.271	14.703±0.013	0.613±0.021
J	58615.870±0.217	15.347±0.017	-
H	58615.468±0.175	15.833±0.008	-
K	58616.324±0.245	16.225±0.013	-

We examined SN 2019ein is close to a normal SN Ia. We used the distance to NGC 5353 as the mean value of 37.22 ± 3.12 Mpc considering the measurements having the uncertainty from the NASA/IPAC Extragalactic Database (NED)[**]. This value gives us the peak absolute B magnitude of -19.14 ± 0.18 mag. Figure 6 shows the location of SN 2019ein on the relation between the peak absolute magnitude and the B-band decline rate with many other SNe Ia from the Harvard-Smithsonian Center for Astrophysics (CfA3) data (Hicken et al. 2009). Normal SNe Ia follow the Phillips relation (a black solid line) including SN 2011fe (Zhang et al. 2016). We found SN 2019ein is on the Phillips relation, giving us the absolute magnitude ($M_{\rm B,max}$) as -19.135±0.027. The uncertainty of $M_{B,max}$ is a standard deviation of the bootstrap resampling ($N = 10000$). The distance modulus is measured as 32.847±0.028 mag, which allows us to estimate the distance to NGC 5353 as 37.098±0.486 Mpc.

We also obtained detailed parameters using SALT2 fitting from `SNCosmo` library (Barbary et al. 2016). The fitting result is presented in table 2 including Milky Way

---

[**] http://ned.ipac.caltech.edu/

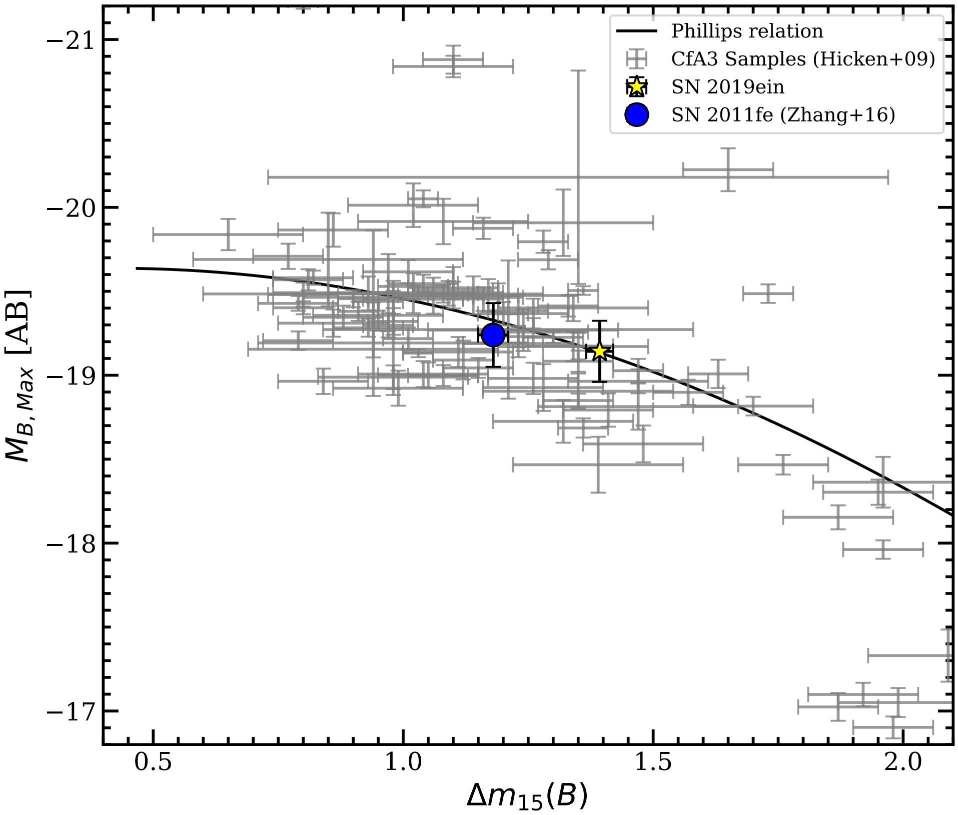

Figure 3.6. The location of SN 2019ein in the peak absolute magnitude-width relation. SN 2019ein (a yellow star) is marked with SN 2011fe (a blue-filled circle) as a typical SN Ia. CfA3 supernovae (gray) are over-plotted. Normal SN Ia follows Phillips relation (black solid line).

reddening. Considering $M_{\rm B,max} \sim -19.4$ and $\Delta m_{15} \sim 1.1$ of SN 2011fe (adopted from Im et al. (2015)) as typical values, SN 2019ein is a slightly sub-luminous normal SN Ia. This result is consistent of the previous results (Kawabata et al. 2020; Pellegrino et al. 2020).

Table 2. SALT2 (`SNCosmo`) fit results

Parameter	Value	Uncertainty
x_0	0.027	$\pm$0.001
x_1	-1.567	$\pm$0.031
c	0.150	$\pm$0.101
$\Delta m_{15}(B)$	1.456	
μ	32.263	
$t_{\mathrm{B,max}}$	58619.295	$\pm$0.021
B_{max}	14.047	
$M_{\mathrm{B,max}}$	-18.216	
$E(B-V)_{\mathrm{MW}}$	0.011	
$E(B-V)_{\mathrm{host}}$	-0.098	$\pm$0.023
χ^2_ν	0.838	

3.3.2 The first light time (t_{fl}) & Early light curve

To constrain the radius of the progenitor system, we performed the two-component model fit of the shock-heated cooling emission (Kasen 2010; Rabinak & Waxman 2011) models and a simple power-law after we determine the first light time when the radioactive ^{56}Ni decay-powered light curve starts to rise with two cases. Here, we converted a power-law model into the magnitude form like the equation (1).

$$M(t) = M_0 - 2.5\alpha \log_{10}(t - t_{\mathrm{fl}}), \tag{3.1}$$

where $M(t)$ is the magnitude as a function of time t, M_0 is the normalization factor of the magnitude, t_{fl} is the first light time, and α is the power-law index.

For Kasen (2010) model,

$$L(t) = 2.0 \times 10^{40} \frac{R_{10} M_c^{1/4} v_9^{7/4}}{\kappa_{0.2}^{3/4}} t_{\mathrm{day}}^{-0.5} \ \mathrm{erg\ s^{-1}}. \tag{3.2}$$

For Rabinak & Waxman (2011) model,

$$L(t) = 1.2 \times 10^{40} \frac{R_{10} E_{51}^{0.85}}{M_c^{0.69} \kappa_{0.2}^{0.85} f_{\mathrm{p}}^{0.16}} t_{\mathrm{day}}^{-0.31} \ \mathrm{erg\ s^{-1}}. \tag{3.3}$$

$L(t)$ is the bolometric luminosity of the early shock-heated cooling emission as the function of time, t. t is units of day. R_{10} is the radius of the progenitor or companion star in units of $10^{10}\,\mathrm{cm}$ or $R_{10} = R_*[\mathrm{R_\odot}]/10^{10}\,\mathrm{cm}$, M_c is the progenitor mass in units of the Chandrasekhar mass. v_9 is the velocity of the expanding SN ejecta in units of $10^9\mathrm{cm\,s^{-1}}$. $\kappa_{0.2}$ is the opacity in units of $0.2\,\mathrm{cm^2\,g^{-1}}$. f_{p} is the form factor ranging from 0.031 to 0.13. See Im et al. (2015) in details for the parameters. We adopted the values of $M_c = 1/1.4$, $\kappa_{0.2} = 1.0$, $v_9 = 1.0$.

For the case (1), we determined t_{fl} to be forced to be one value for all four bands using only a simple power-law model, since the explosion occurs at a specific time. We use the chi-square minimization method to find 9 parameters of m_0, α in each band, and t_{fl}. The weight is given as $1/\sigma_{mag}^2$ and σ_{mag} is an uncertainty of magnitudes. We used 53 data points for the first 8.3 days in each band simultaneously, a total of 212 data points. Each panel of Figure 7 and Table 3 show the results of our fit in each optical band. t_{fl} is determined as MJD 58603.185 ± 0.087. The rise time, t_{rise}, is also measured as 15.466 ± 0.186 days. Reduced chi-square (χ^2_ν) is calculated as 3.32 for the simple power-law fit only. χ^2_ν values of two component model fit are 1.295, 2.003, 3.303, and 5.109 for each band.

Considering the power indices including the first data, the expanding fireball model ($\alpha = 2$) (Arnett 1982; Riess et al. 1998; Nugent et al. 2011) explains the light curve well. For this case, the companion star is large as $0.168 \pm 0.094\,R_\odot$, $0.244 \pm 0.045\,R_\odot$ in B-, R-band ($\sim 0.2\,R_\odot$).

Second, we fit the data points of the first 8.3 days in each band separately, given four t_{fl} values in the case 2 in Table 3 and Figure 8. B-, R- and I-band curves are also explained by the expanding fireball model well ($t^{\sim 2}$). We estimated the radius of the companion as $0.577 \pm 0.142\,R_\odot$, $0.921 \pm 0.144\,R_\odot$ in B-, R-bands.

3.3.3 Early color evolution

Due to the high temperature of the shocked ejecta, the shock-heated cooling emission is expected to be bluer in the early phase than in the later phase. Figure 9 (right) shows the $B - V$ color evolution of SN 2019ein from -17.5 to -3 days from the B maximum. We used data points with $\sigma_{B-V} < \sqrt{0.1^2 + 0.1^2}$. The color curve of SN 2011fe (Black open squares) is over-plotted for comparison. To compare our data with the expected color curve model, we combined the Kasen (2010) model to the pulsational-delayed-detonation (PDD) model from Dessart et al. (2014).

The phase of both supernovae are stretched each other using stretch parameter, s, calculated as 0.854 for SN 2019ein and 0.955 for SN 2011fe ($s = \frac{1.7}{\Delta m_{15}(B)+0.6}$) (Perlmutter et al. 1997). SN 2011fe is known to have very weak shock-heated cooling emission due to the non-detection of g-band 4 hours after the first light time (Bloom et al. 2012). The Kasen (2010) model is plotted as a dotted line with different colors. Then we can regard the color of SN 2011fe as the non-interaction case in the Kasen (2010) model. The color of SN 2019ein is very similar to that of SN 2011fe, suggesting that

Table 3. (1) Resultant parameters of χ^2 minimization when $t_{\rm fl}$ is force to be a one value. (2) The same in (1) but after estimating $t_{\rm fl}$ in each band, adopting the mean value $\langle t_{\rm fl} \rangle$ as $t_{\rm fl}$.

Band	α	m_0	$t_{\rm fl}$	χ^2_ν	$R_*[R_\odot]$	χ^2_ν
Case (1)						
B	1.929±0.039	18.829±0.110	58603.185±0.087	3.398		1.295
V	1.690±0.035	18.433±0.096			0.168±0.094	2.003
R	1.851±0.040	18.862±0.107			0.244±0.045	3.303
I	1.934±0.040	19.373±0.109				5.109
Case (2)						
B	1.909±0.006	18.774±0.013	58603.226±0.575			1.276
V	1.713±0.013	18.470±0.027			0.577±0.142	1.890
R	1.927±0.019	19.023±0.042			0.921±0.144	2.777
I	1.915±0.010	19.322±0.020				4.954

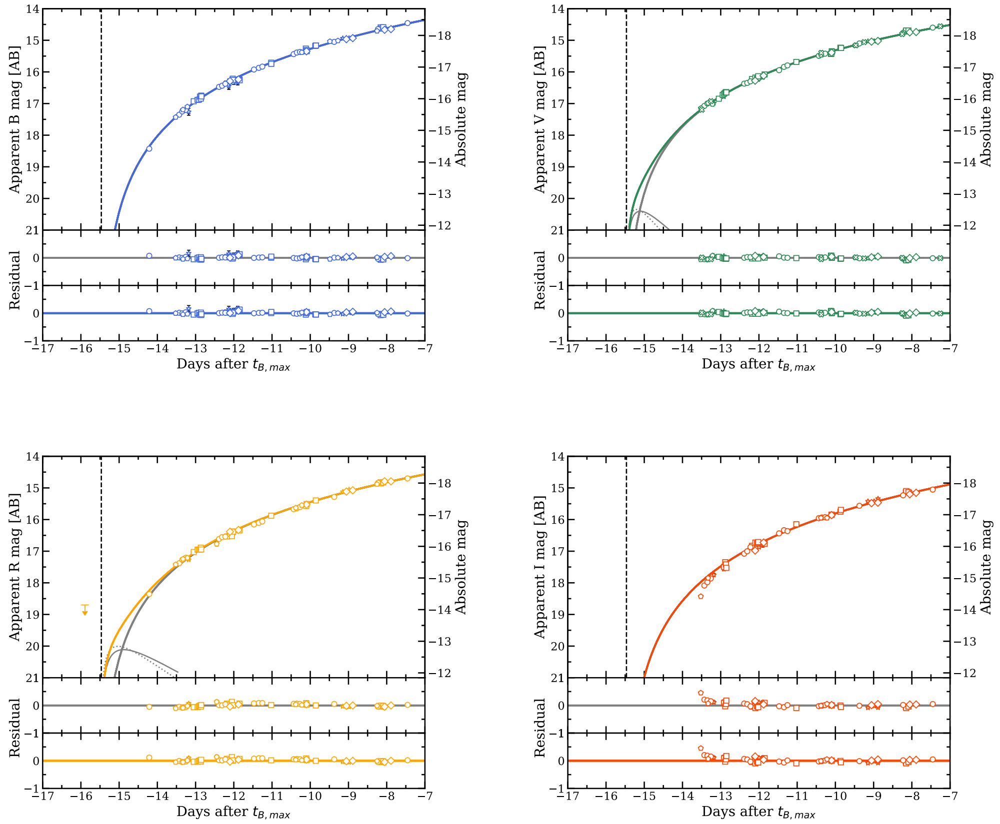

Figure 3.7. The case (1) that $t_{\rm fl}$ is estimated as one value (Black vertical dashed line) after a simple power-law fitting considering all bands simultaneously. The early light curve of SN 2019ein from -17 to -7 days after B-maximum is shown. Each symbol is the same as the Figure 5. The R-band 5-σ detection limit is from SAO data marked as an orange arrow. The single power-law fitting line (Thick gray solid line) is also plotted. Thin gray solid and dotted lines are the expected light curves of the shock-heated cooling emission from the models of Kasen (2010) and Rabinak & Waxman (2011) corresponding to the companion size of $0.168 \pm 0.094\, R_\odot$ (V-band) and $0.244 \pm 0.045\, R_\odot$ (R-band). Colored lines are the combined model fit of Kasen (2010) and simple power-law models.

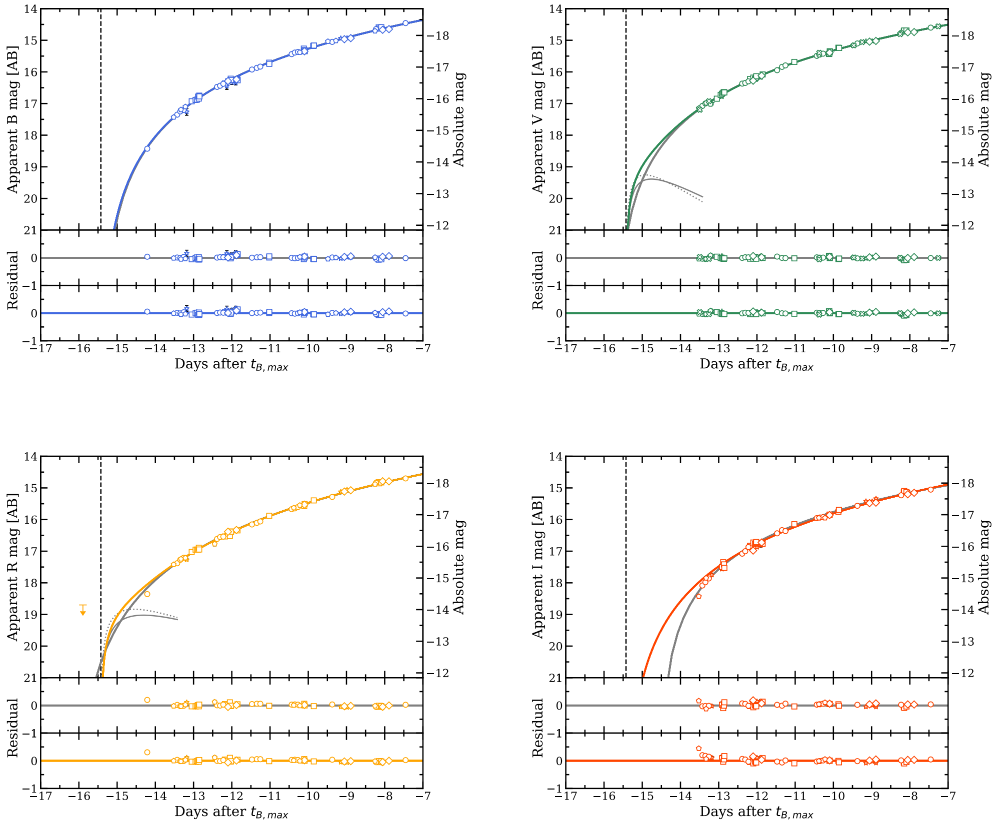

Figure 3.8. The case (2) that the mean value of $t_{\rm fl}$ in each band is adopted as $t_{\rm fl}$ (Black vertical dashed line). Symbols and colors follow the same manner in Figure 7 but the expected light curves of the shock-heated cooling emission from Kasen (2010) and Rabinak & Waxman (2011) are from the companion star with a radius of $0.577 \pm 0.142\,R_\odot$ (V-band) and $0.921 \pm 0.144\,R_\odot$ (R-band).

SN ejecta-companion interaction is not significant.

Furthermore, early color evolution can distinguish between different models such as the double detonation scenario or SN ejecta-companion model (Bulla et al. 2020). Here, we present the $B-V$, $B-R$, $V-R$, and $V-I$ color evolution of SN 2019ein from −15 to 65 days after the B-band maximum. Colors of SN 2011fe known as a typical normal type Ia with little host extinction are overplotted. Milky way and host galaxy extinction

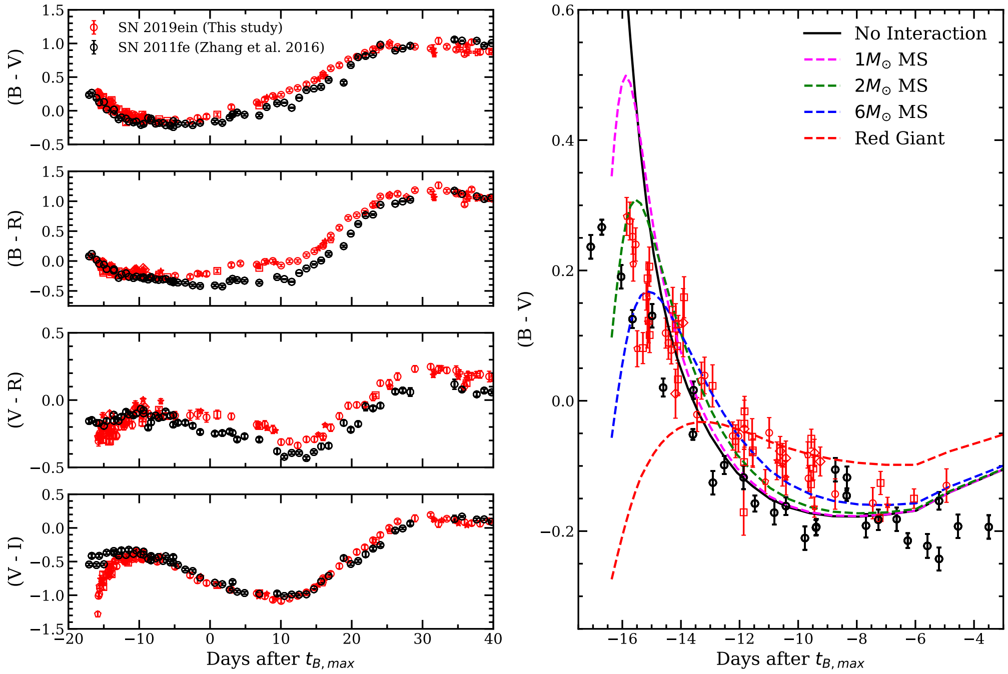

Figure 3.9. (left) $B-V$, $B-R$, $V-R$, and $V-I$ long term color evolution of SN 2019ein (red symbols) and SN 2011fe (black circle) for comparison ranging from -20 to 40 days after B maximum. Each symbol of SN 2019ein is the same in figure 2. (right) The early phase of the $B-V$ color from -18 to -5 days after the B maximum. Model color curve (Kasen (2010) + PDDEL model) is also over-plotted depending on the size (mass) of the companion star of $1\,M_{\odot}$, $2\,M_{\odot}$, $6\,M_{\odot}$, red giant (Magenta, Green, Blue, Red dashed line), and no interaction with SN ejecta (Black solid line).

are corrected for all SNe. Their overall shapes are similar to each other. Bulla et al. (2020) suggested that the color change from blue to red, and to blue again describes the helium shell burning of a white dwarf in the double-detonation scenario from the model (a red bump) despite in $g-r$ color. However, the $B-R$ and $V-R$ colors of SN 2019ein do not show this color inversion in the early phase. This suggests that the progenitor of SN 2019ein was not likely to have a helium shell (if exists, it would be thin as $M_{\mathrm{He}} < 0.01\,M_{\odot}$).

3.4 The progenitor system of SN 2019ein

We cannot find a distinctive signature of the shock-heated cooling emission on the early light curve. From the least-square fitting of the early light curve, the maximum size of the companion star can be $1.2 \pm R_{\odot}$. For this case, we assumed the optimal viewing angle, which gives a maximum signal of the emission. If the viewing angle is off-axis from the optimal angle, the shock-heated cooling emission would be dimmer than that from the optimal angle. We could not detect any excessive flux even at this optimal angle. We now discuss the possible progenitor system of SN 2019ein.

First, if the exploding star is close to M_{ch}-mass WD, evolved stars such as sub-giants, red-giants, and red super-giants can be ruled out. This is agreed with the result of Kawabata et al. (2020) but we can give a constraint on less evolved stars such as the main sequence ($\sim 1\,R_{\odot}$). Their estimation ranges $4.3 - 7.6\,R_{\odot}$ by scaling the luminosity of SN 2019ein at 1.9 days from the explosion following the manner of Nugent et al. (2011). The discrepancy in the estimated radius may be due to difference between our method and Kawabata et al. (2020).

Secondly, for mergers of two CO WDs with a long-delayed time, the size of the progenitor system is assumed as $\sim 0.01\,R_{\odot}$ Yoon et al. (2007). For the violent merger, the massive CO WD binary with the mass ratio close to ~ 0.8 can produce a normal SNe Ia (Pakmor et al. 2012) in a grid box size of $\sim 0.05\,R_{\odot}$. These systems can be plausible considering our upper limit of the size.

If sub-M_{ch} WD has a He-shell with non-degenerate donor star(double detonation), Polin et al. (2019) expected there should be a red bump in the early color curve which its extent of redness depends on the thickness of He shell. If He-shell is thick ($M_{\mathrm{He}} > 0.01\,M_{\odot}$), strong early excess in the light curve and red bump can be detected together. However, this case is not likely since SN 2019ein did not show both signatures (Figure 7, Figure 8, and the right panel of Figure 9).

3.5 Summary

We performed optical (from -14.2 to +130 days after $t_{\mathrm{B,max}}$) and NIR observations (from -13.3 to +60 days after $t_{\mathrm{B,max}}$) of SN 2019ein. Its location of the luminosity-width relation show that SN 2019ein is a normal SN Ia supernova which is agreed with the previous result. SALT2 fitting shows a consistent result despite its lower estimation of the luminosity in the B-band. The distance to its host galaxy NGC 5353 is measured as 37.098 ± 0.028 Mpc using the decline rate in B-band. In the early light curve, we could not identify the blue excess that is believed to be an interaction between SN ejecta and its non-degenerate companion star with a size smaller than $\sim 1.0\,R_\odot$. We found that the $B-V$ color of SN 2019ein is very similar to that of SN 2011fe. In addition, we find no red bump at early $V-R$ and $B-R$ color (until 7 days after the explosion) accumulated around its exploding WD, disfavoring DDet model or very thin He shell ($M_{\mathrm{He}} < 0.01\,M_\odot$). As a result, we can constrain the progenitor system below.

For the single degenerate scenario,

1. The exploding CO WD with close to M_{ch} and a main sequence companion with the radius of $\sim 1.0\,R_\odot$.
2. Sub-M_{ch} CO WD surrounded by thin ($M_{\mathrm{He}} < 0.01\,M_\odot$) helium shell and its non-degenerate star (He star?).

For the double degenerate system, we can include these systems considering our detection limit,

1. The long-delayed time($\sim 10^5$ years) merger of two CO WDs with $\sim 0.01\,R_\odot$.
2. The violent merger of massive CO WDs (including the system with the mass ratio ~ 0.8) with its material expanding up to $\sim 0.1\,R_\odot$)

Although studies to probe the SNe Ia progenitors using very early spectra are rising these days, the high-cadence survey using small telescopes is still a powerful tool for finding observational evidence of their progenitors. To improve their performance for detecting the shock-heated cooling emission, robotic operation and establishing their networking system are also required. For distinguishing other explosion models, the early color curve can be also a useful method.

Chapter 4

The Early Light Curve of A Type Ia SN 2021hpr in NGC 3147 : Progenitor Constraints with The Companion Interaction Model

4.1 Introduction

The progenitor of Type Ia supernovae (SNe Ia) is expected as a close binary system of a carbon/oxygen white dwarf (WD). One of two leading models is the single degenerate (SD) model, which suggests SNe Ia explosion can result from thermonuclear runaway on the WD when the matter from its non-degenerate donors such as a main-sequence (MS), a subgiant (SG), a red giant (RG), or a helium star transfers its material over the Roche-lobe until the mass of WD approaches the Chandrasekhar-mass of $M_{\rm ch} \sim 1.4\,M_{\odot}$ (Whelan & Iben 1973; Nomoto 1982; Iben & Tutukov 1984; Hachisu et al. 1996; Wang et al. 2014). The other model, the double-degenerate (DD) model, expects that a binary WD system can merge via emitting the gravitational wave radiation and become an SN Ia (Iben & Tutukov 1984; Webbink 1984). SNe Ia are used as a distance indicator in that they have an empirical relation between the width of the light curve and the peak luminosity (Width-Luminosity relation; Phillips 1993). This allows SN Ia to be a good tool as a standardizable candle for measuring the distance and probing the accelerating expansion of the universe (Riess et al. 1998).

Despite its usefulness, observational evidence of their progenitors is still in debate. One of the ways to constrain the progenitor system is to detect the shock-heated cooling emission (SHCE) in the early time light curve of SNe after the shock-breakout (Kasen 2010; Rabinak & Waxman 2011; Piro & Nakar 2013). For the SD scenario, materials in the ejecta are heated by the shock which is produced from the collision between the ejecta and companion star (Kasen 2010). While the ejecta expands and cools down, the emission (SHCE) can be detected at the ultraviolet(UV)/optical wavelengths. The brightness and duration of the SHCE depend on the radius of the companion and the viewing angle from the observer. For a $1\,M_{\odot}$ MS companion, the SHCE would be peaked at $B = -14$ AB magnitude while an RG companion ($\sim 143\,R_{\odot}$) would produce it with $B \sim -18$ AB magnitude on a day after the explosion. This emission appears as "early excess" on the rising part of the standard SNe Ia light curve.

Many theoretical studies have been performed to describe this early excess in the SN Ia light curve. If a sub-$M_{\rm ch}$ WD has a helium shell, the helium detonation can induce a shock wave traversing the carbon/oxygen core and trigger the second detonation (Double detonation or DDet; Woosley et al. 1986). Sub-$M_{\rm ch}$ CO WD with a thin helium shell model ($< 0.1\,M_{\odot}$) is favored in many recent simulations (Fink et al. 2007, 2010; Pakmor et al. 2013; Polin et al. 2019) to explain a significant fraction of sub-luminous and normal SN Ia events. In Polin et al. (2019), the excessive flux in the early phase ($\lesssim 5\,$days since explosion) shows a red color peak ("red bump" in Polin et al. (2019)) in the early color evolution.

Piro & Morozova (2016) predicted the early excess of SNe Ia with the various distribution of the radioactive nickel (^{56}Ni) in the exploding WD and the presence of circumstellar material (CSM) around the primary WD. Shallow ^{56}Ni distribution (Highly mixed) and extended CSM density can show a bluer color evolution in the early phase.

A recent model suggests the early excess can also be seen in the DD system. Levanon et al. (2015) predicted that a UV/Blue early emission can result from the interaction of SN ejecta and disk-originated matter (DOM), which forms an accretion disk surrounding the primary WD after the companion WD is tidally-disrupted. In general, the SHCE is weak and lasts only a few hours to days.

Observationally, the diversity of the SNe Ia early light curves has been shown and many of them failed to detect the SHCE and therefore disfavoring the SD scenario. Nugent et al. (2011) constrained the progenitor radius of SN 2011fe as $< 0.1\,R_\odot$ with the fireball model (t^2). Bloom et al. (2012) gave a tight constraint of the progenitor size as $< 0.02\,R_\odot$ and the companion star size as $< 0.2\,R_\odot$ using the detection limit of 4 hours after the explosion, favoring a DD system. Some studies left a possibility of the SD model ruling out a red-giant companion for SN 2012ht (Yamanaka et al. 2014), SN 2017cfd (Han et al. 2020), and SN 2019ein where no early excess was reported (Kawabata et al. (2020) and Lim et al., in prep.).

However, there are a number of studies showing a signature of early excess. Marion et al. (2016) constrained the companion mass of SN 2012cg to 6 $M_\odot$ MS binary companion using its early light curve and color evolution together with the evidence of the DD system (Liu & Stancliffe 2016; Shappee et al. 2018). Hosseinzadeh et al. (2017) detected the blue bump of SN 2017cbv inferring the presence of its subgiant companion of 56 $R_\odot$, although there is an aspect that the companion model does not fully describe the data. Im et al. (2015) found a possible signal (2σ) of SHCE of SN 2015F from intense monitoring of nearby galaxies. Furthermore, Levanon & Soker (2019) suggested the DOM model can explain a linearly-rising flux at the early time of SN 2018oh better than the companion model. iPTF14atg (Cao et al. 2015) and MUSSES1604D (Jiang et al. 2017) with the early UV flash and red bump are classified as a peculiar and a normal event with other peculiar features. SN 2018aoz (Ni et al. 2022) and SN 2021aefx (Ashall et al. 2022; Hosseinzadeh et al. 2022), two normal SN Ia, are recently studied showing the early excess which is tried to explain its origin with diverse explanations.

Clearly, there is a need for more early light curve samples to better understand the SNe Ia progenitor system.

Another way to constrain the progenitor model of SNe Ia is to detect spectral features resulting from the companion matter stripped/ablated by the ejecta (Wheeler et al. 1975; Chugai 1986). These features include Balmer lines (e.g., Hα) and helium emission lines in optical and they should be seen after the supernova enters the nebular phase ($\gtrsim 200$ days; Botyánszki et al. 2018). Marietta et al. (2000) predicted the mass of stripped matter with an numerical simulation as $0.15 - 0.17\,M_{\odot}$ for an MS (820 km/s), SG (890 km/s), and $0.53 - 0.54\,M_{\odot}$ for an RG companion star. Meng et al. (2007) also obtained a similar result. Many studies have investigated nebular spectra of SNe Ia, but estimating the mass of unbound material has been challenging (Leonard 2007; Lundqvist et al. 2015; Tucker et al. 2019). Maguire et al. (2016) found the possible Hα emission for SN 2013ct (corresponding to $\sim 0.007\,M_{\odot}$) but no detection for the other 10 SNe Ia. Motivated by this, we also performed the late phase spectroscopy of SN 2021hpr using the 9.2 m Hobby-Eberly Telescope (HET) to find Balmer emission lines.

The observation method and data reduction procedure are described in section 2. Next, photometry and spectra analysis including early light curve are presented in sections 3-4. From this result, we discuss the progenitor system of SN 2021hpr in section 5. The summary is in section 6. We use H_0 value of 70 km s^{-1} Mpc^{-1} (Hicken et al. 2009; Planck Collaboration et al. 2016). We also neglect the $K-$ correction in our analysis since the redshift of NGC 3147 is very low at $z = 0.009346$ (Tomasella et al. 2021).

4.2 Observation & Data reduction

4.2.1 Imaging Observation

The discovery of SN 2021hpr was reported on 2021 April 2.45 UT by Koichi Itagaki (Itagaki 2021), and classified as a SN Ia by Tomasella et al. (2021). Here, we report the analysis of the SN 2021hpr early light curve using our data as well as reported data from other groups such as Caucasian Mountain Observatory (CMO; Tsvetkov et al. 2021) and the Zwicky Transient Facility (ZTF; Bellm et al. 2019) to constrain its progenitor star system property.

Most of the data come from the Intensive Monitoring Survey of Nearby Galaxies (IMSNG; Im et al. 2019). IMSNG observes 60 nearby galaxies with a high cadence of $\lesssim$ a day to detect the early emission from the shock-heated material of supernovae. Our regular monitoring observation provides the data to the 5σ depths of 19.5 mag for a point source detection using a network of $0.4 - 1.0$ meter class telescopes around the world.

NGC 3147 has been monitored by IMSNG since 2014 in B- and R-bands. In our data, SN 2021hpr was first identified in B- and R-band images taken on 2021 April 1.29 (UT) with the 1-m telescope of the Mt. Lemmon Optical Astronomy Observatory (LOAO; Im et al. 2019), located in the USA, after the last non-detection in 2021 March 31.18 with an upper limit of $R = 19.62$ AB mag. Our first detection epoch precedes the discovery epoch of Itagaki (2021) by 1.1 days. The IMSNG data were taken nearly daily in the beginning, and then several times a day since the SN discovery up to +30 days from the B-maximum brightness of SN 2021hpr using $BVRI$-bands. In addition to the LOAO 1.0-m telescope, we used the 0.6-m telescope at Mt.Sobaek Optical Astronomy Observatory (SOAO), the 1.0-m telescope at Seoul national university Astronomical Observatory (SAO), the 0.6-m telescope at Chungbuk National University Observatory (CBNUO), and the 1.0-m telescope at Deokheung Optical Astronomy Observatory (DOAO) in Korea (Figure 1). Only BVR-band data were obtained at CBNUO and with SNUCAM (Im et al. 2010) on the 1.5-m telescope at the Maidanak Astronomical Observatory (MAO; Ehgamberdiev 2018). Refer to Table 2 in Im et al. (2019) and Table 1 in Im et al. (2021) for a detailed description of the facilities. For the SAO observation, we use the Finger Lake Instrumentation (FLI) KL4040 sCMOS camera. Each single exposure time varies with the observatory from 60 to 180 seconds.

Standard reduction (bias, dark subtraction, and flat fielding) procedures were applied to the observed data using the `PyRAF` (Science Software Branch at STScI 2012) and the `Astropy` package (Astropy Collaboration et al. 2013). Additionally, we made a fringe pattern correction from the LOAO I-band data. The astrometry calibration was conducted using `astrometry.net` (Lang et al. 2010).

We performed photometry on stacked images taken consecutively at a similar epoch (3 to 5 frames). The observation time of each combined image is defined as the median of the observing start times of each single frame used for stacking. The photometric calibration was conducted using stars from data release 1 (DR1) of Pan-STARRS[*] (PS1). Calibration stars were selected as follows.

(i) Sources after removing extended sources, QSO, variables, and transients flagged from the PS1 catalog within the field of view of each image. For CBNUO, we used stars around the image center within a radius of 75% of the field of view to avoid systematic errors from the image edge.

(ii) Sources with `i_PSFmag`−`i_Kronmag`< 0.05 were classified as stars from galaxies[†]. The PS1 magnitudes were transformed into the Johnson $BVRI$ system using an equation (6) in the form of $y = B_0 + B_1 x$, where the coefficients B_0 and B_1 are provided in table 6 in Tonry et al. (2012) for the $BVRI$ system. So we use equations below.

$$(B - g_{PS1}) = 0.213 + 0.587(g - r)_{PS1}\,(\sigma_B = 0.034), \tag{4.1}$$

$$(V - r_{PS1}) = 0.006 + 0.474(g - r)_{PS1}\,(\sigma_V = 0.012), \tag{4.2}$$

$$(R - r_{PS1}) = -0.138 - 0.131(g - r)_{PS1}\,(\sigma_R = 0.015), \tag{4.3}$$

$$(I - i_{PS1}) = -0.367 - 0.149(g - r)_{PS1}\,(\sigma_I = 0.016), \tag{4.4}$$

(iii) Next, we selected stars with the transformed magnitudes ranging[‡] from 13.5

---

[*] `https://catalogs.mast.stsci.edu/panstarrs/`

[†] https://outerspace.stsci.edu/display/PANSTARRS/How+to+separate+stars+and+galaxies

[‡] bright sources in PS1 catalog are known to be saturated from 13.5th magnitude (Magnier et al. 2013). The magnitudes of detected sources in our facilities start to disperse fainter than 17th magnitude.

to 17 with signal-to-noise larger than 10 and SExtractor `FLAG`=0. The magnitude zero points and their errors were taken as the mean and standard deviation of the zero points from different reference stars. Typical zero-point errors are 0.005 to 0.185 magnitudes depending on filters and weather conditions. For CMO data in the SDSS filter system, *gri*-band magnitudes were transformed into the *BR*-band magnitudes using the equations in table 2 in Blanton & Roweis (2007).

$$B = g + 0.2354 + 0.3915[(g - r) - 0.6102]\,(\sigma_{g-r} = 0.15), \tag{4.5}$$

$$V = g - 0.3516 - 0.7585[(g - r) - 0.6102]\,(\sigma_{g-r} = 0.15), \tag{4.6}$$

$$R = r - 0.0576 - 0.3718[(r - i) - 0.2589]\,(\sigma_{r-i} = 0.10), \tag{4.7}$$

$$I = i - 0.0647 - 0.7177[(i - z) - 0.2083]\,(\sigma_{i-z} = 0.10), \tag{4.8}$$

We used the V-band magnitude presented in Tsvetkov et al. (2021). For ZTF photometry, we firstly converted g_{ZTF}-, and r_{ZTF}-band magnitudes into the PS1 filter system using the equations in Medford et al. (2020). These equations are expressed in terms of g_{PS1}, r_{PS1} in this study.

$$g_{PS1} = 0.948 g_{ZTF} + 0.052 r_{ZTF} + 0.011\,(\sigma_g = 0.004), \tag{4.9}$$

$$r_{PS1} = 0.076 g_{ZTF} + 0.924 r_{ZTF} + 0.004\,(\sigma_r = 0.063), \tag{4.10}$$

These ZTF-to-PS1 converted magnitudes were again transformed into the BVR-band magnitudes in the same way as above. All the magnitudes are based on the AB system. In addition, we calibrated the magnitudes between LOAO and other 3 telescopes (DOAO, CBNUO, SAO) which show slight offsets by adding a magnitude shift. The magnitude shift was calculated by subtracting LOAO magnitude from the DOAO, CBNUO, SAO magnitudes near the SN brightness peak (Table 1).

Table 1. Magnitude offsets ($\mathrm{Mag}_{\mathrm{LOAO}} - \mathrm{Mag}_{\mathrm{Telescopes}}$) for 3 telescopes in each band.

	DOAO (*mag*)	SAO (*mag*)	CBNUO (*mag*)
B	-0.140	-0.043	0.019
V	-0.105	-0.054	-0.078
R	-0.124	-0.096	-0.107
I	-0.109	0.025	

We subtracted a reference image from science images using `HOTPANTS` (Becker 2015), where reference images had been created in advance using images taken with the same telescope and instrument under the best observing conditions. Aperture photometry was performed on the subtracted images using `SExtractor` (Bertin & Arnouts 1996) with an aperture diameter of 3×Full Width Half Maximum (FWHM) of the Point Spread Function (PSF).

4.2.2 Spectroscopy

To confirm the SN 2021hpr classification and examine the time evolution of the spectrum, we performed long-slit spectroscopy on 2021 April 6, 14, and May 2 at SAO. We used the Shelyak LISA spectrograph[§] with the grating size of 300 g/mm and the $2''.47$ (50 μm) width slit. We placed the slit not to include the nucleus of NGC 3147 to avoid contamination. Ne lamp was used for the wavelength calibration. Flux calibration was conducted using two standard stars, HR 4554 (A0V) and BD+75d 325 (O5P). The second and third epochs spectra show typical spectral features of SNe Ia such as Si II, Mg II, and Fe II absorption lines with no hydrogen emission line. Applying GEneric cLAssification TOol (GELATO; Harutyunyan et al. 2008) on the April 14 spectrum

---

[§] `https://www.shelyak.com/description-lisa/?lang=en`

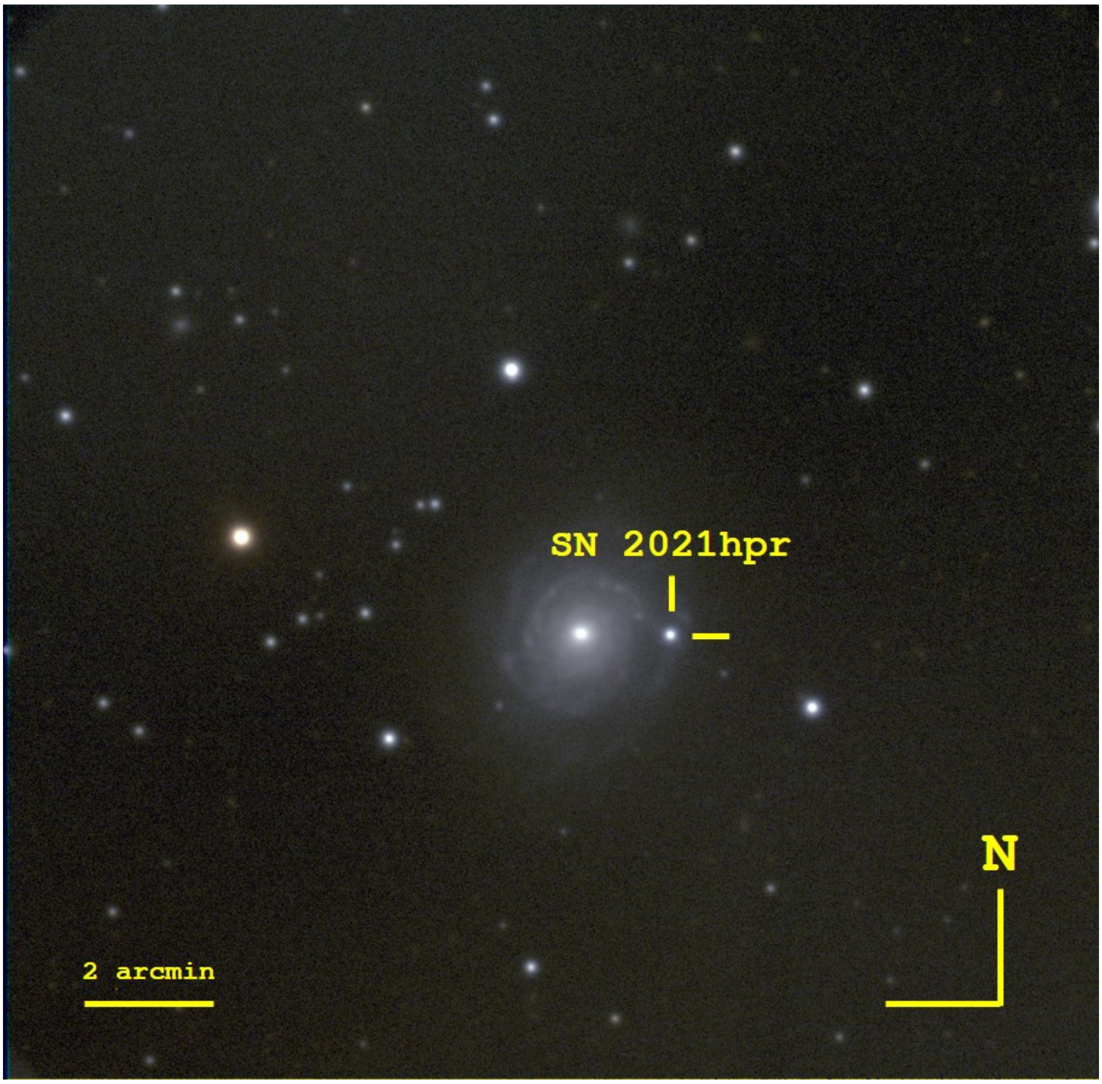

Figure 4.1. A color composite image of SN 2021hpr in NGC 3147. This image is composed of R-(red), V-(green), and B-(blue) band images observed on 2021-04-17 (almost at B-maximum) taken with the DOAO 1-m telescope. The yellow reticle points to the supernova. North is up, and East is to the left.

(taken at near maximum brightness), we classify that the SN 2021hpr spectrum is similar to SN 1989B, a normal SN Ia.

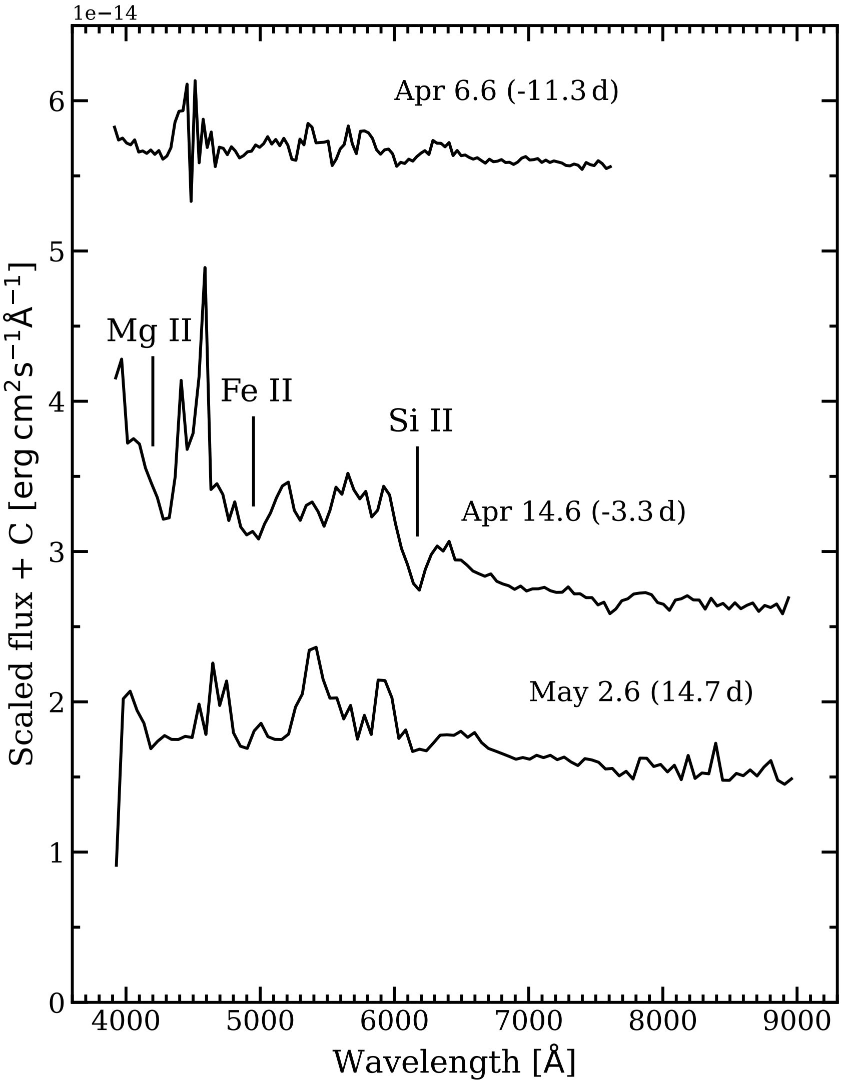

Figure 4.2. Optical spectra of SN 2021hpr, observed from the SAO 1-m telescope. Fluxes are shifted with additional constant values. No extinction is corrected.

4.3 Analysis

4.3.1 The optical long-term light curve and the nature of SN 2021hpr

Table 2 provides the optical light curve data before the dust extinction correction, and Figure 4 shows the optical light curve from -17.025 to 29.329 days from the B-maximum, corrected for the dust extinction. The galactic reddening is adopted as $E(B-V)_{\mathrm{MW}} = 0.021$ ($A_B = 0.088$, $A_V = 0.067$, $A_R = 0.053$, and $A_I = 0.037$; Schlafly & Finkbeiner 2011). The host galaxy reddening is determined from the peak $B-V$ color as described in Section 3.2, and we assumed the galactic extinction curve (Fitzpatrick 1999) and $R_V = 3.1$ to obtain the extinction correction in each band. The light curves of SN 2011fe, one of the most well-studied SNe Ia, are over-plotted for comparison, matching the B-band peak brightness epoch and giving arbitrary y-direction shifts to overlap with the maximum brightness of SN 2021hpr. For this, we adopt the SN 2011fe's peak time as 55814.48 MJD (Zhang et al. 2016). A polynomial fit (solid line) was performed on the SN 2021hpr light curve using the data near the peak from -7 to $+18$ days, which gives us the times and brightnesses ($t_{\lambda,\mathrm{max}}$, $m_{\lambda,\mathrm{max}}$) at the peak brightness and the decline rates, $\Delta m_{15}(\lambda)$, at different bands. These quantities are taken from the 50 percentile value in the distribution using the bootstrap re-sampling ($N = 1000$; Table 3). The uncertainty is adopted from the standard deviation in the distribution of each parameter.

The $\Delta m_{15}(\lambda)$ value, the spectral features, and the similarity of its light curve to SN 2011fe all suggest that SN 2021hpr is a normal SN Ia.

4.3.2 The reddening, peak absolute magnitude, and distance to NGC 3147

We measured the host reddening using the relation between the intrinsic $B-V$ color at the maximum brightness, $(B_{\mathrm{max}} - V_{\mathrm{max}})_0$, and $\Delta m_{15}(B)$ (Phillips et al. 1999). The observed $B-V$ color at the maximum brightness, $(B_{\mathrm{max}} - V_{\mathrm{max}})_{\mathrm{corr}}$, is -0.007 ± 0.006 after the galactic extinction correction alone. The intrinsic color in maximum

Table 3. Light curve parameters, estimated from the polynomial fit of the light curve of SN 2021hpr. Both the galactic and host extinctions are corrected.

	$t_{\lambda,\max}$ (MJD)	$m_{\lambda,\max}$ (*mag*)	$\Delta m_{15}(\lambda)$ (*mag*)
B	59321.893 ± 0.217	13.740 ± 0.004	0.984 ± 0.025
V	59324.003 ± 0.126	13.828 ± 0.004	0.697 ± 0.025
R	59323.428 ± 0.160	13.984 ± 0.008	0.698 ± 0.027
I	59320.731 ± 0.083	14.766 ± 0.003	0.486 ± 0.005

brightness, $(B_{\max} - V_{\max})_0$, is expected to be -0.083 ± 0.039 for $\Delta m_{15}(B) = 0.984 \pm 0.025$, therefore, we measure $E(B - V)_{\text{host}}$ as 0.076 ± 0.039.

The extinction coefficients in each band are estimated assuming the galactic extinction curve ($R_V = 3.1$; Fitzpatrick 1999). Note that this value is larger than that of 0.22 ± 0.05 mag for SN 2008fv (Biscardi et al. 2012), an SN Ia that appeared in another arm of NGC 3147.

$M_{B,\max}$ is -19.56 ± 0.11 AB mag according to the width ($\Delta m_{15}(B)$) - luminosity relation (Phillips et al. 1999), which is consistent with the recent measurement in Zhang et al. (2022). Here, we used the Phillips relation from the CfA3 sample (Hicken et al. 2009) in the AB system, since SN 2021hpr is close to a normal SN Ia from its spectrum. Combining the expected $M_{B,\max}$ and the measured peak luminosity in Table 2, we find that the distance modulus of NGC 3147 is 32.98 ± 0.11 mag or the distance (d) as 39.50 ± 2.02 Mpc. In Figure 3, we show previous distance estimates that are derived from historical SNe Ia (Amanullah et al. 2010; Prieto et al. 2006; Tully et al. 2013; Wang et al. 2006; Takanashi et al. 2008; Biscardi et al. 2012; Kowalski et al. 2008; Jha et al. 2007; Reindl et al. 2005; Parodi et al. 2000) and the Tully-Fisher (TF) relation range (Bottinelli et al. (1984, 1986); Tully & Fisher (1988); Distances from TF are measured

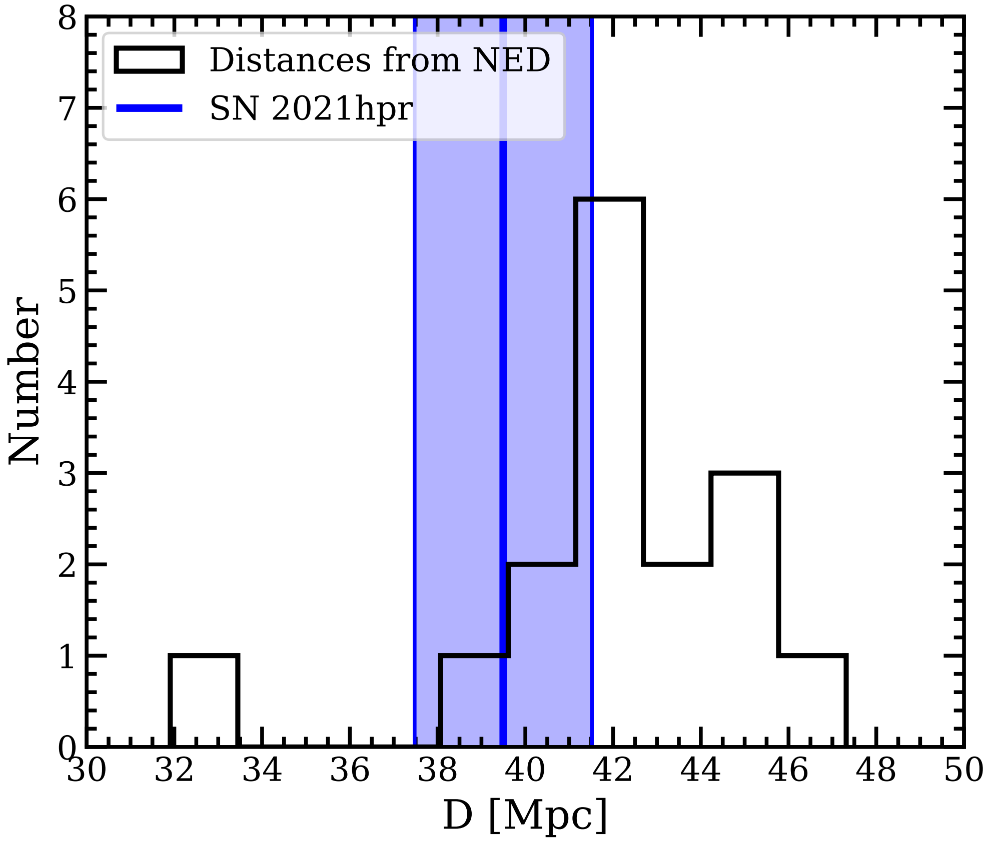

Figure 4.3. A histogram of estimated distances of NGC 3147 from the NED database. The distance estimated in this study is marked as the blue solid line shaded with a 1σ uncertainty.

before the 1990s). These values range from 30 to 50 Mpc with a median value of 40.7 Mpc (References taken from NASA/IPAC Extragalactic Database (NED)[¶]), and converted to appropriate values adopting a common Hubble constant. Our value is consistent with the median value of the distribution.

[¶] `https://ned.ipac.caltech.edu/`

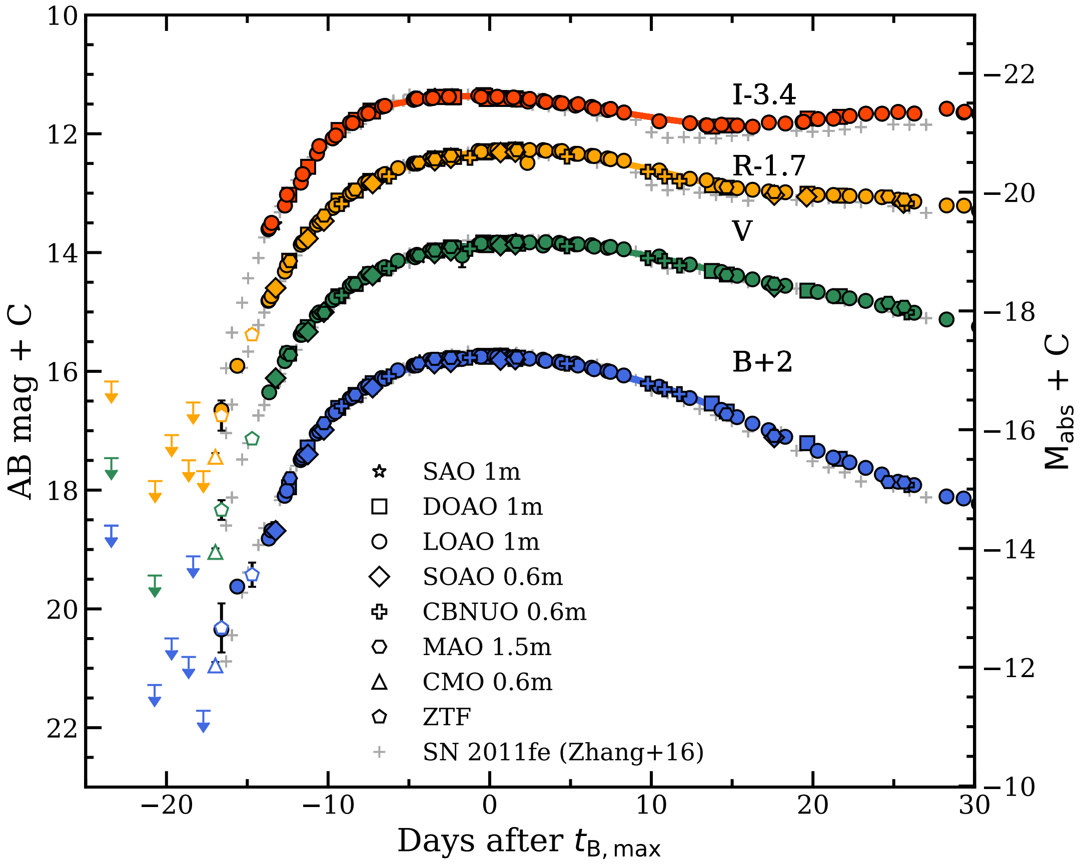

Figure 4.4. The optical light curve of SN 2021hpr. Other reported data points like CMO and ZTF are marked as open symbols. The polynomial fitting results are overplotted as solid line. SN 2011fe is also marked as gray cross symbols with an offset to the y-axis direction. The milky way and the host galaxy extinction are both corrected.

4.3.3 The early light curve

Figure 5 shows the early light curve of SN 2021hpr ±5 days from the first light time ($t_{\rm fl}$[‖]). Early flux evolution of SNe Ia can be described well with a rising power law (t^{α}) with $\alpha \sim 2$ (the fireball model), but whether there is a deviation from this behavior in the very early time (within one day or so from the explosion) has been in debate.

[‖] We adopted the term "the first light time" in the literature describing that the photons generated from radioactive decay of ^{56}Ni start to escape from the photosphere.

Figure 5 shows a bumpy feature in the very early time ($t_{\mathrm{fl}} < 0$) that seems to deviate from a simple power-law light curve ("Early excess"). Here, we examine this early excess in the light curve quantitatively using the power-law model and the ejecta-companion interaction model suggested by Kasen (2010). We model the rising part of the SN Ia light curve with a combination of a simple power-law and a SCHE. The simple power-law model is described in Equation (11).

$$M(t) = M_0 - 2.5\alpha \log_{10}(t - t_{\mathrm{fl}}). \tag{4.11}$$

Here, $M(t)$ is the absolute magnitude as a function of time t, and M_0 is a normalization factor of the absolute magnitude at a unit time of $t - t_{\mathrm{fl}} = 1$.

The SHCE light curve is calculated using the ejecta-companion interaction model of Kasen (2010, hereafter K10). To calculate the effective temperature, $T_{\mathrm{eff}}(t)$, and the luminosity, $L(t)$, of SHCE, we use the equations below which are taken from Im et al. (2015).

$$T_{\mathrm{eff}}(t) = 5.3 \times 10^3 \frac{R_{10}^{1/4}}{\kappa_{0.2}^{35/36}} t_{\mathrm{exp}}^{-37/72}\ \mathrm{K}, \tag{4.12}$$

$$L(t) = 2.0 \times 10^{40} \frac{R_{10} M_c^{1/4} v_9^{7/4}}{\kappa_{0.2}^{3/4}} t_{\mathrm{exp}}^{-0.5}\ \mathrm{erg\ s^{-1}}. \tag{4.13}$$

Here, R_{10} is the radius of the companion star in units of 10^{10} cm (R_*=(separation distance)/2 where R_* is the stellar radius), $\kappa_{0.2}$ is the opacity in units of 0.2 cm^2 g^{-1} which is adopted as 1.0, M_c is the ejecta mass in units of $1.4\,M_\odot$ which is adopted as 1/1.4, t_{exp} is the time since the explosion in units of days, and v_9 is the expansion velocity of the ejecta in units of 10^9 cm s^{-1} (adopted as 1.0, here).

The light curve fit was performed on the 4 band data simultaneously by minimizing chi-square using the `Python` library of `LMFIT` (Newville et al. 2014). Free parameters are α_{B}, α_{V}, α_{R}, α_{I}, $M_{0,\mathrm{B}}$, $M_{0,\mathrm{V}}$, $M_{0,\mathrm{R}}$, $M_{0,\mathrm{I}}$, t_{fl}, R_*, and t_{gap}, where the last two parameters are the radius of companion in the unit of $R_\odot$ and the time gap between t_{exp} and t_{fl} ($t_{\mathrm{gap}} = t_{\mathrm{fl}} - t_{\mathrm{exp}}$), where t_{exp} is the explosion time which marks the start of SHCE. Furthermore, the amount of SHCE in the companion model is dependent on the viewing angle. We assume the optimal viewing angle that the observer looks down to the ejecta-companion collision. If we consider a common viewing angle, the companion radius could be larger than that assumed at the optimal viewing angle by about a factor 10.

The best-fit parameters are given in Table 4. As seen in Figure 5, our two-component model can explain the early excess of SN 2021hpr with a $R_* = 5.95 \pm 0.35\,R_\odot$ sized companion, giving the goodness of fit of χ^2_ν as 2.3. The explosion time (t_exp) is estimated as 59304.76 ± 0.01 MJD. t_gap is also estimated as 1.65 ± 0.20 days. This can be regarded as a large value (e.g., Noebauer et al. (2017)), but it is acceptable if a large fraction of ^{56}Ni is deep from the ejecta surface in which case so t_gap can be up to a few days after the explosion (Piro & Nakar 2013). When assuming a common viewing angle which we modeled by multiplying Eq. (13) by 0.1, the radius of the companion star can be $R_* = 101.40 \pm 30.42\,R_\odot$ ($\chi^2_\nu = 3.9$). When we fix the power index to 2 (the fireball model), t_gap is 0.85 ± 0.12 days and $R_* = 4.50 \pm 0.65\,R_\odot$ with $\chi^2_\nu = 4.8$ (Optimal viewing angle). A pure power-law model gives a poor fit ($\chi^2_\nu = 5.3$, dash-dotted line), and it is disfavored.

Table 4. The best results of the early light curve fit by different methods. We did not include the case of the Companion+Simple power-law model (fireball) assuming the common viewing angle because we obtained unacceptable result that model lines cannot explain the upper limit in observed data.

Fitting method	Viewing angle	α	M_0 (mag)	$t_{\rm exp}$ (MJD)	$t_{\rm fl}$ (MJD)	$t_{\rm gap}$ ($days$)	R_* ($R_\odot$)	χ^2_ν
Simple power-law		(B) 3.78 ± 0.32	24.55 ± 1.00		59301.15 ±0.53			5.3
		(V) 3.55 ± 0.27	23.92 ± 0.87					
		(R) 3.45 ± 0.29	23.84 ± 0.90					
		(I) 3.38 ± 0.26	24.24 ± 0.81					
Companion+Simple power-law	Optimal	(B) 2.05 ± 0.14	18.54 ± 0.32	59304.76 ±0.01	59306.42 ±0.20	1.65 ±0.20	5.95 ±0.35	2.3
		(V) 1.52 ± 0.11	17.70 ± 0.24					
		(R) 1.56 ± 0.12	17.98 ± 0.25					
		(I) 1.88 ± 0.14	19.17 ± 0.30					
	Common	(B) 3.43 ± 0.28	22.55 ± 0.75	59304.31 ±0.12	59303.88 ±0.46	-0.43 ±0.45	101.40 ±30.42	3.9
		(V) 2.60 ± 0.18	20.71 ± 0.53					
		(R) 2.45 ± 0.20	20.63 ± 0.55					
		(I) 2.64 ± 0.20	21.59 ± 0.55					
Companion+Simple power-law (Fireball)	Optimal	2 (Fixed)	(B) 18.86 ± 0.06	59304.74 ±0.02	59305.59 ±0.12	0.85 ±0.12	4.50 ±0.65	4.8
			(V) 18.80 ± 0.05					
			(R) 19.01 ± 0.05					
			(I) 19.71 ± 0.04					

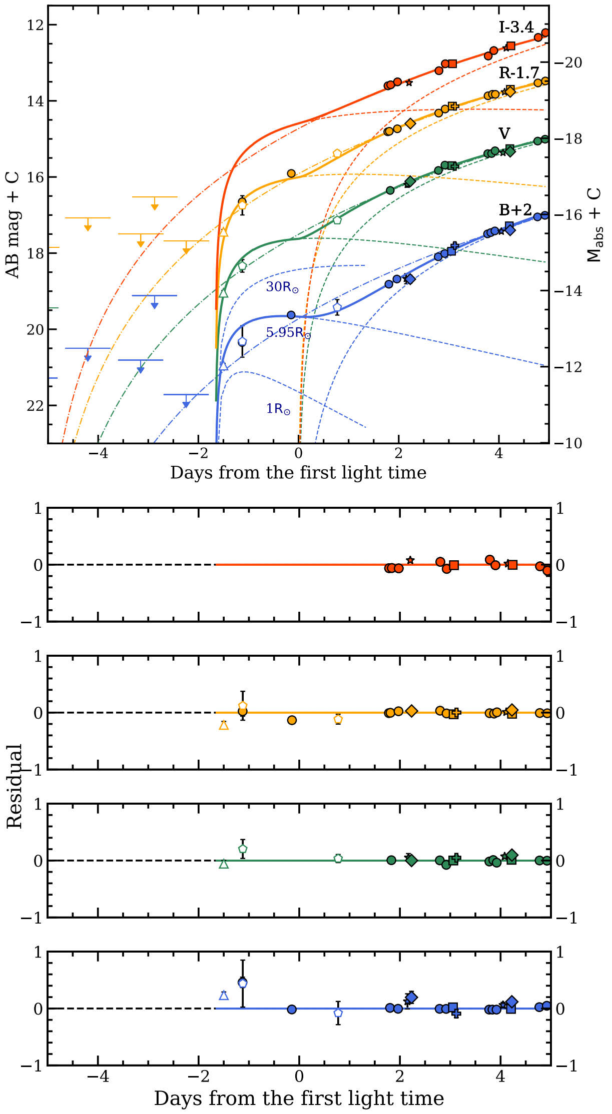

Figure 4.5. (top) The early light curve of SN 2021hpr between -5 and 5 days from the first light time with the best fit of the two-component model (Solid line). Dashed lines show separated model lines of K10 and the power-law fitting results. Pure simple power-law model lines are also overplotted in dash-dotted lines. Each symbol is the same as that in Figure 4. K10 models for $1\,R_{\odot}$ and $30\,R_{\odot}$-sized companion stars are overplotted (Black dashed line). (bottom) A residual plot corresponding to the top.

4.3.4 Early color evolution

Our multi-color, high cadence monitoring observation allows us to construct the color curve from the time shortly after the explosion. The 2nd and 3rd left panels of Figure 6 shows the color curve in $B - V$ and $B - R$, compared with several R_* values for the power-law + K10 model. SN 2021hpr was blue very early on, then reddened, and became blue again a few days after the first light time. This overall behavior is in qualitative agreement with our two-component model including SHCE. According to the two-component model, $T_{\rm eff}$ of SHCE increases with $R^{1/4}$, meaning that the larger the companion is, the bluer the early color curve is. Therefore, in this model, if the companion star is large ($R_* \sim 30\,R_\odot$), the predicted colors are very blue. On the other hand, the peak of the color curve in early epochs becomes too red if the companion star is too small. Figure 6 shows the early peak colors agree with a rather small companion star case ($R_* \sim 6\,R_\odot$).

Additionally, Figure 6 shows the light and color curves of the cases where the power-law model is replaced with the delayed detonation models (DDC; Blondin et al. 2013) and pulsational detonation models (PDD; Dessart et al. 2014) since the two models are in common in their properties of no ejecta interaction (Marion et al. 2016). SN ejecta properties (kinetic energy, nickel mass, abundances, mixing, etc.) varies in each model. They are summarized in Table 2 in Dessart et al. (2014). Blondin et al. (2013) mentioned that, at the maximum brightness, the synthetic spectrum of the DDC10 model matches very well with the observed spectrum of SN 2005cf, and even its UV flux though some spectral features are expected to be narrower and redder in the model. On the other hand, Dessart et al. (2014) mentioned that many parts of the spectrum and the light curve of SN 2011fe are reproduced with the PDDEL4n model around the maximum but there are discrepancies at early times.

In Figure 6, DDC10 is similar to our fitting results > 6 days after $t_{\rm fl}$ while it is not similar to the PDDEL4n model. In this figure, we can find that colors most likely agree with the companion model of the radius of $R_* = 5.95\,R_\odot$ sized star for the optimal viewing angle. We also present other possible results with different configurations in

Figure C.1 including the case of the Power-law+K10 fit at the common viewing angle. DDC10_M4 is slightly brighter in the I-band light curve than that of DDC10 in Figure 6. DDC15 also explains the I-band light curve but it shows a faster rise in the early part than that of DDC10 in Figure 6.

4.3.5 Finding Possible Progenitor System in the Pre-explosion HST image

We could possibly constrain the progenitor system by directly identifying the progenitor at the SN position in the pre-explosion images (Li et al. 2011; McCully et al. 2014). We identified a series of Hubble Space Telescope (HST) images from the HST archive[**] taken before the SN explosion during November 2017 to March 2018 (Proposal 15145; PI: A. Riess) and after the explosion (Proposal 16691, PI: R. Foley). The images were obtained by Wide-Field Camera 3 (WFC3) in F350LP, F555W, F814W, and F160W filters. Table 5 summarized the observation. Images were stacked using Swarp (Bertin 2010). Figure 7 shows the HST images before and after the SN explosion. The coordinate of SN2021hpr and its 1-σ error, $0\farcs3$ from Gaia alerts (Yaron 2019) in Transient Name Server[††] is drawn as circle in the figure.

At the SN 2021hpr position, no obvious source is found in the pre-explosion image. We measured a 5σ detection limit for a point source with the default aperture size of 0.2 arcsecond radius, finding upper limits on the progenitor system magnitudes of $\sim 27-28\,$mag in optical, and $\sim 25\,$mag in F160W (Table 5).

Figure 8 shows the color-magnitude diagram (CMD) with stellar evolutionary tracks and HST upper limits. The tracks are calculated from the MESA Isochrones and Stellar Tracks (MIST; Choi et al. 2016), a recent set of stellar evolutionary tracks and isochrones, which provides the synthetic photometry in HST/WFC3 filters[‡‡]. We adopted the tracks of initial mass ($M_{\rm init}$) from $8-16\,M_{\odot}$ with the step of $2\,M_{\odot}$ with solar metallicity assumption. We also plotted the Bessell V- and I-band synthetic pho-

---

[**] `https://archive.stsci.edu/`

[††] `https://sandbox.wis-tns.org/object/2021hpr#comment-wrapper-23355`

[‡‡] `http://waps.cfa.harvard.edu/MIST/index.html`

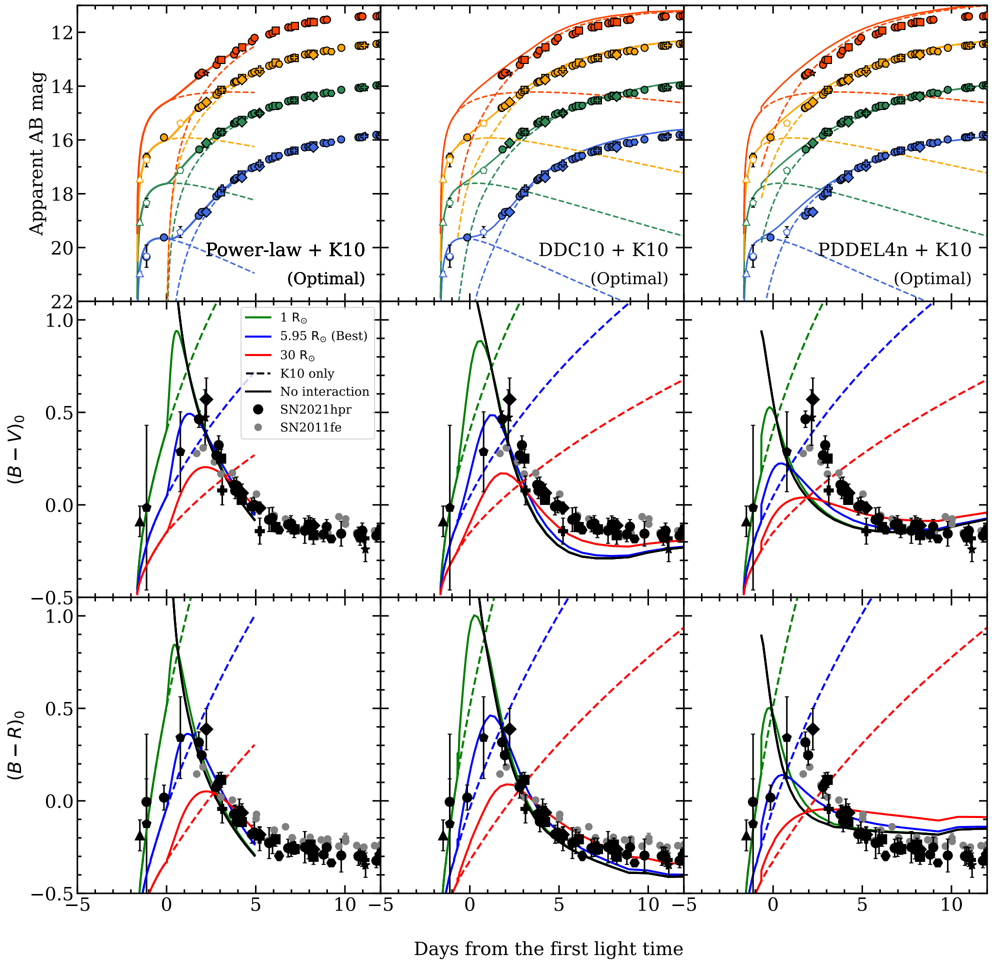

Figure 4.6. The reddening-corrected light curves (Top row), $(B-V)_0$ color (Middle row), and $(B-R)_0$ color (Bottom row) curves of SN 2021hpr and SN 2011fe (Black and grey filled circles) in the early phase with the different two-component models (The best fit of Companion+Simple power-law, DDC10 (Blondin et al. 2013), and PDDEL4n (Dessart et al. 2014) at the optimal viewing angle. Two-component models with different companion radii and only K10 models are also presented in solid and dashed lines.

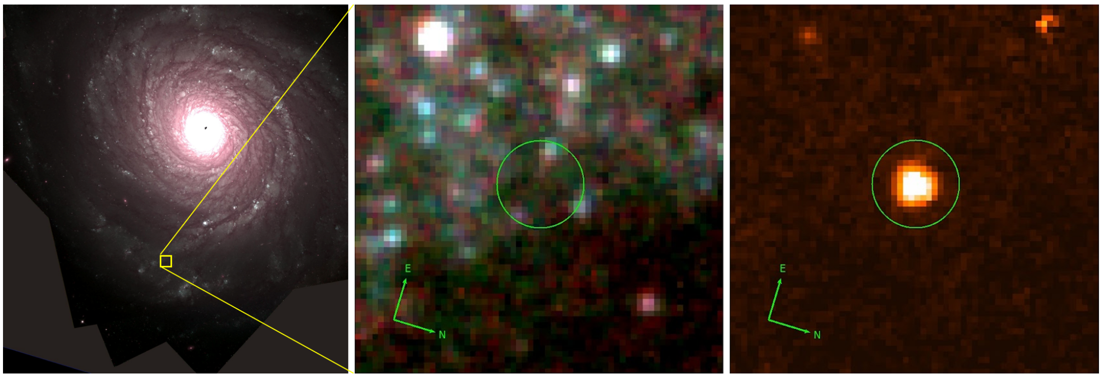

Figure 4.7. (Left) An F350LP/F555W/F814W color image before the explosion of SN 2021hpr observed by the Hubble Space Telescope/Wide Field Camera 3 (WFC3). (Middle) A zoomed region ($2.''5 \times 2.''5$) of the region in the yellow box of the full-frame image on the left. The site of SN 2021hpr is marked with a green circle centered at the *Gaia* alert coordinated with a radius of the 1σ astrometric accuracy ($0.''3$). (Right) The detection image of SN 2021hpr in the F814W filter on Dec 29th, 2021. FOV is the same with the middle panel. The source on the upper right is an artifact.

tometry[§§] of some evolved stars including asymptotic giant and supergiant branch in the Large Magellanic Cloud (LMC) (black filled circles; Groenewegen & Sloan 2018).

In the CMD, stars with $M_{\rm init} > 12\,M_\odot$, except for some in the high luminosity phase, would have been detected in the HST image. The radius of $M_{\rm init} \sim 12\,M_\odot$ star can be approximated with the evolutionary tracks in Levesque et al. (2005). Assuming $\log_{10}(\mathrm{T_{eff}}\,[\mathrm{K}]) = 3.56$, $M_{\rm bol} = -6.0\,\mathrm{mag}$ as the effective temperature and bolometric magnitude of stars with $M_{\rm init} = 12\,M_\odot$, we obtain $L/L_\odot \sim 19770$ giving us $R_* \sim 300\,R_\odot$ as an upper limit of the radius of the companion star.

[§§] They are calculated from the spectral energy distribution (SED) fit of samples in the literature. We plotted these because there is no large difference between V-, I-band, and F555W-, F814-band. The vega system is converted into the AB system.

Table 5. Description of HST WFC3/UVIS and IR imaging images. Host reddening ($A_{\lambda,\mathrm{host}}$) is calculated at the pivot wavelength. $M_{\mathrm{abs},0}$ is the Milky Way and host reddening corrected absolute magnitude.

	Pre-SN				Post-SN
Filter	F350LP	F555W	F814W	F160W	F814W
Detector	UVIS	UVIS	UVIS	IR	UVIS
t_{exp} [s]	25520	5952	5954	12055	780
N of images	11	5	5	5	1
Pivot λ [$\AA$]	5862.5	5308.2	8034.2	15369.2	8034.2
5σ limit [AB]	>27.54	>27.48	>26.89	>24.86	>26.00
$A_{\lambda,\mathrm{host}}$ [mag]	0.27	0.31	0.16	0.06	0.16
$M_{\mathrm{abs,obs}}$ [AB]	>-5.44	>-5.50	>-6.09	>-8.12	>-6.98
$M_{\mathrm{abs},0}$ [AB]	>-5.71	>-5.81	>-6.26	>-8.18	>-7.15

4.3.6 The stripped mass limit from HET late phase Spectroscopy

To identify emissions from the stripped matter of the companion, we also obtained an optical spectrum of SN 2021hpr using the blue pair of the second generation Low-Resolution Spectrograph (LRS2-B) mounted on the 9.2 m Hobby-Eberly Telescope at McDonald Observatory, USA (Chonis et al. 2014). LSR2-B is a $12'' \times 7''$ Integral Field Unit (IFU) that covers the wavelength ranges of $3700 \leq \lambda\,(\AA) \leq 4700$ (R$\sim$ 1900) and $4600 \leq \lambda\,(\AA) \leq 7000$ (R$\sim$ 1100). A single frame of 1000 seconds was obtained under a dark condition ($g \sim 21.13$ mag arcsec^{-}2) on 2021 November 30. At that time, SN 2021hpr was in a late phase (MJD 59548.51, +226 days from B-maximum brightness).

The spectrum was reduced using a standard pipeline, and flux calibration was conducted using a default response curve constructed with standard stars over 6 months in 2019. We used the redshift of $z = 0.009346$ from Tomasella et al. (2021) to shift the spectrum to the rest-frame. Milky Way and host galaxy extinction were also corrected. Furthermore, we re-calibrated the flux of the spectrum so that the flux values of the

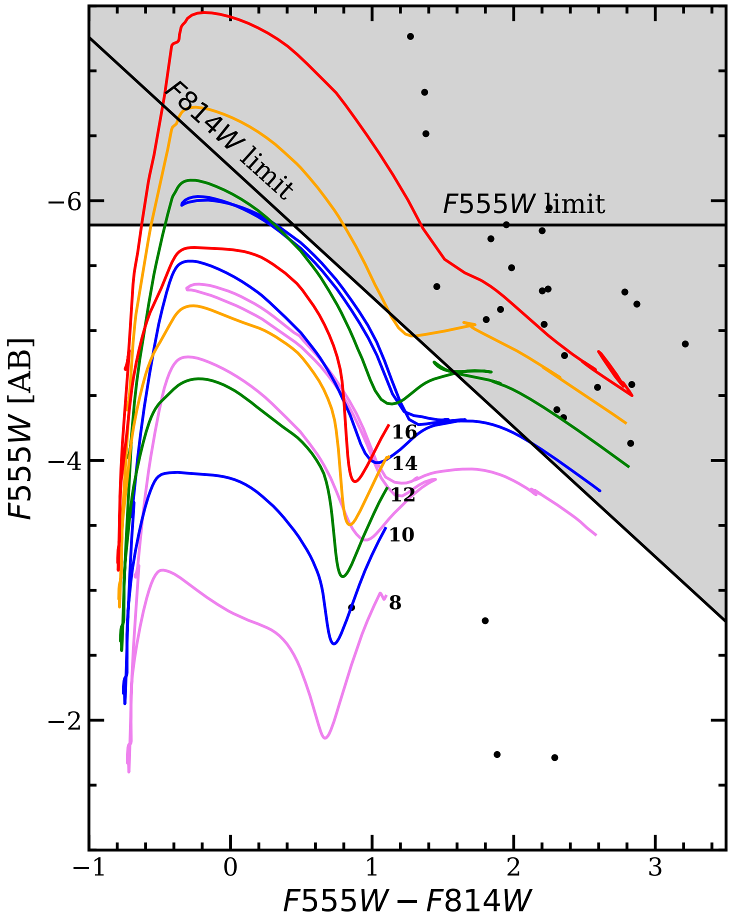

Figure 4.8. A color-magnitude diagram of HST filters with MIST evolutionary tracks for massive stars with the initial mass from $8 - 16\,M_{\odot}$ assuming the solar metallicity marked at the starting points of the tracks. The gray shading shows an excluded parametric space for the progenitor system. Extinction correction is applied in the upper limits here (black solid line). The bessell synthetic V- and I-band photometry of evolved stars in LMC are marked as black-filled circles.

spectrum match our photometry at the observed date by multiplying 1.61 on the flux as a correction factor.

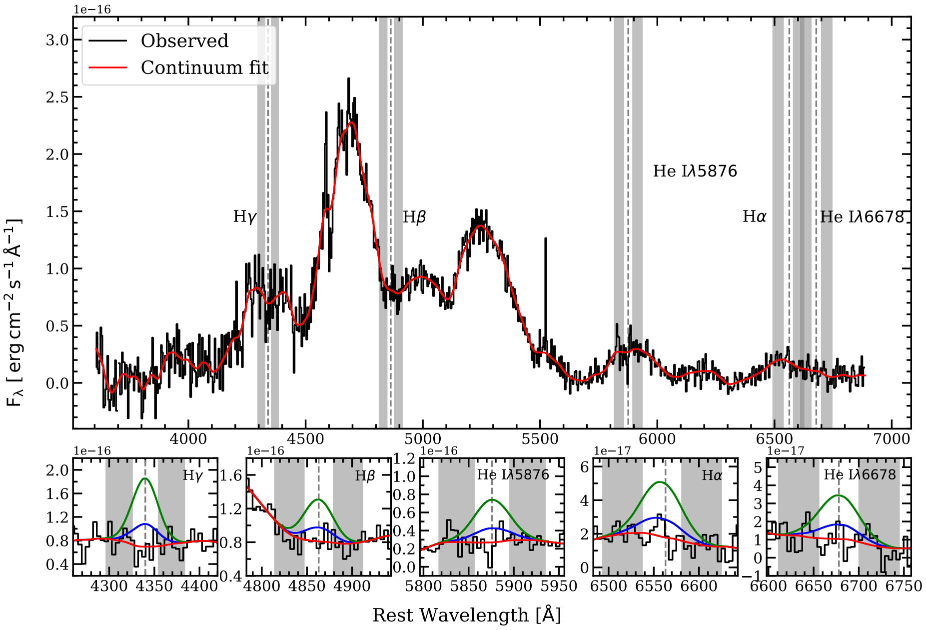

Figure 4.9. Flux-calibrated HET/LRS2-B spectrum (De-reddened) of SN 2021hpr at the nebular phase of +243 days since the explosion (black solid line) and the continuum fit (Red solid line). The gray dashed line marks the positions of each spectral line. Gray shaded areas are the masked regions for measuring the continuum RMS. Five subplots on the bottom show ambiance of spectral regions and 1σ- and 3σ-flux limits are plotted as blue and green solid lines. Flux is binned with a size of 6 Å.

Figure 9 shows the reduced spectrum. To search for nebular emission lines, we subtracted the continuum in the following way. We adopted the method from Tucker et al. (2019) for the continuum fit. We first masked regions around spectral lines such as the Balmer series lines (Hα, Hβ, Hγ), He I λ 5876, and He Iλ 6678) with the width of 1000 km/s ($W_{\rm line}$) that is known to be the line width of the stripped matter. Then, the spectrum was smoothed using the 2nd order Savitzky-Golay polynomial (Press et al. 1992) with a window size of 3000 km/s in 6563 $\AA$, which is wider (narrow) than the host galaxy (the ejecta) features. Considering $R = 1100$ at the He Iλ 6678, the observed data were binned to a wavelength size of 6 $\AA$. Observed data and the fitted continuum are shown as the black and red line in Figure 9.

Table 6. The continuum fluxes and flux and luminosity limits of nebular emission lines, along with the upper limits on the stripped mass corrected by multiplying the correction factors expected in +250 days since explosion.

Line	$W_{\rm line}$ (Å)	Continuum noise (σ) (10^{-17} erg Å^{-1} cm^{-2} s^{-1})	Flux limit (3σ) (10^{-16} erg Å^{-1} cm^{-2} s^{-1})	Luminosity limit (3σ) (10^{38} erg s^{-1})	$M_{\rm st}$ limit ($M_\odot$)
Hα	21.89	1.08	7.11	1.33	$< 0.0016 - 0.0020$
Hβ	16.22	1.66	8.09	1.55	$< 0.0018 - 0.0022$
Hγ	14.48	3.87	16.82	3.14	$< 0.0031 - 0.0039$
He Iλ 5876	19.60	1.57	9.23	1.72	$< 0.0019 - 0.0024$
He Iλ 6678	22.28	8.05	5.38	1.00	$< 0.0013 - 0.0016$

After subtracting the best-fit continuum from the observed spectrum, we searched for signs of emission lines in the spectral regions. As a result, we found no significant emission lines (Figure 9). We measured flux limits from the continuum RMS around each line. The RMS was measured as the standard deviation of the Gaussian fit of the continuum flux distribution ranging from $-3 \times W_{\rm line}$:-$W_{\rm line}$ to $W_{\rm line}$:$3 \times W_{\rm line}$, excluding the signals at the position of each emission line (The gray shaded regions in Figure 9). The $1-\sigma$ and $3-\sigma$ and flux limits are also plotted together in Figure 9 assuming a Gaussian profile with a width corresponding to 1000 km/s. These flux limits are converted to luminosity limits considering the distance. For the Hα emission line, the 3σ luminosity limit is 1.33×10^{38} erg/s. Using the Hα luminosity-stripped mass relation of the MS38 model (Equation 1) from Botyánszki et al. (2018), we estimate the 3σ stripped mass limit ($M_{\rm st}$) for each emission line[¶¶]. Since this model is predicted in 200 days since the explosion, we applied a scale factor to estimate $M_{\rm st}$ in +243 days since the explosion. Botyánszki et al. (2018) mentioned that there is a constant ratio of bolometric luminosity and Hα luminosity, but SN 2021hpr was observed in only BR bands between 200 and 250 days since the explosion. In this time range, B- and R-band flux have decreased a factor of 0.57 and 0.77 with little $B-R$ color change. After correction, the 3σ stripped mass limit ($M_{\rm st}$) for Hα is $< 0.0016 - 0.0020\, M_{\odot}$. For the other Balmer lines, the mass limits are also presented in Table 6. For He lines, their mass limits are obtained assuming that luminosity of He lines follows Equation (1).

For a He star companion, the hydrogen lines would not be visible. Yet, the stripped mass of $\lesssim 0.06\, M_{sun}$ is expected, and the predicted strengths of the He lines are only a factor of a few smaller than the hydrogen lines in H-rich companion star model (Botyánszki et al. 2018). No strong He emission lines in our data suggest a small amount of stripped He mass.

[¶¶] We adopted the form provided in Sand et al. (2018) as Equation (1) in Botyánszki et al. (2018).

4.4 Discussion

In section 3.3, we showed that the companion interaction model can explain the early blue excess in the SN 2021hpr light curve, suggesting the possibility of an SD system as the progenitor system with a $\sim 6\,R_{\odot}$ companion star of SN 2021hpr. A $\sim 6\,R_{\odot}$ companion can be a subgiant star with $6\,M_{\odot}$ or low mass red giant (Hachisu et al. 1996). On the other hand, the radius of $\sim 6\,R_{\odot}$ is too large for a low mass main-sequence star. A He-rich envelope star (He star) can also be a companion because its orbital separation a, assuming a circular orbit, ranges from $4 - 80\,R_{\odot}$ (Hachisu et al. 1999) with $a = 2 - 3\,R_{*}$ for typical mass ratios (Hachisu et al. 1996; Kasen 2010).

However, we detect no signatures of Hα emission in the late spectrum, while SNe Ia from SD progenitor systems are expected to show strong emission lines. Several works note that the stripped mass is reduced if the binary separation distance is large (Marietta et al. 2000; Pakmor et al. 2008; Liu et al. 2012; Pan et al. 2012; Boehner et al. 2017). Pakmor et al. (2008) demonstrates this in their equation (4). Pakmor et al. (2008) show $M_{\mathrm{st}} \sim a^{-3.5}$. Applying this relation to their models, it is not too difficult to obtain $M_{\mathrm{st}} < 0.01\,M_{\odot}$. For example their rp3_24a model, where the companion star's initial mass is $2.4\,M_{\odot}$ and the separation of the binary system is $4.39 \times 10^{11}\,\mathrm{cm}$ (or $6.3\,R_{\odot}$), they get $M_{\mathrm{st}} \sim 0.01\,M_{\odot}$. Making a a bit further will easily reduce M_{st} to a value less than $0.01\,M_{\odot}$.

Pakmor et al. (2008) also showed that low explosion energy produces a small amount of the stripped mass (The approximated relation is in equation (2) in Pakmor et al. 2008). Another reason for the non-detection of Hα could be the low explosion energy of SN 2021hpr. However, considering SN 2021hpr is a normal SN Ia event, low explosion energy would make SN 2021hpr a sub-luminous event.

As mentioned in the introduction, the early color of SN 2021hpr can be regarded as a “red bump” in the DDet model. Double detonation model is a model where the thermonuclear explosion in the He shell causes the core ignition. DDet models with thick He shell are known to produce excess in early light curve due to radioactive materials in the He shell ashes (e.g., Polin et al. 2019). On the other hand, the He shell ashes contain too much Fe-group elements that block the light and make the colors redder. Qualitatively speaking, one would expect red excess light in the early light curve in thick He shell DDet models, which is possibly in agreement with SN 2021hpr's color and light curves. Figure 10 compares the SN 2021hpr light and color curves with a thick He shell DDet model with $0.9\,M_{\odot}$ WD+$0.08\,M_{\odot}$ He shell (edge-lit) of Polin et al. (2019). The shape of the early red peak is similar to the observed colors but the model produces slower evolution of the red early light curve. Hence, the DDet model produces a light curve that is too red after the peak luminosity epoch. In this regard, as shown in Figure 11, it is instructive to examine color curves of various SNe Ia with an extensive set of early-time data. Figure 11 shows a diversity of early color curves of SNe Ia with early excess, except for SN 2011fe. The figure indicates there are roughly four families of color curves, one with a blue, flat color curve (SN 2017cbv and SN 2012cg), one with a red peak at 2-3 days, and then either becoming redder again (MUSSES1604D) or blue (SN 2021hpr, SN 2011fe), and one that shows a red peak at a very early epoch ($\sim$ 1 day) and becomes blue (SN 2018aoz). The favorite model for SNe Ia with the early red peak is the presence of Fe-peak elements in the outer ejecta extinguishing blue light. The outer ejecta are possibly produced by He-shell in DDet models. MUSSES1604D follows the DDet model trend well. For SN 2018aoz, the companion shock-heating model is disfavored since such a model cannot reproduce the color curve behavior. On the other hand, a DDet model can, and Jiang et al. (2017) also suggest another possibility of subsonic mixing for the presence of outer layer Fe-peak elements. For the flat, blue curves of SN 2017cbv and SN 2012cg, Hosseinzadeh et al. (2017) suggest a model with the circumstellar (CSM) material and nickel mixing, while they disfavor the companion interaction model because such a model cannot explain the excess in Swift UV bands.

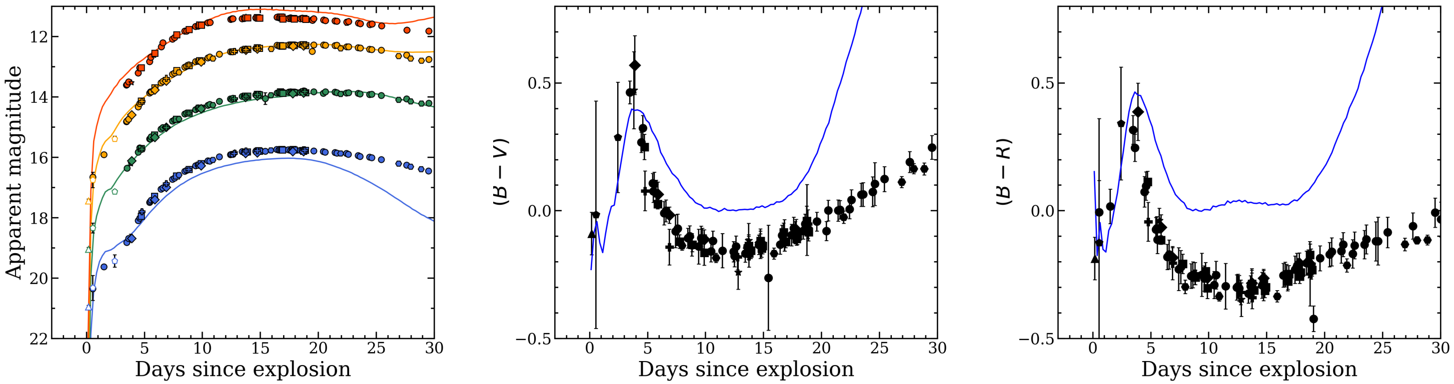

Figure 4.10. The light curve (Left), $B - V$ (Middle), and $B - R$ (Right) color evolution of SN 2021hpr with the He shell ($0.08\,M_{\odot}$) detonation on the $0.9\,M_{\odot}$ Sub-$M_{\rm ch}$ mass WD (Polin et al. 2019). The color and symbols are the same as in Figure 4. In the color curves, the model is presented as the blue solid line.

Levanon et al. (2015) derived an analytic form of an early signal emitted from the interaction between the SN ejecta and the accreted matter around the primary WD. This matter results from a tidal disruption of the companion WD (Disk-originated matter; DOM). This emission is also expected to last up to a few hours in the ultraviolet wavelength. The light curves of SN 2012cg and iPTF2014atg can be also examined by the ejecta-DOM interaction in addition to other suggested models such as stratified ^{56}Ni structure, DDet with an outer ^{56}Ni shell, and the companion interaction (Levanon & Soker 2017). In their further study, Levanon & Soker (2019) argued that the early blue excess of SN 2018oh is fitted with the two-component DOM interaction model better than the companion model. Another evidence against the companion model for SN 2018oh is the non-detection of Hα emission from the stripped matter of its donor star in the SD system (Tucker et al. 2019).

As shown earlier, SN 2021hpr's light and color curves can be explained well with a companion interaction model, making this SN distinct from SNe Ia like SN 2018aoz (very early red peak), SN 2017cbv (flat blue color curve), and MUSSES1604D (slow red peak, late red color). The early color curve behavior of SN 2021hpr resembles that of SNe 2011fe, therefore, the family of SNe Ia with this kind of color curves may have a similar explosion mechanism. A further improvements in DDet or DOM models may fully explain all observed features of SN 2021hpr.

4.5 Summary

We observed a type Ia supernova, SN 2021hpr firstly reported on 2021 April 2.45 UT, using a network of 0.4-1.0 meter class telescopes in the IMSNG program. A long-term light curve and a series of long-slit spectral analyses show that SN 2021hpr has typical characteristics of a normal type Ia supernova with a distance modulus of its host galaxy NGC 3147 as 32.98 ± 0.11 mag in the AB system (d=39.50 ± 2.02 Mpc).

In particular, the early photometric data shows a distinct feature of SHCE. We fit the early data using a two-component model of the ejecta-companion interaction and a simple power-law model. The model explains the early excess and blue color in the

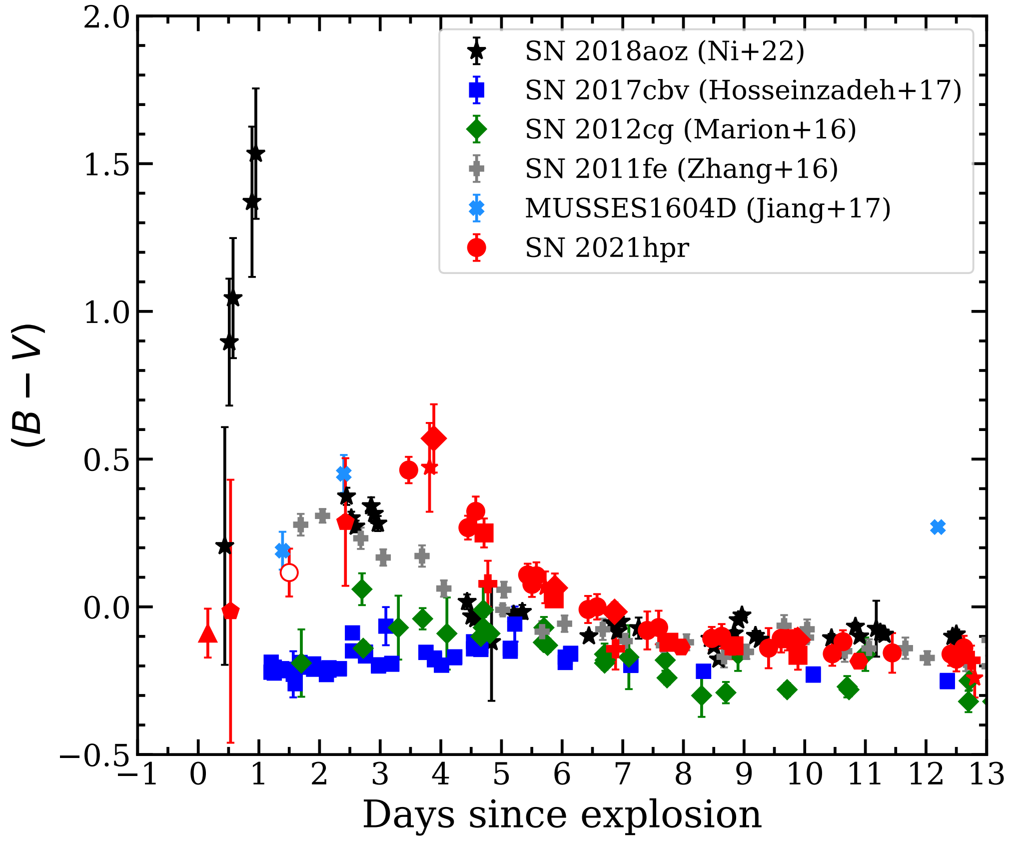

Figure 4.11. The de-reddened $B-V$ color evolution of SN 2021hpr with other type Ia supernovae within 13 days since explosion. A data point for SN 2021hpr is added at $t \sim 1.5$ days by converting $B-R$ to $B-V$ using a correlation between the two quantities during the first 4 days since explosion. SNe Ia except SN 2011fe are known to have early excess. Symbols of SN 2021hpr are same as Figure 4.

early phase well with an assumption of the optimal viewing angle. The best fit result is consistent with a companion radius of $5.95 \pm 0.35\,R_{\odot}$. The radius could be larger when the viewing angle varies. Subgiant, low mass red giant and helium star can be a possible donor but low mass main sequence star is not likely to be the progenitor companion under this scenario. We could not detect the probable progenitor candidate of SN 2021hpr at the TNS-reported position on the HST archival deep pre-explosion images above the detection limits. The detection limits on the color-magnitude diagram with the stellar evolutionary tracks using MIST only to rule out massive stars with $M_{\rm init} > 12\,M_{\odot}$, giving us the upper limit of the radius of the progenitor system up to $\sim 300\,R_{\odot}$.

Although the companion model examines the early evolution of SN 2021hpr, we could not find any strong signature of stripped mass ($\lesssim 0.002\,M_{\odot}$ for Hα emission) of H/He-rich material from the companion star in the late spectroscopy. This can result from a large binary separation rather than the low supernova explosion energy.

However, the non-detection of nebular emission lines in the late spectrum suggests that other kinds of progenitor system may be more plausible. In this regards, we examined color curves of SNe Ia with available very early color data (available at $< 1-2$ days). These color curves have a diversity of cases that can be summarized into four cases: (i) a color curve showing a very early red peak ($\lesssim$1 day after explosion) like SN 2018aoz; (ii) color curves with a slower appearance of red peak ($2-3$ days after explosion) with reddening of the curve in a later time (MUSSES1604D); (iii) or with the color staying blue after the red peak (SN 2011fe); and (iv) flat, blue color curve (SN 2017cbv). The first two cases support the He-shell detonation or at least ^{56}Ni in the outer ejecta, but a simple comparison of DDet models does not reproduce the early light and color curves of SN 2021hpr. Yet, DDet models and DOM models may explain the whole observed properties of SN 2021hpr in a more careful analysis in the future.

In conclusion, the evolution of SN 2021hpr (especially at the early phase) can be a good sample to test various progenitor scenarios so far. Furthermore, the detection of early excess of SN 2021hpr indicates that the high-cadence monitoring of nearby galaxies using small telescopes is still a powerful technique to constrain the progenitor system of SN Ia during the era of large telescopes.

Chapter 5

Conclusion

This thesis describes the results of early-time observations of Type Ia supernovae aimed to constrain their progenitor system using a small telescope network (SomangNet). We have operated a high-cadence monitoring program for nearby galaxies, IMSNG, with more than 10 telescopes to obtain early light curves of SNe. In this process, we established an automated observing system of KCT to increase our observing cadence in the southern sky. We could successfully obtain early light curves of two SNe Ia 2019ein and 2021hpr. Moreover, we performed the HET long-slit spectroscopy to find Hα emission in the late nebular phase of SN 2021hpr. We summarize our main results in detail below.

In Chapter 2, we introduce the overall characteristics and performance of the 0.36-m KCT system. KCT was installed on March 2020 at DeepSkyChile in Chile, showing a dark and stable night sky in the southern hemisphere. KCT focuses on the time-series observation mainly for transient with other SomangNet telescopes in multiple locations over the world. KCT uses a 0.36-m CDK optical tube and the German equatorial Paramount MX+ mount, and an SBIG STX16803 CCD camera with an SDSS filter set on the fixed pier. KCT shows the field of view of $49'.4 \times 49'.4$, pixel scale of $0''.724$ per pixel. Automated operation is established via script-based scheduling observation using a public software "ACP Observatory Control Panel". ACP selects the "adequate" target in a list uploaded by a user. From the analysis of our imaging data, we found uniform but slightly elongated PSFs over the field of view thought to be the optic system. Also, we found no shutter pattern even in very short exposures. A 5σ limiting of $g = 18.9$ AB mag for a point source with 10 minutes of integrated exposures in the clear sky. KCT is now obtaining daily monitoring data of IMSNG galaxies and a supermassive black hole binary (SMBHB) candidate, showing its potential for understanding the nature of transient events.

In Chapter 3, we present the constraint result of the progenitor system of SN 2019ein via its early light curve. The long-term light curve and long-slit spectroscopy show the characteristics of a slightly faint normal SN Ia ($M_{\rm B} = -19.14 \pm 0.03\,{\rm AB}$ mag, and $\Delta m_{15}(B) = 1.39 \pm 0.03\,{\rm mag}$) with little host galaxy reddening, providing the distance to NGC 5353 as $37.10 \pm 0.03\,{\rm Mpc}$. We found no early excess feature resulting from the shock-heated cooling emission. Two-component model fit of the companion model and a simple power-law gives us the radius of companion (i) $0.24 \pm 0.05\,R_{\odot}$ in R-band when forcing the first light time ($t_{\rm fl}$) to be one value (MJD 58603.19±0.09), (ii) $0.92 \pm 0.14\,R_{\odot}$ when using the average $t_{\rm fl}$ of MJD 58603.23 ± 0.57 in each band. All three cases can rule out a red giant star for the companion star.

In Chapter 4, we studied the progenitor system of SN 2021hpr with early detection. SN 2021hpr is a normal SN Ia from the photometric ($M_{\rm B} = -19.56 \pm 0.11\,{\rm AB}$ mag, $\Delta m_{15}(B) = 0.98 \pm 0.03\,{\rm mag}$) and spectroscopic data. A remarkable feature of SN 2021hpr is a significant "early excess" on the light curve with its bluish color. At this time, we fit the early part of $BVRI$-band light curves simultaneously with the two-component model, giving us the companion radius of $\sim 5.95 \pm 0.35\,R_{\odot}$ at the viewing angle looking down the collision (Optimal angle), while other fit result assuming the common viewing angle is also possible. We could not find possible progenitor system candidates in the HST pre-SN image, comparing the SN detected image. The limiting magnitudes exclude more massive single stars with an initial mass than ($M_{\rm init} > 12\,M_{\odot}$) corresponding to the radius of $\gtrsim 300\,R_{\odot}$. However, the late time spectrum gave no signs of the unbound mass from the companion star, which may be explained by the large separation distance rather than low SN explosion energy. In addition other detailed explanation with DDet and DOM models can possibly explain the early feature of SN 2021hpr.

We conclude this thesis work as follows based on the results above.

First, we could obtain the early light curve of SNe Ia via high-cadence observation of the network of small telescopes. To maximize the usage of each component in the network, reducing human intervention is essential. Automated operation of the KCT system now contributes to the recent increased number of SNe detection in IMSNG, expecting more early light curves of SNe. The number of transients detected in IMSNG increased recently after the participation of some telescopes (CBNUO, KCT, and RASA36), especially all four SNe Ia (SN 2021hpr, SN 2021pfs, SN 2021jag, and SN 2021aefx) observed in 2021 were detected in the early phase.

Second, some of the progenitor scenarios are ruled out by studying an early light curve of SNe Ia. We suggest the favored progenitor scenarios of SNe Ia based on our results. The progenitor systems of SNe Ia summarizes in (i)-(iv) in Figure 1.

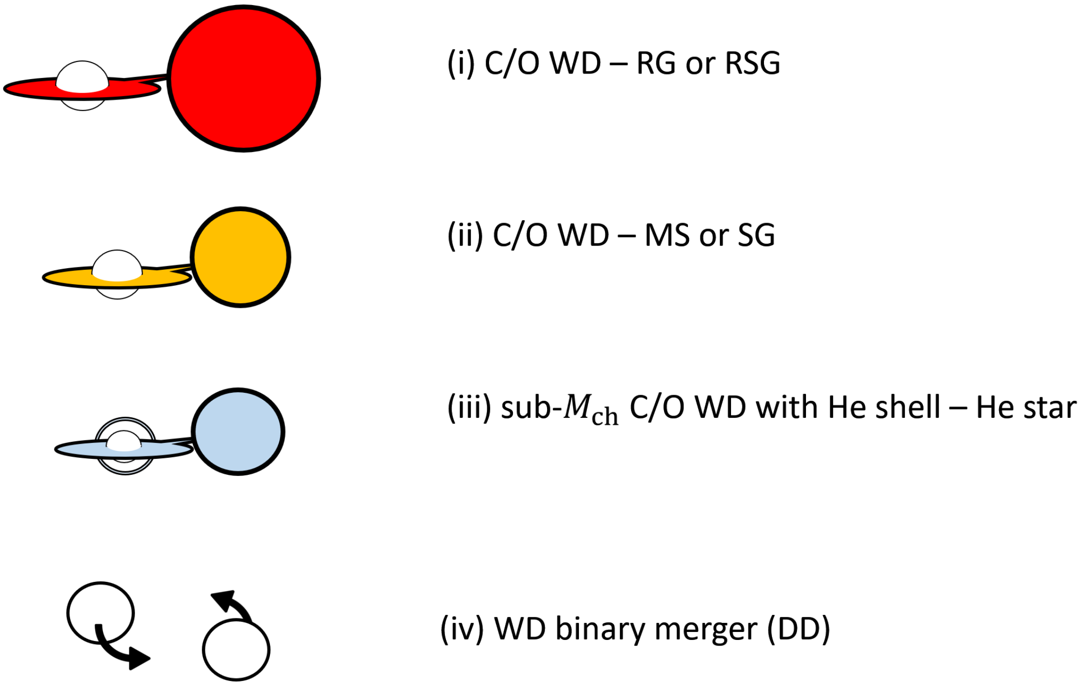

Figure 5.1. The summary of the possible progenitor systems of SNe Ia in this thesis work.

(i) A close binary system of $M_{\rm ch}$ C/O WD - red giant (RG) or red super-giant (RSG) are the most disfavored system in this thesis work. Many observational studies reject red giants and red super-giants as companion stars. The result of SN 2019ein (Chapter 3) also supports their results, disfavoring RGs as companions. It seems possible for a very limited case of this system, the WD - RG system with a large separation distance, according to this thesis work, considering the result of SN 2021hpr (Chapter 4).

(ii) For main sequence (MS) or sub-giant (SG) companions, the SN ejecta-companion interaction model produces relatively weak shock cooling features for this system, which agrees with early-time observations of SNe Ia with no excessive emission in the light curve. However, the SD system (i) and (ii) have to explain a few results of non-detection of the Hα emission of the unbound matter from the donor star in the late time spectroscopy, despite the amount of the unbound matter has the possibility to be over-predicted in the theory.

(iii) The sub-$M_{\rm ch}$ C/O WD - helium donors (Double Detonation scenario) is not very preferred because the light curves of two SNe Ia in this thesis work cannot be explained perfectly with this model. For now, only some of SNe Ia showing an early red excess or sub-luminous (e.g. MUSSES1604D, SN 2018aoz, and SN2018byg) are known to be examined with the WD with a helium shell.

(iv) Since the merger of C/O WD binary predicts no early excess emission (or undetectable), we favor this scenario together with (ii), based on early observation results, considering this model does not require Hα emission in the nebular phase. Besides, the early blue excess of SN Ia light curves can also be described in some cases of WD binaries with the accretion disk.

Third, the progenitor system of SNe Ia can be distinguished by deeper IMSNG observation than now. However, none of our SNe Ia samples could clearly distinguish whether the progenitor system is the SD or DD model. The limiting magnitude of IMSNG should reach a depth enough to detect the luminosity of the shock-heated cooling emission produced by a white dwarf progenitor or companion. For a $0.1\,R_{\odot}$ sized star, the luminosity peaks at $R \sim -12\,\mathrm{AB}$ mag. This is too faint to be detected in a distance $\sim 50\,\mathrm{Mpc}$ but it could be achieved with more galaxies within $30\,\mathrm{Mpc}$ down to $R \sim 20.4\,\mathrm{AB}$ mag though they have a slightly low star formation rate.

Finally, additional information such as color evolution, spectrum, and high-resolution deep imaging can provide more observational evidence to distinguish the progenitor system of SNe Ia, especially with the early excess. Recent theoretical studies suggested many models explain the origin of the early excess but there is no consensus. In the companion model, the effective temperature of the shocked ejecta increases with the companion radius ($T_{\mathrm{eff}} \sim R^{1/4}$), so the large companion generates bluer color in the early phase showing a red peak after a few days since the explosion (t_{exp}). A prompt X-ray emission arises before this cooling emission, though the detection is very challenging due to its short duration. As I mentioned earlier, Hα emission is also predicted in the nebula phase (t_{exp}), which is also distinguished from the CSM interaction predicting Hα emission also in the early phase. For nearby SNe Ia, large companions can be rejected by the investigation of the pre/post-SN direct imaging with high-resolution with given magnitude limits. Some sub-luminous SNe Ia can be explained by the helium double detonation model. The color change is similar but a thin helium shell can explain a very red peak (redder than $B - V \sim 1$), showing the low effective temperature. This is also supported by the spectral feature from the helium ash such as titanium (Ti II at around $4,150\,\mathring{A}$) for some SN Ia. For CSM Interaction, the mass of CSM can be constrained not only with the early excess but also with the synchrotron radio emission.

In the future, the cooperation of the rapid follow-up using our small telescopes and spectroscopy or the deep high-resolution imaging from new large telescopes will create more synergies in understanding the nature of the progenitor system of SNe and transients.

Bibliography

Chapter 1. Introduction

Abbott, B. P., Abbott, R., Abbott, T. D., et al. 2017, ApJ, 848, L12. doi:10.3847/2041-8213/aa91c9

Alsabti, A. W. & Murdin, P. 2017, Handbook of Supernovae, 3. doi:10.1007/978-3-319-21846-5_1

Arnett, W. D. 1969, Ap&SS, 5, 180. doi:10.1007/BF00650291

Aznar-Siguán, G., García-Berro, E., Lorén-Aguilar, P., et al. 2013, MNRAS, 434, 2539. doi:10.1093/mnras/stt1198

Bai, Y., Zou, H., Liu, J., et al. 2015, ApJS, 220, 6. doi:10.1088/0067-0049/220/1/6

Branch, D. & Wheeler, J. C. 2017, Supernova Explosions: Astronomy and Astrophysics Library, ISBN 978-3-662-55052-6. Springer-Verlag GmbH Germany, 2017. doi:10.1007/978-3-662-55054-0

Boehner, P., Plewa, T., & Langer, N. 2017, MNRAS, 465, 2060. doi:10.1093/mnras/stw2737

Boisseau, J. R. & Wheeler, J. C. 1991, AJ, 101, 1281. doi:10.1086/115763

Botticella, M. T., Smartt, S. J., Kennicutt, R. C., et al. 2012, A&A, 537, A132. doi:10.1051/0004-6361/201117343

Botyánszki, J., Kasen, D., & Plewa, T. 2018, ApJ, 852, L6. doi:10.3847/2041-8213/aaa07b

Choi, C. & Im, M. 2017, Journal of Korean Astronomical Society, 50, 71. doi:10.5303/JKAS.2017.50.3.71

Choi, S., Im, M., & Choi, C. 2018, , 46, 141

Chugai, N. N. 1986, Soviet Ast., 30, 563

Elias-Rosa, N., Chen, P., Benetti, S., et al. 2021, A&A, 652, A115. doi:10.1051/0004-6361/202141218

Foley, R. J., Fox, O. D., McCully, C., et al. 2014, MNRAS, 443, 2887. doi:10.1093/mnras/stu1378

Fink, M., Hillebrandt, W., & Röpke, F. K. 2007, A&A, 476, 1133. doi:10.1051/0004-6361:20078438

Fink, M., Röpke, F. K., Hillebrandt, W., et al. 2010, A&A, 514, A53. doi:10.1051/0004-6361/200913892

Gao, Y. & Pritchet, C. 2013, AJ, 145, 83. doi:10.1088/0004-6256/145/3/83

Gil de Paz, A., Boissier, S., Madore, B. F., et al. 2007, ApJS, 173, 185. doi:10.1086/516636

Hachisu, I., Kato, M., & Nomoto, K. 1996, ApJ, 470, L97. doi:10.1086/310303

Hachisu, I., Kato, M., Nomoto, K., et al. 1999, ApJ, 519, 314. doi:10.1086/307370

Hachisu, I., Kato, M., & Nomoto, K. 2012, ApJ, 756, L4. doi:10.1088/2041-8205/756/1/L4

Han, Z. & Podsiadlowski, P. 2004, MNRAS, 350, 1301. doi:10.1111/j.1365-2966.2004.07713.x

Hoyle, F. & Fowler, W. A. 1960, ApJ, 132, 565. doi:10.1086/146963

Hwang, S., Im, M., Taak, Y. C., et al. 2021, ApJ, 908, 113. doi:10.3847/1538-4357/abcd9a

Iben, I. & Tutukov, A. V. 1984, ApJS, 54, 335. doi:10.1086/190932

Im, M., Ko, J., Cho, Y., et al. 2010, Journal of Korean Astronomical Society, 43, 75. doi:10.5303/JKAS.2010.43.3.075

Im, M., Choi, C., & Kim, K. 2015, Journal of Korean Astronomical Society, 48, 207. doi:10.5303/JKAS.2015.48.4.207

Im, M., Choi, C., Yoon, S.-C., et al. 2015, ApJS, 221, 22. doi:10.1088/0067-0049/221/1/22

Im, M., Yoon, Y., Lee, S.-K. J., et al. 2017, ApJ, 849, L16. doi:10.3847/2041-8213/aa9367

Im, M., Choi, C., Hwang, S., et al. 2019, Journal of Korean Astronomical Society, 52, 11. doi:10.5303/JKAS.2019.52.1.11

Im, M., Kim, Y., Lee, C.-U., et al. 2021, Journal of Korean Astronomical Society, 54, 89

Jha, S. W., Maguire, K., & Sullivan, M. 2019, Nature Astronomy, 3, 706. doi:10.1038/s41550-019-0858-0

Kasen, D. 2010, ApJ, 708, 1025. doi:10.1088/0004-637X/708/2/1025

Kelly, P. L., Fox, O. D., Filippenko, A. V., et al. 2014, ApJ, 790, 3. doi:10.1088/0004-637X/790/1/3

Khokhlov, A. M. 1991, A&A, 245, 114

Kim, J., Im, M., Choi, C., et al. 2019, ApJ, 884, 103. doi:10.3847/1538-4357/ab40cd

Kollmeier, J. A., Chen, P., Dong, S., et al. 2019, MNRAS, 486, 3041. doi:10.1093/mnras/stz953

Kushnir, D., Katz, B., Dong, S., et al. 2013, ApJ, 778, L37. doi:10.1088/2041-8205/778/2/L37

Li, W., Bloom, J. S., Podsiadlowski, P., et al. 2011, Nature, 480, 348. doi:10.1038/nature10646

Liu, Z. W., Pakmor, R., Röpke, F. K., et al. 2012, A&A, 548, A2.doi:10.1051/0004-6361/201219357

Liu, Z.-W., Pakmor, R., Seitenzahl, I. R., et al. 2013, ApJ, 774, 37. doi:10.1088/0004-637X/774/1/37

Maeda, K. & Terada, Y. 2016, International Journal of Modern Physics D, 25, 1630024. doi:10.1142/S021827181630024X

Maoz, D., Mannucci, F., & Nelemans, G. 2014, ARA&A, 52, 107. doi:10.1146/annurev-astro-082812-141031

Marietta, E., Burrows, A., & Fryxell, B. 2000, ApJS, 128, 615. doi:10.1086/313392

McCully, C., Jha, S. W., Foley, R. J., et al. 2014, Nature, 512, 54. doi:10.1038/nature13615

McCully, C., Jha, S. W., Scalzo, R. A., et al. 2022, ApJ, 925, 138. doi:10.3847/1538-4357/ac3bbd

Maguire, K., Taubenberger, S., Sullivan, M., et al. 2016, MNRAS, 457, 3254. doi:10.1093/mnras/stv2991

Minkowski, R. 1941, PASP, 53, 224. doi:10.1086/125315

Nomoto, K., Sugimoto, D., & Neo, S. 1976, Ap&SS, 39, L37. doi:10.1007/BF00648354

Nomoto, K. 1982, ApJ, 253, 798. doi:10.1086/159682

Nugent, P. E., Sullivan, M., Cenko, S. B., et al. 2011, Nature, 480, 344. doi:10.1038/nature10644

Pakmor, R., Röpke, F. K., Weiss, A., et al. 2008, A&A, 489, 943. doi:10.1051/0004-6361:200810456

Pakmor, R., Kromer, M., Röpke, F. K., et al. 2010, Nature, 463, 61. doi:10.1038/nature08642

Pakmor, R., Hachinger, S., Röpke, F. K., et al. 2011, A&A, 528, A117. doi:10.1051/0004-6361/201015653

Pakmor, R., Kromer, M., Taubenberger, S., et al. 2012, ApJ, 747, L10. doi:10.1088/2041-8205/747/1/L10

Pakmor, R., Kromer, M., Taubenberger, S., et al. 2013, ApJ, 770, L8. doi:10.1088/2041-8205/770/1/L8

Phillips, M. M. 1993, ApJ, 413, L105. doi:10.1086/186970

Phillips, M. M., Lira, P., Suntzeff, N. B., et al. 1999, AJ, 118, 1766. doi:10.1086/301032

Piro, A. L., Chang, P., & Weinberg, N. N. 2010, ApJ, 708, 598. doi:10.1088/0004-637X/708/1/598

Polin, A., Nugent, P., & Kasen, D. 2019, ApJ, 873, 84. doi:10.3847/1538-4357/aafb6a

Prieto, J. L., Chen, P., Dong, S., et al. 2020, ApJ, 889, 100. doi:10.3847/1538-4357/ab6323

Pruzhinskaya, M. V. & Lisakov, S. M. 2016, Journal of Astronomical History and Heritage, 19, 203

Rabinak, I. & Waxman, E. 2011, ApJ, 728, 63. doi:10.1088/0004-637X/728/1/63

Saio, H. & Nomoto, K. 1985, A&A, 150, L21

Srivastav, S., Ninan, J. P., Kumar, B., et al. 2016, MNRAS, 457, 1000. doi:10.1093/mnras/stw039

Troja, E., Piro, L., van Eerten, H., et al. 2017, Nature, 551, 71. doi:10.1038/nature24290

Trundle, C., Pastorello, A., Benetti, S., et al. 2009, A&A, 504, 945. doi:10.1051/0004-6361/200911776

Tucker, M. A., Shappee, B. J., Vallely, P. J., et al. 2020, MNRAS, 493, 1044. doi:10.1093/mnras/stz3390

Webbink, R. F. 1984, ApJ, 277, 355. doi:10.1086/161701

Wheeler, J. C., Lecar, M., & McKee, C. F. 1975, ApJ, 200, 145. doi:10.1086/153771

Whelan, J. & Iben, I. 1973, ApJ, 186, 1007. doi:10.1086/152565

Woosley, S. E., Taam, R. E., & Weaver, T. A. 1986, ApJ, 301, 601. doi:10.1086/163926

Woosley, S. E. & Weaver, T. A. 1994, ApJ, 423, 371. doi:10.1086/173813

Yoon, S.-C. & Langer, N. 2005, A&A, 435, 967. doi:10.1051/0004-6361:20042542

Yoon, S.-C., Podsiadlowski, P., & Rosswog, S. 2007, MNRAS, 380, 933. doi:10.1111/j.1365-2966.2007.12161.x

Chapter 2. KIAS Chamnun Telescope

Abbott, B. P., Abbott, R., Abbott, T. D., et al. 2017, ApJ, 848, L12. doi:10.3847/2041-8213/aa91c9

Bertin, E. 2011, Astronomical Data Analysis Software and Systems XX, 442, 435

Choi, C. & Im, M. 2017, Journal of Korean Astronomical Society, 50, 71. doi:10.5303/JKAS.2017.50.3.71

Denny, R. B. 2004, Society for Astronomical Sciences Annual Symposium, 23, 35

Henden, A. A., Templeton, M., Terrell, D., et al. 2016, VizieR Online Data Catalog, II/336

Im, M., Choi, C., & Kim, K. 2015, Journal of Korean Astronomical Society, 48, 207. doi:10.5303/JKAS.2015.48.4.207

Im, M., Choi, C., Yoon, S.-C., et al. 2015, ApJS, 221, 22. doi:10.1088/0067-0049/221/1/22

Im, M., Choi, C., Hwang, S., et al. 2019, Journal of Korean Astronomical Society, 52, 11. doi:10.5303/JKAS.2019.52.1.11

Im, M., Kim, Y., Lee, C.-U., et al. 2021, Journal of Korean Astronomical Society, 54, 89

Jiang, N., Yang, H., Wang, T., et al. 2022, arXiv:2201.11633

Kasen, D. 2010, ApJ, 708, 1025. doi:10.1088/0004-637X/708/2/1025

Kim, J., Im, M., Choi, C., et al. 2019, ApJ, 884, 103. doi:10.3847/1538-4357/ab40cd

Kwon, Y. G., Ishiguro, M., Kwon, J., et al. 2019, A&A, 629, A121. doi:10.1051/0004-6361/201935542

Onken, C. A., Wolf, C., Bessell, M. S., et al. 2019, PASA, 36, e033. doi:10.1017/pasa.2019.27

Chapter 3. The progenitor system of SN 2019ein

Arnett, W. D. 1982, ApJ, 253, 785. doi:10.1086/159681

Astropy Collaboration, Robitaille, T. P., Tollerud, E. J., et al. 2013, A&A, 558, A33

Barbary, K., Barclay, T., Biswas, R., et al. 2016, Astrophysics Source Code Library

Bertin, E., & Arnouts, S. 1996, A&AS, 117, 393

Becker, A. 2015, Astrophysics Source Code Library

Bellm, E. C., Kulkarni, S. R., Graham, M. J., et al. 2019, PASP, 131, 018002

Blanton, M. R. & Roweis, S. 2007, AJ, 133, 734. doi:10.1086/510127

Bloom, J. S., Kasen, D., Shen, K. J., et al. 2012, ApJ, 744, L17. doi:10.1088/2041-8205/744/2/L17

Bulla, M., Miller, A. A., Yao, Y., et al. 2020, arXiv:2001.00587

Cao, Y., Kulkarni, S. R., Howell, D. A., et al. 2015, Nature, 521, 328. doi:10.1038/nature14440

Cho, H., Woo, J.-H., Hodges-Kluck, E., et al. 2020, ApJ, 892, 93

Dessart, L., Blondin, S., Hillier, D. J., et al. 2014, MNRAS, 441, 532. doi:10.1093/mnras/stu598

Fink, M., Hillebrandt, W., & Röpke, F. K. 2007, A&A, 476, 1133. doi:10.1051/0004-6361:20078438

Fink, M., Röpke, F. K., Hillebrandt, W., et al. 2010, A&A, 514, A53. doi:10.1051/0004-6361/200913892

Hachisu, I. & Kato, M. 2003, ApJ, 588, 1003. doi:10.1086/374303

Han, Z. & Podsiadlowski, P. 2004, MNRAS, 350, 1301. doi:10.1111/j.1365-2966.2004.07713.x

Harutyunyan, A. H., Pfahler, P., Pastorello, A., et al. 2008, A&A, 488, 383. doi:10.1051/0004-6361:20078859

Hicken, M., Challis, P., Jha, S., et al. 2009, ApJ, 700, 331. doi:10.1088/0004-637X/700/1/331

Henden, A. A., Levine, S. E., Terrell, D., et al. 2012, Journal of the American Association of Variable Star Observers (JAAVSO), 40, 430

Hwang, S., Im, M., Taak, Y. C., et al. 2020, arXiv:2011.14049

Iben, I. & Tutukov, A. V. 1984, ApJS, 54, 335

Im, M., Ko, J., Cho, Y., et al. 2010, Journal of Korean Astronomical Society, 43, 75. doi:10.5303/JKAS.2010.43.3.075

Im, M., Choi, C., Yoon, S.-C., et al. 2015, ApJS, 221, 22

Im, M., Choi, C., Hwang, S., et al. 2019, Journal of Korean Astronomical Society, 52, 11

Kasen, D. 2010, ApJ, 708, 1025

Kawabata, M., Maeda, K., Yamanaka, M., et al. 2020, ApJ, 893, 143

Kochanek, C. S., Shappee, B. J., Stanek, K. Z., et al. 2017, PASP, 129, 104502

Lang, D., Hogg, D. W., Mierle, K., et al. 2010, AJ, 139, 1782

Magee, M. R. & Maguire, K. 2020, A&A, 642, A189. doi:10.1051/0004-6361/202037870

Marion, G. H., Brown, P. J., Vinkó, J., et al. 2016, ApJ, 820, 92. doi:10.3847/0004-637X/820/2/92

Munari, U., Henden, A., Belligoli, R., et al. 2013, , 20, 30

Nomoto, K. 1982, ApJ, 253, 798. doi:10.1086/159682

Nugent, P., Phillips, M., Baron, E., et al. 1995, ApJ, 455, L147. doi:10.1086/309846

Nugent, P. E., Sullivan, M., Cenko, S. B., et al. 2011, Nature, 480, 344

Pakmor, R., Röpke, F. K., Weiss, A., et al. 2008, A&A, 489, 943. doi:10.1051/0004-6361:200810456

Pakmor, R., Kromer, M., Röpke, F. K., et al. 2010, Nature, 463, 61. doi:10.1038/nature08642

Pakmor, R., Kromer, M., Taubenberger, S., et al. 2012, ApJ, 747, L10. doi:10.1088/2041-8205/747/1/L10

Pellegrino, C., Howell, D. A., Sarbadhicary, S. K., et al. 2020, ApJ, 897, 159

Perlmutter, S. A., Deustua, S., Gabi, S., et al. 1997, Thermonuclear Supernovae, 486, 749. doi:10.1007/978-94-011-5710-0_46

Perlmutter, S., Aldering, G., Goldhaber, G., et al. 1999, ApJ, 517, 565. doi:10.1086/307221

Phillips, M. M. 1993, ApJ, 413, L105. doi:10.1086/186970

Phillips, M. M., Lira, P., Suntzeff, N. B., et al. 1999, AJ, 118, 1766. doi:10.1086/301032

Piro, A. L., Chang, P., & Weinberg, N. N. 2010, ApJ, 708, 598. doi:10.1088/0004-637X/708/1/598

Piro, A. L. & Morozova, V. S. 2016, ApJ, 826, 96. doi:10.3847/0004-637X/826/1/96

Polin, A., Nugent, P., & Kasen, D. 2019, ApJ, 873, 84

Rabinak, I. & Waxman, E. 2011, ApJ, 728, 63

Riess, A. G., Filippenko, A. V., Challis, P., et al. 1998, AJ, 116, 1009

Science Software Branch at STScI 2012, Astrophysics Source Code Library

Skrutskie, M. F., Cutri, R. M., Stiening, R., et al. 2006, AJ, 131, 1163. doi:10.1086/498708

Tanikawa, A., Nakasato, N., Sato, Y., et al. 2015, ApJ, 807, 40. doi:10.1088/0004-637X/807/1/40

Tonry, J. L., Stubbs, C. W., Lykke, K. R., et al. 2012, ApJ, 750, 99. doi:10.1088/0004-637X/750/2/99

Tonry, J. L., Denneau, L., Heinze, A. N., et al. 2018, PASP, 130, 064505

Tonry, J., Denneau, L., Heinze, A., et al. 2019, Transient Name Server Discovery Report, 2019-678

Vinkó, J., Sárneczky, K., Takáts, K., et al. 2012, A&A, 546, A12

Webbink, R. F. 1984, ApJ, 277, 355. doi:10.1086/161701

Whelan, J. & Iben, I. 1973, ApJ, 186, 1007

Woosley, S. E., Taam, R. E., & Weaver, T. A. 1986, ApJ, 301, 601. doi:10.1086/163926

Yamanaka, M., Maeda, K., Kawabata, M., et al. 2014, ApJ, 782, L35

Yoon, S.-C., Podsiadlowski, P., & Rosswog, S. 2007, MNRAS, 380, 933

Zhang, K., Wang, X., Zhang, J., et al. 2016, ApJ, 820, 67. doi:10.3847/0004-637X/820/1/67

Zheng, W., Silverman, J. M., Filippenko, A. V., et al. 2013, ApJ, 778, L15

Chapter 4. The progenitor system of SN 2021hpr

Amanullah, R., Lidman, C., Rubin, D., et al. 2010, ApJ, 716, 712. doi:10.1088/0004-637X/716/1/712

Ashall, C., Lu, J., Shappee, B. J., et al. 2022, arXiv:2205.00606

Astropy Collaboration, Robitaille, T. P., Tollerud, E. J., et al. 2013, A&A, 558, A33

Becker, A. 2015, Astrophysics Source Code Library

Bertin, E., & Arnouts, S. 1996, A&AS, 117, 393

Bertin, E. 2010, Astrophysics Source Code Library. ascl:1010.068

Bellm, E. C., Kulkarni, S. R., Graham, M. J., et al. 2019, PASP, 131, 018002. doi:10.1088/1538-3873/aaecbe

Biscardi, I., Brocato, E., Arkharov, A., et al. 2012, A&A, 537, A57. doi:10.1051/0004-6361/201014160

Blanton, M. R. & Roweis, S. 2007, AJ, 133, 734. doi:10.1086/510127

Blondin, S., Dessart, L., Hillier, D. J., et al. 2013, MNRAS, 429, 2127. doi:10.1093/mnras/sts484

Bloom, J. S., Kasen, D., Shen, K. J., et al. 2012, ApJ, 744, L17. doi:10.1088/2041-8205/744/2/L17

Boehner, P., Plewa, T., & Langer, N. 2017, MNRAS, 465, 2060. doi:10.1093/mnras/stw2737

Bottinelli, L., Gouguenheim, L., Paturel, G., et al. 1984, A&AS, 56, 381

Bottinelli, L., Gouguenheim, L., Paturel, G., et al. 1986, A&A, 156, 157

Botyánszki, J., Kasen, D., & Plewa, T. 2018, ApJ, 852, L6. doi:10.3847/2041-8213/aaa07b

Bulla, M., Miller, A. A., Yao, Y., et al. 2020, ApJ, 902, 48. doi:10.3847/1538-4357/abb13c

Burns, C. R., Stritzinger, M., Phillips, M. M., et al. 2011, AJ, 141, 19. doi:10.1088/0004-6256/141/1/19

Cao, Y., Kulkarni, S. R., Howell, D. A., et al. 2015, Nature, 521, 328. doi:10.1038/nature14440

Choi, J., Dotter, A., Conroy, C., et al. 2016, ApJ, 823, 102. doi:10.3847/0004-637X/823/2/102

Chonis, T. S., Hill, G. J., Lee, H., et al. 2014, Proc. SPIE, 9147, 91470A. doi:10.1117/12.2056005

Chugai, N. N. 1986, Soviet Ast., 30, 563

Dessart, L., Blondin, S., Hillier, D. J., et al. 2014, MNRAS, 441, 532. doi:10.1093/mnras/stu598

Dessart, L., Leonard, D. C., & Prieto, J. L. 2020, A&A, 638, A80. doi:10.1051/0004-6361/202037854

Ehgamberdiev, S. 2018, Nature Astronomy, 2, 349. doi:10.1038/s41550-018-0459-3

Elias-Rosa, N., Chen, P., Benetti, S., et al. 2021, A&A, 652, A115. doi:10.1051/0004-6361/202141218

Fitzpatrick, E. L. 1999, PASP, 111, 63. doi:10.1086/316293

Fink, M., Hillebrandt, W., & Röpke, F. K. 2007, A&A, 476, 1133. doi:10.1051/0004-6361:20078438

Fink, M., Röpke, F. K., Hillebrandt, W., et al. 2010, A&A, 514, A53. doi:10.1051/0004-6361/200913892

Gonzaga, S., Hack, W., Fruchter, A., et al. 2012, The DrizzlePac Handbook, HST Data Handbook

Groenewegen, M. A. T. & Sloan, G. C. 2018, A&A, 609, A114. doi:10.1051/0004-6361/201731089

Hachisu, I., Kato, M., & Nomoto, K. 1996, ApJ, 470, L97. doi:10.1086/310303

Hachisu, I., Kato, M., Nomoto, K., et al. 1999, ApJ, 519, 314. doi:10.1086/307370

Han, X., Zheng, W., Stahl, B. E., et al. 2020, ApJ, 892, 142. doi:10.3847/1538-4357/ab7a27

Harutyunyan, A. H., Pfahler, P., Pastorello, A., et al. 2008, A&A, 488, 383. doi:10.1051/0004-6361:20078859

Harris, C. R., Millman, K. J., van der Walt, S. J., et al. 2020, Nature, 585, 357. doi:10.1038/s41586-020-2649-2

Henden, A. A., Levine, S. E., Terrell, D., et al. 2012, Journal of the American Association of Variable Star Observers (JAAVSO), 40, 430

Hicken, M., Challis, P., Jha, S., et al. 2009, ApJ, 700, 331. doi:10.1088/0004-637X/700/1/331

Hosseinzadeh, G., Sand, D. J., Valenti, S., et al. 2017, ApJ, 845, L11. doi:10.3847/2041-8213/aa8402

Hosseinzadeh, G., Sand, D. J., Lundqvist, P., et al. 2022, arXiv:2205.02236

Iben, I. & Tutukov, A. V. 1984, ApJS, 54, 335. doi:10.1086/190932

Im, M., Ko, J., Cho, Y., et al. 2010, Journal of Korean Astronomical Society, 43, 75. doi:10.5303/JKAS.2010.43.3.075

Im, M., Choi, C., Yoon, S.-C., et al. 2015, ApJS, 221, 22. doi:10.1088/0067-0049/221/1/22

Im, M., Choi, C., Hwang, S., et al. 2019, Journal of Korean Astronomical Society, 52, 11. doi:10.5303/JKAS.2019.52.1.11

Im, M., Kim, Y., Lee, C.-U., et al. 2021, Journal of Korean Astronomical Society, 54, 89

Itagaki, K. 2021, Transient Name Server Discovery Report, 2021-998

Jha, S., Riess, A. G., & Kirshner, R. P. 2007, ApJ, 659, 122. doi:10.1086/512054

Jiang, J.-A., Doi, M., Maeda, K., et al. 2017, Nature, 550, 80. doi:10.1038/nature23908

Kasen, D. 2010, ApJ, 708, 1025. doi:10.1088/0004-637X/708/2/1025

Kawabata, M., Maeda, K., Yamanaka, M., et al. 2020, ApJ, 893, 143. doi:10.3847/1538-4357/ab8236

Kowalski, M., Rubin, D., Aldering, G., et al. 2008, ApJ, 686, 749. doi:10.1086/589937

Lang, D., Hogg, D. W., Mierle, K., et al. 2010, AJ, 139, 1782

Leonard, D. C. 2007, ApJ, 670, 1275. doi:10.1086/522367

Levanon, N., Soker, N., & García-Berro, E. 2015, MNRAS, 447, 2803. doi:10.1093/mnras/stu2580

Levanon, N. & Soker, N. 2017, MNRAS, 470, 2510. doi:10.1093/mnras/stx1387

Levanon, N. & Soker, N. 2019, ApJ, 872, L7. doi:10.3847/2041-8213/ab0285

Levesque, E. M., Massey, P., Olsen, K. A. G., et al. 2005, ApJ, 628, 973. doi:10.1086/430901

Levesque, E. M., Massey, P., Olsen, K. A. G., et al. 2006, ApJ, 645, 1102. doi:10.1086/504417

Li, W., Bloom, J. S., Podsiadlowski, P., et al. 2011, Nature, 480, 348. doi:10.1038/nature10646

Liu, Z. W., Pakmor, R., Röpke, F. K., et al. 2012, A&A, 548, A2. doi:10.1051/0004-6361/201219357

Liu, Z.-W. & Stancliffe, R. J. 2016, MNRAS, 459, 1781. doi:10.1093/mnras/stw774

Lundqvist, P., Nyholm, A., Taddia, F., et al. 2015, A&A, 577, A39. doi:10.1051/0004-6361/201525719

Magnier, E. A., Schlafly, E., Finkbeiner, D., et al. 2013, ApJS, 205, 20. doi:10.1088/0067-0049/205/2/20

Maguire, K., Taubenberger, S., Sullivan, M., et al. 2016, MNRAS, 457, 3254. doi:10.1093/mnras/stv2991

Marietta, E., Burrows, A., & Fryxell, B. 2000, ApJS, 128, 615. doi:10.1086/313392

Marion, G. H., Brown, P. J., Vinkó, J., et al. 2016, ApJ, 820, 92. doi:10.3847/0004-637X/820/2/92

McCully, C., Jha, S. W., Foley, R. J., et al. 2014, Nature, 512, 54. doi:10.1038/nature13615

McCully, C., Jha, S. W., Scalzo, R. A., et al. 2022, ApJ, 925, 138. doi:10.3847/1538-4357/ac3bbd

Medford, M. S., Lu, J. R., & Schlafly, E. F. 2020, Research Notes of the American Astronomical Society, 4, 38. doi:10.3847/2515-5172/ab7f3c

Meng, X., Chen, X., & Han, Z. 2007, PASJ, 59, 835. doi:10.1093/pasj/59.4.835

Meynet, G., Chomienne, V., Ekström, S., et al. 2015, A&A, 575, A60. doi:10.1051/0004-6361/201424671

Newville, M., Stensitzki, T., Allen, D. B., et al. 2014, Zenodo

Ni, Y. Q., Moon, D.-S., Drout, M. R., et al. 2022, Nature Astronomy. doi:10.1038/s41550-022-01603-4

Noebauer, U. M., Kromer, M., Taubenberger, S., et al. 2017, MNRAS, 472, 2787. doi:10.1093/mnras/stx2093

Nomoto, K. 1982, ApJ, 253, 798. doi:10.1086/159682

Nugent, P. E., Sullivan, M., Cenko, S. B., et al. 2011, Nature, 480, 344. doi:10.1038/nature10644

Pakmor, R., Röpke, F. K., Weiss, A., et al. 2008, A&A, 489, 943. doi:10.1051/0004-6361:200810456

Pakmor, R., Kromer, M., Taubenberger, S., et al. 2013, ApJ, 770, L8. doi:10.1088/2041-8205/770/1/L8

Pan, K.-C., Ricker, P. M., & Taam, R. E. 2012, ApJ, 750, 151. doi:10.1088/0004-637X/750/2/151

Parodi, B. R., Saha, A., Sandage, A., et al. 2000, ApJ, 540, 634. doi:10.1086/309385

Piro, A. L. & Nakar, E. 2013, ApJ, 769, 67. doi:10.1088/0004-637X/769/1/67

Piro, A. L. & Morozova, V. S. 2016, ApJ, 826, 96. doi:10.3847/0004-637X/826/1/96

Phillips, M. M. 1993, ApJ, 413, L105. doi:10.1086/186970

Phillips, M. M., Lira, P., Suntzeff, N. B., et al. 1999, AJ, 118, 1766. doi:10.1086/301032

Planck Collaboration, Ade, P. A. R., Aghanim, N., et al. 2016, A&A, 594, A13. doi:10.1051/0004-6361/201525830

Polin, A., Nugent, P., & Kasen, D. 2019, ApJ, 873, 84. doi:10.3847/1538-4357/aafb6a

Press, W. H., Teukolsky, S. A., Vetterling, W. T., et al. 1992, Cambridge: University Press, —c1992, 2nd ed.

Prieto, J. L., Rest, A., & Suntzeff, N. B. 2006, ApJ, 647, 501. doi:10.1086/504307

Rabinak, I. & Waxman, E. 2011, ApJ, 728, 63. doi:10.1088/0004-637X/728/1/63

Reindl, B., Tammann, G. A., Sandage, A., et al. 2005, ApJ, 624, 532. doi:10.1086/429218

Riess, A. G., Filippenko, A. V., Challis, P., et al. 1998, AJ, 116, 1009. doi:10.1086/300499

Sand, D. J., Graham, M. L., Botyánszki, J., et al. 2018, ApJ, 863, 24. doi:10.3847/1538-4357/aacde8

Science Software Branch at STScI 2012, Astrophysics Source Code Library

Schlafly, E. F. & Finkbeiner, D. P. 2011, ApJ, 737, 103. doi:10.1088/0004-637X/737/2/103

Shappee, B. J., Piro, A. L., Stanek, K. Z., et al. 2018, ApJ, 855, 6. doi:10.3847/1538-4357/aaa1e9

Takanashi, N., Doi, M., & Yasuda, N. 2008, MNRAS, 389, 1577. doi:10.1111/j.1365-2966.2008.13694.x

Tomasella, L., Benetti, S., Cappellaro, E., et al. 2021, Transient Name Server Classification Report, 2021-1031

Tonry, J. L., Stubbs, C. W., Lykke, K. R., et al. 2012, ApJ, 750, 99. doi:10.1088/0004-637X/750/2/99

Tonry, J. L., Denneau, L., Heinze, A. N., et al. 2018, PASP, 130, 064505. doi:10.1088/1538-3873/aabadf

Tsvetkov, D. Y., Pavlyuk, N. N., Ikonnikova, N. P., et al. 2021, The Astronomer's Telegram, 14541

Tucker, M. A., Shappee, B. J., & Wisniewski, J. P. 2019, ApJ, 872, L22. doi:10.3847/2041-8213/ab0286

Tully, R. B. & Fisher, J. R. 1988, Catalog of Nearby Galaxies, by R. Brent Tully and J. Richard Fisher, pp. 224. ISBN 0521352991. Cambridge, UK: Cambridge University Press, April 1988., 224

Tully, R. B., Courtois, H. M., Dolphin, A. E., et al. 2013, AJ, 146, 86. doi:10.1088/0004-6256/146/4/86

Wang, X., Wang, L., Pain, R., et al. 2006, ApJ, 645, 488. doi:10.1086/504312

Wang, B., Meng, X., Liu, D.-D., et al. 2014, ApJ, 794, L28. doi:10.1088/2041-8205/794/2/L28

Webbink, R. F. 1984, ApJ, 277, 355. doi:10.1086/161701

Wheeler, J. C., Lecar, M., & McKee, C. F. 1975, ApJ, 200, 145. doi:10.1086/153771

Whelan, J. & Iben, I. 1973, ApJ, 186, 1007. doi:10.1086/152565

Woosley, S. E., Taam, R. E., & Weaver, T. A. 1986, ApJ, 301, 601. doi:10.1086/163926

Yamanaka, M., Maeda, K., Kawabata, M., et al. 2014, ApJ, 782, L35. doi:10.1088/2041-8205/782/2/L35

Yaron, O. 2019, Transient Name Server AstroNote, 60

Zhang, K., Wang, X., Zhang, J., et al. 2016, ApJ, 820, 67. doi:10.3847/0004-637X/820/1/67

Zhang, Y., Zhang, T., Danzengluobu, et al. 2022, PASP, 134, 074201. doi:10.1088/1538-3873/ac7583

Appendix A

Optical/Near-IR Long-term Light Curves of SN 2019ein

Table A.1. Light curve data in optical band of SN 2019ein

MJD (*day*)	Phase (*mag*)	B (*mag*)	σ_B (*mag*)	V (*mag*)	σ_V (*mag*)	R (*mag*)	σ_R (*mag*)	I (*mag*)	σ_I	Telescope
58578.85	−39.80					> 17.58				SAO
58588.63	−30.02					> 18.96				SAO
58590.82	−27.83					> 17.95				SAO
58592.64	−26.01					> 18.75				SAO
58602.76	−15.89					> 18.70				SAO
58604.44	−14.21	18.43	0.06			18.36	0.09			LOAO
58605.13	−13.52	17.43	0.05	17.15	0.03	17.42	0.04	18.43	0.07	MCD30INCH
58605.16	−13.49			17.20	0.03					CCA250
58605.22	−13.43	17.35	0.03	17.08	0.05	17.38	0.06	18.09	0.07	LOAO
58605.30	−13.35	17.25	0.02	17.00	0.05	17.27	0.06	17.98	0.05	LOAO
58605.32	−13.33	17.19	0.04	16.98	0.04	17.25	0.03	17.85	0.05	MCD30INCH
58605.39	−13.26	17.20	0.03	16.96	0.04	17.21	0.06	17.86	0.07	LOAO
58605.40	−13.26			16.92	0.05					CCA250
58605.44	−13.21	17.10	0.04	17.02	0.03	17.21	0.03			MCD30INCH
58605.47	−13.18	17.26	0.22	16.99	0.06	17.27	0.06	17.75	0.10	SAO

Table A.1 (cont'd)

MJD (*day*)	Phase (*mag*)	B (*mag*)	σ_B (*mag*)	V (*mag*)	σ_V (*mag*)	R (*mag*)	σ_R (*mag*)	I (*mag*)	σ_I	Telescope
58605.60	−13.05	16.93	0.03	16.85	0.04	17.03	0.04			DOAO
58605.70	−12.95	16.89	0.03	16.73	0.03	16.95	0.03			DOAO
58605.73	−12.92	16.90	0.07	16.78	0.04	16.90	0.01	17.57	0.08	SAO
58605.74	−12.91	16.88	0.03	16.69	0.04	16.95	0.04	17.50	0.07	DOAO
58605.77	−12.88	16.78	0.06	16.66	0.04	16.95	0.03	17.35	0.06	DOAO
58605.79	−12.86	16.84	0.05	16.64	0.03	16.89	0.05	17.42	0.05	DOAO
58605.80	−12.85	16.75	0.05	16.65	0.03	16.95	0.03	17.53	0.06	DOAO
58605.80	−12.85	16.77	0.05							DOAO
58606.20	−12.45					16.77	0.12			MCD30INCH
58606.27	−12.39	16.47	0.03	16.37	0.04	16.61	0.03	17.08	0.07	LOAO
58606.35	−12.31	16.44	0.04	16.35	0.04	16.55	0.05	17.00	0.05	LOAO
58606.43	−12.22	16.38	0.03	16.30	0.03	16.54	0.04	16.87	0.04	LOAO
58606.47	−12.18	16.36	0.06	16.22	0.02	16.53	0.03	16.83	0.03	DOAO
58606.52	−12.13	16.45	0.21	16.25	0.06	16.47	0.05	16.94	0.07	SAO
58606.55	−12.10	16.29	0.07	16.28	0.03	16.38	0.03	16.98	0.06	SOAO

Table A.1 (cont'd)

MJD (*day*)	Phase (*mag*)	B (*mag*)	σ_B (*mag*)	V (*mag*)	σ_V (*mag*)	R (*mag*)	σ_R (*mag*)	I (*mag*)	σ_I	Telescope
58606.56	−12.09	16.30	0.05	16.18	0.04	16.44	0.04	16.73	0.03	DOAO
58606.60	−12.05	16.30	0.04	16.22	0.02	16.52	0.02	16.76	0.02	DOAO
58606.62	−12.03	16.21	0.04	16.18	0.03	16.38	0.03	16.73	0.02	DOAO
58606.63	−12.02	16.25	0.02	16.14	0.02	16.38	0.03	16.71	0.05	DOAO
58606.65	−12.00	16.33	0.14	16.20	0.04	16.42	0.05	16.87	0.07	SAO
58606.75	−11.90	16.34	0.15	16.17	0.08			16.81	0.12	SAO
58606.77	−11.88	16.24	0.10	16.12	0.04	16.33	0.04	16.73	0.05	SOAO
58606.80	−11.85	16.24	0.05	16.08	0.04	16.34	0.04	16.77	0.05	DOAO
58606.80	−11.85	16.26	0.07							DOAO
58607.18	−11.47	15.92	0.04	15.95	0.04	16.15	0.03	16.44	0.04	LOAO
58607.31	−11.34	15.87	0.04	15.84	0.04	16.10	0.04	16.34	0.04	LOAO
58607.40	−11.25	15.83	0.04	15.79	0.04	16.06	0.03	16.36	0.06	LOAO
58607.63	−11.02	15.71	0.05	15.68	0.04	15.88	0.04	16.15	0.02	DOAO
58607.63	−11.02	15.75	0.04							DOAO
58608.22	−10.43	15.44	0.03	15.49	0.03	15.67	0.04	15.95	0.05	LOAO

Table A.1 (cont'd)

MJD (*day*)	Phase (*mag*)	B (*mag*)	σ_B (*mag*)	V (*mag*)	σ_V (*mag*)	R (*mag*)	σ_R (*mag*)	I (*mag*)	σ_I	Telescope
58608.27	−10.38			15.46	0.02	15.63	0.02	15.95	0.04	MCD30INCH
58608.28	−10.37			15.40	0.12					CCA250
58608.30	−10.35	15.39	0.03	15.45	0.04	15.65	0.04	15.94	0.04	LOAO
58608.38	−10.27	15.37	0.03	15.42	0.04	15.60	0.03	15.92	0.06	LOAO
58608.43	−10.22	15.38	0.03			15.55	0.02	15.95	0.04	MCD30INCH
58608.54	−10.12	15.26	0.06	15.43	0.04					DOAO
58608.55	−10.10	15.33	0.04	15.42	0.01	15.57	0.05	15.85	0.08	DOAO
58608.55	−10.10	15.35	0.05	15.39	0.04	15.53	0.03	15.86	0.05	SOAO
58608.56	−10.10	15.31	0.06	15.35	0.04	15.51	0.03	15.84	0.08	DOAO
58608.56	−10.09	15.35	0.04	15.36	0.02					DOAO
58608.78	−9.87	15.18	0.05	15.23	0.03			15.75	0.05	DOAO
58608.80	−9.85	15.16	0.04	15.24	0.01	15.39	0.04	15.70	0.05	DOAO
58608.80	−9.85	15.17	0.05	15.24	0.02					DOAO
58609.17	−9.49	15.04	0.02	15.16	0.03					MCD30INCH
58609.19	−9.47			15.16	0.07					CCA250

Table A.1 (cont'd)

MJD (*day*)	Phase (*mag*)	B (*mag*)	σ_B (*mag*)	V (*mag*)	σ_V (*mag*)	R (*mag*)	σ_R (*mag*)	I (*mag*)	σ_I	Telescope
58609.28	−9.37	15.05	0.03	15.10	0.03	15.28	0.05	15.57	0.04	LOAO
58609.37	−9.28	15.01	0.04							MCD30INCH
58609.40	−9.25			15.06	0.02					CCA250
58609.50	−9.15	14.94	0.05	15.03	0.02	15.12	0.04	15.42	0.04	SAO
58609.60	−9.05	14.97	0.04	15.04	0.02	15.11	0.02	15.48	0.02	SOAO
58609.67	−8.99	14.93	0.06	15.03	0.03	15.05	0.03	15.42	0.06	SAO
58609.76	−8.89	14.93	0.05	15.02	0.02	15.07	0.02	15.47	0.04	SOAO
58609.77	−8.89	14.89	0.05	15.01	0.02	15.06	0.03	15.34	0.04	SAO
58610.40	−8.25	14.71	0.02	14.79	0.04	14.88	0.03			MCD30INCH
58610.40	−8.25			14.81	0.03					CCA250
58610.42	−8.23	14.65	0.02	14.77	0.04	14.84	0.04	15.23	0.05	LOAO
58610.49	−8.16	14.59	0.03	14.72	0.03	14.82	0.06	15.14	0.02	DOAO
58610.50	−8.15	14.63	0.01	14.69	0.03	14.85	0.06	15.10	0.01	DOAO
58610.56	−8.09	14.59	0.03	14.69	0.02	14.83	0.04	15.13	0.02	DOAO
58610.59	−8.06	14.60	0.03	14.76	0.02	14.76	0.02	15.11	0.04	SAO

Table A.1 (cont'd)

MJD (*day*)	Phase (*mag*)	B (*mag*)	σ_B (*mag*)	V (*mag*)	σ_V (*mag*)	R (*mag*)	σ_R (*mag*)	I (*mag*)	σ_I	Telescope
58610.60	−8.05	14.67	0.04	14.75	0.02	14.79	0.01	15.20	0.04	SOAO
58610.76	−7.89	14.65	0.04	14.74	0.01	14.79	0.01	15.15	0.04	SOAO
58611.20	−7.45	14.46	0.02	14.60	0.04	14.70	0.02	15.05	0.06	LOAO
58611.40	−7.26			14.56	0.02					CCA250
58612.29	−6.36	14.21	0.02	14.37	0.04	14.48	0.05	14.87	0.05	LOAO
58612.36	−6.29					14.44	0.01	14.78	0.03	MCD30INCH
58612.37	−6.28			14.35	0.02					CCA250
58612.49	−6.16	14.15	0.01	14.33	0.01	14.40	0.03	14.79	0.04	DOAO
58612.52	−6.13	14.18	0.01	14.30	0.03	14.40	0.04	14.76	0.01	DOAO
58612.72	−5.93	14.16	0.02	14.32	0.02	14.33	0.04	14.74	0.04	SAO
58613.49	−5.16	13.99	0.02	14.14	0.02	14.26	0.03			DOAO
58614.44	−4.21	13.94	0.03	14.07	0.04	14.18	0.05	14.65	0.05	LOAO
58615.15	−3.50			13.92	0.02					CCA250
58615.58	−3.07					14.06	0.01			SOAO
58616.25	−2.41	13.73	0.02	13.88	0.05	14.00	0.06	14.59	0.05	LOAO

Table A.1 (cont'd)

MJD (*day*)	Phase (*mag*)	B (*mag*)	σ_B (*mag*)	V (*mag*)	σ_V (*mag*)	R (*mag*)	σ_R (*mag*)	I (*mag*)	σ_I	Telescope
58617.14	−1.51	13.77	0.04							MCD30INCH
58617.14	−1.51			13.79	0.02					CCA250
58617.15	−1.50	13.74	0.06	13.85	0.06	13.95	0.04	14.63	0.06	LOAO
58617.32	−1.33	13.70	0.01							MCD30INCH
58617.54	−1.11	13.68	0.04	13.82	0.01	13.90	0.02	14.54	0.04	SAO
58618.23	−0.42	13.71	0.04	13.79	0.04	13.92	0.06	14.61	0.06	LOAO
58618.60	−0.06					13.89	0.03			SAO
58618.60	−0.05					13.89	0.01			SOAO
58619.52	0.87	13.74	0.03	13.80	0.04	13.90	0.05	14.65	0.05	DOAO
58619.58	0.93					13.88	0.04			SOAO
58619.61	0.96					13.88	0.02			SAO
58621.21	2.56	13.81	0.05	13.76	0.03	13.88	0.04	14.68	0.08	LOAO
58622.30	3.65	13.87	0.03			13.91	0.05			LOAO
58623.64	4.99					13.90	0.01			DOAO
58623.70	5.04					13.93	0.01			DOAO

Table A.1 (cont'd)

MJD	Phase	B	σ_B	V	σ_V	R	σ_R	I	σ_I	Telescope
(*day*)	(*mag*)	(*mag*)	(*mag*)	(*mag*)	(*mag*)	(*mag*)	(*mag*)	(*mag*)		
58624.28	5.63	14.01	0.03	13.89	0.04	14.07	0.04	14.86	0.04	LOAO
58624.50	5.85	13.93	0.06	13.83	0.04	14.01	0.04	14.85	0.04	SAO
58624.58	5.92	13.94	0.02	13.86	0.01	14.06	0.03	14.84	0.01	DOAO
58625.24	6.59	14.08	0.04	13.91	0.04	14.09	0.04	14.93	0.07	LOAO
58625.49	6.84	14.10	0.04	13.90	0.01	14.11	0.03	14.88	0.05	SAO
58625.74	7.09					14.13	0.03			SAO
58626.22	7.57	14.19	0.03	13.97	0.04	14.19	0.04	15.04	0.05	LOAO
58626.53	7.88	14.17	0.03	13.97	0.02	14.20	0.01	15.02	0.04	SAO
58627.21	8.56	14.27	0.02	14.03	0.03	14.35	0.03	15.12	0.05	LOAO
58628.22	9.57	14.42	0.02	14.11	0.03	14.42	0.04	15.16	0.04	LOAO
58629.20	10.55	14.52	0.03	14.18	0.03	14.52	0.03	15.20	0.05	LOAO
58630.26	11.61	14.66	0.04	14.27	0.04	14.56	0.02	15.23	0.06	LOAO
58630.37	11.72	14.66	0.02							MCD30INCH
58631.21	12.56	14.78	0.03	14.33	0.03	14.62	0.03	15.21	0.05	LOAO
58631.68	13.03	14.81	0.04	14.34	0.02	14.60	0.03	15.19	0.05	SAO

Table A.1 (cont'd)

MJD (*day*)	Phase (*mag*)	B (*mag*)	σ_B (*mag*)	V (*mag*)	σ_V (*mag*)	R (*mag*)	σ_R (*mag*)	I (*mag*)	σ_I	Telescope
58632.26	13.61	14.93	0.03	14.38	0.03	14.66	0.01	15.20	0.02	MCD30INCH
58632.27	13.62	14.93	0.03	14.41	0.03	14.68	0.03	15.15	0.04	LOAO
58632.50	13.85	14.92	0.04	14.40	0.02	14.59	0.02	15.15	0.05	SAO
58633.19	14.54	15.08	0.03	14.45	0.04	14.65	0.04	15.13	0.06	LOAO
58633.21	14.56	15.03	0.02			14.68	0.02	15.15	0.03	MCD30INCH
58634.22	15.57	15.19	0.04	14.52	0.04	14.64	0.04	15.09	0.07	LOAO
58635.29	16.64	15.32	0.02	14.56	0.04	14.60	0.04	15.04	0.05	LOAO
58636.31	17.66	15.43	0.03	14.63	0.03	14.66	0.03	14.99	0.07	LOAO
58637.28	18.63	15.54	0.03	14.67	0.03	14.71	0.01	14.96	0.06	LOAO
58638.28	19.63	15.65	0.03	14.74	0.04	14.72	0.04	14.92	0.05	LOAO
58638.32	19.67	15.70	0.02							MCD30INCH
58638.59	19.94	15.65	0.03	14.74	0.01	14.70	0.02	14.93	0.05	DOAO
58639.15	20.50	15.78	0.03	14.83	0.03	14.70	0.03	14.93	0.06	LOAO
58640.22	21.57	15.86	0.03	14.89	0.04	14.77	0.04	14.89	0.04	LOAO
58640.30	21.64	15.86	0.02	14.85	0.02	14.75	0.01	14.89	0.02	MCD30INCH

Table A.1 (cont'd)

MJD (*day*)	Phase (*mag*)	B (*mag*)	σ_B (*mag*)	V (*mag*)	σ_V (*mag*)	R (*mag*)	σ_R (*mag*)	I (*mag*)	σ_I	Telescope
58641.23	22.58	15.95	0.04	15.00	0.03	14.83	0.05	14.91	0.04	LOAO
58642.31	23.66	15.99	0.02			14.91	0.02	15.01	0.04	MCD30INCH
58643.32	24.67	16.16	0.03	15.21	0.03	14.98	0.04	15.07	0.10	LOAO
58645.22	26.57	16.32	0.03	15.40	0.03	15.15	0.03	15.21	0.04	LOAO
58645.53	26.88	16.28	0.13	15.37	0.03	15.18	0.02	15.24	0.05	SAO
58645.63	26.98					15.27	0.04			SOAO
58645.65	27.00	16.23	0.10	15.38	0.03	15.17	0.03	15.26	0.05	SAO
58646.16	27.51	16.50	0.10	15.47	0.04	15.24	0.04	15.41	0.10	LOAO
58646.55	27.90	16.45	0.14	15.47	0.03	15.23	0.03	15.36	0.03	SAO
58646.61	27.96					15.25	0.03			SOAO
58647.17	28.51	16.48	0.04	15.52	0.03	15.30	0.03	15.39	0.04	LOAO
58648.29	29.64	16.50	0.03	15.60	0.04	15.37	0.05	15.48	0.07	LOAO
58648.57	29.92	16.52	0.08	15.54	0.01	15.38	0.02	15.48	0.05	SAO
58648.71	30.06	16.49	0.02	15.57	0.02	15.37	0.04			MAO
58649.30	30.65	16.50	0.04	15.66	0.04	15.55	0.05	15.57	0.07	LOAO

Table A.1 (cont'd)

MJD	Phase	B	σ_B	V	σ_V	R	σ_R	I	σ_I	Telescope
(*day*)	(*mag*)	(*mag*)	(*mag*)	(*mag*)	(*mag*)	(*mag*)	(*mag*)	(*mag*)		
58649.54	30.89	16.54	0.04	15.61	0.03	15.49	0.03			DOAO
58649.57	30.92	16.59	0.06	15.61	0.02	15.46	0.02	15.58	0.02	SAO
58649.70	31.05	16.50	0.01	15.63	0.01	15.43	0.04			MAO
58650.15	31.50	16.69	0.06	15.67	0.05	15.50	0.03	15.60	0.04	LOAO
58650.73	32.08	16.54	0.01	15.68	0.01	15.49	0.04			MAO
58651.17	32.52	16.62	0.06	15.75	0.04	15.56	0.04	15.69	0.08	LOAO
58652.26	33.61	16.68	0.05	15.80	0.06	15.62	0.05	15.70	0.06	LOAO
58652.68	34.03	16.62	0.02	15.74	0.02	15.58	0.04			MAO
58653.24	34.59	16.71	0.04	15.80	0.05	15.63	0.05	15.79	0.05	LOAO
58653.69	35.04	16.64	0.01	15.79	0.02	15.64	0.05			MAO
58654.24	35.59	16.70	0.03	15.85	0.04	15.75	0.04	15.89	0.04	LOAO
58655.24	36.59	16.77	0.03	15.91	0.03	15.76	0.04	15.94	0.05	LOAO
58655.68	37.03	16.79	0.23	15.85	0.05					SAO
58656.23	37.57	16.79	0.03	15.91	0.03	15.77	0.04	15.98	0.04	LOAO
58657.25	38.60	16.81	0.03			15.80	0.03			LOAO

Table A.1 (cont'd)

MJD (*day*)	Phase (*mag*)	B (*mag*)	σ_B (*mag*)	V (*mag*)	σ_V (*mag*)	R (*mag*)	σ_R (*mag*)	I (*mag*)	σ_I	Telescope
58658.23	39.58	16.82	0.03	15.98	0.04	15.88	0.03	16.07	0.05	LOAO
58659.54	40.89	16.97	0.10	15.97	0.03			16.09	0.05	SAO
58660.23	41.58	16.88	0.03	16.06	0.05	15.92	0.04	16.17	0.04	LOAO
58662.19	43.54			16.12	0.04					LOAO
58665.24	46.59			16.24	0.06			16.43	0.13	LOAO
58665.70	47.05	16.87	0.02	16.11	0.04	16.04	0.06			MAO
58666.50	47.85	16.92	0.07	16.17	0.03	16.15	0.04	16.47	0.05	SAO
58667.20	48.55			16.27	0.03	16.17	0.04	16.49	0.04	LOAO
58667.50	48.85	16.88	0.10	16.22	0.03	16.14	0.03	16.49	0.04	SAO
58668.73	50.08	16.90	0.02	16.22	0.00	16.15	0.05			MAO
58669.21	50.56			16.30	0.04	16.21	0.04	16.57	0.06	LOAO
58669.71	51.06	16.90	0.01	16.26	0.01	16.20	0.02			MAO
58670.71	52.06	16.92	0.01	16.33	0.02	16.23	0.02			MAO
58671.71	53.05	16.94	0.02	16.32	0.03	16.25	0.04			MAO
58672.22	53.57			16.38	0.03	16.42	0.05	16.81	0.05	LOAO

Table A.1 (cont'd)

MJD	Phase	B	σ_B	V	σ_V	R	σ_R	I	σ_I	Telescope
(*day*)	(*mag*)	(*mag*)	(*mag*)	(*mag*)	(*mag*)	(*mag*)	(*mag*)	(*mag*)		
58672.62	53.96			16.32	0.03	16.45	0.03	16.73	0.06	SAO
58673.27	54.62					16.38	0.04			LOAO
58673.72	55.07	16.98	0.02	16.36	0.02	16.33	0.04			MAO
58674.20	55.55			16.43	0.04	16.40	0.03	16.84	0.05	LOAO
58675.70	57.05	17.01	0.02	16.42	0.02	16.40	0.03			MAO
58676.71	58.06	16.99	0.02	16.47	0.01	16.36	0.02			MAO
58677.51	58.86			16.45	0.06	16.47	0.06	17.01	0.07	SAO
58677.71	59.06	17.04	0.02	16.47	0.01	16.45	0.04			MAO
58679.70	61.05	17.05	0.02	16.54	0.02	16.53	0.04			MAO
58680.21	61.56			16.62	0.05	16.63	0.04	16.94	0.04	LOAO
58680.26	61.61					16.61	0.07			LOAO
58680.71	62.06	17.08	0.02	16.53	0.02	16.53	0.04			MAO
58683.72	65.07	17.08	0.02	16.63	0.02	16.66	0.04			MAO
58702.52	83.87	17.38	0.04	17.15	0.02	17.36	0.04	17.75	0.05	DOAO
58739.13	120.48			17.83	0.15					LOAO

Table A.1 (cont'd)

MJD (*day*)	Phase (*mag*)	B (*mag*)	σ_B (*mag*)	V (*mag*)	σ_V (*mag*)	R (*mag*)	σ_R (*mag*)	I (*mag*)	σ_I	Telescope
58740.12	121.47			17.85	0.17	18.57	0.25	19.51	0.22	LOAO
58744.11	125.46	18.11	0.09	18.04	0.06	18.72	0.15			LOAO
58747.10	128.45	18.22	0.09	18.08	0.08					LOAO
58748.10	129.44					18.78	0.11	18.51	0.19	LOAO

Table A.2. Light curve data in Near-IR bands from UKIRT observation of SN 2019ein

MJD	Phase (*day*)	J (*mag*)	σ_J (*mag*)	H (*mag*)	σ_H (*mag*)	K (*mag*)	σ_K (*mag*)
58605.35	−13.30	17.98	0.03	17.69	0.04	18.63	0.13
58610.35	−8.30	15.85	0.02	16.20	0.03	16.74	0.03
58611.34	−7.31	15.64	0.02	16.04	0.03	16.59	0.03
58612.37	−6.28	15.48	0.02	15.90	0.03	16.38	0.03
58613.28	−5.37	15.39	0.02	15.83	0.02	16.30	0.03
58614.36	−4.29	15.33	0.03	15.81	0.03	16.27	0.03
58615.33	−3.32	15.30	0.02	15.78	0.02	16.21	0.03
58616.27	−2.38	15.30	0.02	15.78	0.03	16.22	0.03
58617.28	−1.37	15.33	0.02	15.83	0.03	16.20	0.03
58618.24	−0.41	15.38	0.02	15.86	0.03	16.28	0.03
58619.36	0.71	15.45	0.02	15.95	0.03	16.28	0.03
58620.33	1.68	15.52	0.02	15.91	0.03	16.31	0.03
58621.33	2.68	15.61	0.02	16.02	0.03	16.36	0.03
58622.35	3.70	15.71	0.02	16.02	0.03	16.39	0.03
58623.32	4.67	15.89	0.03	16.10	0.03	16.55	0.03
58624.36	5.71	16.12	0.02			16.61	0.04
58625.39	6.74	16.39	0.02	16.15	0.03	16.60	0.04
58626.26	7.61	16.63	0.03	16.22	0.03	16.62	0.03
58627.35	8.70	16.84	0.02	16.19	0.03	16.70	0.03
58628.32	9.67	16.91	0.02	16.19	0.03	16.62	0.03
58629.31	10.65	17.01	0.03	16.29	0.03	16.76	0.03
58631.28	12.63	17.06	0.02	16.23	0.03	16.65	0.03
58633.32	14.66	16.98	0.03	16.15	0.03	16.63	0.03

Table A.2 (cont'd)

MJD	Phase (*day*)	J (*mag*)	σ_J (*mag*)	H (*mag*)	σ_H (*mag*)	K (*mag*)	σ_K (*mag*)
58633.33	14.68	16.98	0.03	16.08	0.02	16.60	0.03
58633.34	14.69	16.97	0.03	16.11	0.02	16.56	0.03
58635.26	16.61	16.82	0.02	15.98	0.03	16.43	0.03
58637.34	18.69	16.65	0.02	15.76	0.03	16.31	0.03
58639.35	20.70	16.43	0.03	15.85	0.03	16.40	0.03
58641.26	22.61	16.27	0.03	15.87	0.02	16.45	0.03
58643.40	24.74	16.29	0.02	16.03	0.03	16.59	0.03
58645.23	26.58	16.47	0.02	16.17	0.03	16.73	0.03
58647.30	28.65	16.74	0.02	16.38	0.03	16.95	0.03
58649.24	30.59	16.95	0.03	16.37	0.03	17.14	0.05
58651.23	32.58	17.18	0.03	16.33	0.03	17.13	0.05
58653.23	34.58	17.33	0.03	16.48	0.03	17.52	0.06
58655.25	36.60	17.48	0.03	16.75	0.03	17.31	0.05
58659.25	40.60	17.86	0.04	17.01	0.03	17.81	0.08
58659.26	40.61	17.94	0.03	16.94	0.03	17.66	0.06
58662.39	43.74	18.19	0.04	16.86	0.03	17.86	0.09
58668.26	49.61	18.60	0.04	17.18	0.03	17.90	0.06
58674.28	55.63	19.09	0.06	17.38	0.03	18.00	0.06
58679.26	60.61	19.41	0.07	17.72	0.04	18.28	0.06

Appendix B

Optical Long-term Light Curves of SN 2021hpr

Table 2. Optical light curve of SN 2021hpr with no extinction corrected. The 5σ detection limits are also presented.

MJD	Phase (*day*)	Magnitude (*mag*)	σ_{Mag} (*mag*)	Telescope
		B band		
59256.85	−65.04	> 20.57	-	6
59258.77	−63.13	> 22.36	-	6
59259.83	−62.06	> 22.51	-	6
59260.76	−61.13	> 22.51	-	6
59261.71	−60.18	> 22.45	-	6
59262.73	−59.16	> 21.72	-	6
59275.26	−46.63	> 19.33	-	1
59276.53	−45.37	> 19.76	-	1
59277.26	−44.64	> 21.06	-	1
59280.26	−41.63	> 21.23	-	1
59283.33	−38.56	> 21.33	-	1
59288.34	−33.55	> 21.10	-	1
59295.12	−26.77	> 20.22	-	1
59298.48	−23.42	> 17.02	-	5
59298.48	−23.41	> 17.14	-	3
59301.16	−20.73	> 19.68	-	1
59302.21	−19.68	> 18.90	-	1
59303.27	−18.63	> 19.21	-	1
59303.54	−18.35	> 17.53	-	5
59304.18	−17.72	> 20.11	-	1
59305.29	−16.60	18.75	0.09	1

Table 2 (cont'd)

MJD	Phase (*day*)	Magnitude (*mag*)	σ_{Mag} (*mag*)	Telescope
59306.27	−15.62	18.02	0.04	1
59308.22	−13.67	17.22	0.04	1
59308.38	−13.51	17.08	0.04	1
59308.57	−13.32	17.11	0.13	2
59308.65	−13.24	17.08	0.11	4
59309.21	−12.69	16.50	0.03	1
59309.34	−12.56	16.41	0.04	1
59309.47	−12.42	16.49	0.03	3
59309.54	−12.35	16.22	0.07	5
59310.19	−11.70	15.89	0.04	1
59310.26	−11.64	15.86	0.03	1
59310.34	−11.55	15.82	0.04	1
59310.47	−11.43	15.87	0.05	2
59310.63	−11.27	15.82	0.01	3
59310.64	−11.25	15.80	0.04	4
59311.19	−10.70	15.45	0.04	1
59311.34	−10.56	15.41	0.04	1
59311.63	−10.26	15.39	0.02	4
59311.64	−10.26	15.29	0.06	5
59312.17	−9.73	15.12	0.06	1
59312.35	−9.54	15.09	0.05	1
59312.52	−9.37	15.16	0.02	3

Table 2 (cont'd)

MJD	Phase (*day*)	Magnitude (*mag*)	σ_{Mag} (*mag*)	Telescope
59312.72	−9.17	14.98	0.01	6
59313.23	−8.66	14.86	0.04	1
59313.39	−8.50	14.83	0.04	1
59313.57	−8.32	14.81	0.04	5
59313.59	−8.30	14.94	0.02	3
59314.16	−7.73	14.68	0.07	1
59314.37	−7.52	14.65	0.04	1
59314.48	−7.41	14.80	0.02	3
59314.65	−7.25	14.68	0.03	4
59314.65	−7.24	14.74	0.04	3
59315.22	−6.67	14.51	0.04	1
59315.39	−6.50	14.53	0.03	1
59315.65	−6.24	14.48	0.01	6
59316.21	−5.69	14.38	0.06	1
59317.17	−4.72	14.30	0.04	1
59317.26	−4.63	14.30	0.04	1
59317.38	−4.51	14.30	0.04	1
59317.50	−4.39	14.29	0.04	5
59317.56	−4.34	14.28	0.06	2
59318.18	−3.72	14.21	0.03	1
59318.36	−3.54	14.23	0.03	1
59318.46	−3.44	14.29	0.06	2

Table 2 (cont'd)

MJD	Phase (*day*)	Magnitude (*mag*)	σ_{Mag} (*mag*)	Telescope
59318.47	−3.42	14.27	0.04	4
59318.48	−3.41	14.37	0.03	3
59318.50	−3.39	14.21	0.04	5
59318.65	−3.24	14.35	0.02	3
59319.35	−2.54	14.19	0.04	1
59319.48	−2.41	14.33	0.03	3
59319.48	−2.41	14.25	0.03	4
59319.49	−2.40	14.19	0.04	5
59319.58	−2.31	14.32	0.01	3
59319.67	−2.22	14.33	0.02	3
59320.18	−1.71	14.19	0.07	1
59320.67	−1.23	14.17	0.02	6
59321.18	−0.71	14.14	0.03	1
59321.35	−0.54	14.15	0.04	1
59321.48	−0.41	14.29	0.02	3
59321.56	−0.34	14.20	0.02	2
59321.59	−0.30	14.28	0.02	3
59321.68	−0.21	14.29	0.02	3
59322.18	0.29	14.14	0.04	1
59322.35	0.46	14.16	0.04	1
59322.48	0.59	14.29	0.03	3
59322.56	0.67	14.21	0.03	4

Table 2 (cont'd)

MJD	Phase (*day*)	Magnitude (*mag*)	σ_{Mag} (*mag*)	Telescope
59322.59	0.69	14.27	0.01	3
59322.67	0.78	14.29	0.02	3
59323.19	1.30	14.16	0.03	1
59323.36	1.46	14.17	0.03	1
59323.48	1.58	14.20	0.02	4
59323.48	1.59	14.33	0.04	3
59323.50	1.60	14.20	0.11	2
59323.58	1.69	14.19	0.05	5
59323.65	1.76	14.31	0.02	3
59324.35	2.46	14.19	0.03	1
59325.19	3.30	14.20	0.04	1
59325.35	3.46	14.22	0.04	1
59326.19	4.30	14.24	0.04	1
59326.35	4.46	14.26	0.03	1
59326.67	4.78	14.27	0.02	6
59327.19	5.29	14.27	0.03	1
59327.35	5.46	14.30	0.04	1
59328.19	6.30	14.34	0.04	1
59328.35	6.46	14.36	0.04	1
59329.18	7.28	14.39	0.06	1
59329.36	7.47	14.41	0.07	1
59330.19	8.29	14.47	0.04	1

Table 2 (cont'd)

MJD	Phase (*day*)	Magnitude (*mag*)	σ_{Mag} (*mag*)	Telescope
59331.68	9.79	14.61	0.02	6
59332.37	10.48	14.66	0.03	1
59332.71	10.82	14.70	0.01	6
59333.63	11.74	14.78	0.02	6
59334.27	12.38	14.85	0.04	1
59335.63	13.74	15.08	0.03	3
59336.22	14.33	15.05	0.04	1
59336.54	14.64	15.14	0.05	5
59336.56	14.67	15.22	0.01	3
59337.19	15.30	15.17	0.04	1
59338.15	16.26	15.28	0.03	1
59339.15	17.26	15.39	0.04	1
59339.49	17.60	15.51	0.05	5
59339.50	17.61	15.51	0.03	4
59340.18	18.28	15.50	0.04	1
59341.54	19.65	15.75	0.02	3
59342.18	20.29	15.74	0.04	1
59343.15	21.26	15.85	0.04	1
59343.55	21.66	16.01	0.02	3
59344.15	22.26	15.93	0.04	1
59345.15	23.26	16.02	0.04	1
59346.15	24.26	16.14	0.04	1

Table 2 (cont'd)

MJD	Phase (*day*)	Magnitude (*mag*)	σ_{Mag} (*mag*)	Telescope
59346.54	24.65	16.28	0.08	5
59347.15	25.26	16.26	0.04	1
59347.53	25.64	16.29	0.10	5
59347.70	25.81	16.32	0.01	6
59348.15	26.26	16.32	0.03	1
59350.16	28.26	16.51	0.03	1
59351.22	29.32	16.54	0.04	1
		V band		
59258.77	-63.12	> 22.23	-	6
59259.84	-62.05	> 22.36	-	6
59260.76	-61.13	> 22.45	-	6
59261.71	-60.18	> 22.30	-	6
59262.73	-59.16	> 21.65	-	6
59275.27	-46.62	> 19.05	-	1
59276.53	-45.36	> 19.44	-	1
59277.27	-44.62	> 20.66	-	1
59280.27	-41.62	> 20.73	-	1
59283.35	-38.55	> 20.69	-	1
59288.36	-33.53	> 20.62	-	1
59295.14	-26.76	> 20.14	-	1
59298.48	-23.41	> 17.86	-	3
59301.18	-20.72	> 19.74	-	1

Table 2 (cont'd)

MJD	Phase (*day*)	Magnitude (*mag*)	σ_{Mag} (*mag*)	Telescope
59308.25	−13.64	16.65	0.01	1
59308.59	−13.30	16.55	0.07	2
59308.65	−13.24	16.41	0.05	4
59309.21	−12.68	16.13	0.02	1
59309.34	−12.55	15.99	0.04	1
59309.48	−12.41	16.11	0.04	3
59309.54	−12.35	16.10	0.04	5
59310.20	−11.70	15.69	0.01	1
59310.27	−11.62	15.68	0.03	1
59310.34	−11.55	15.61	0.01	1
59310.50	−11.39	15.72	0.03	2
59310.64	−11.26	15.66	0.02	3
59310.64	−11.25	15.63	0.03	4
59311.19	−10.70	15.36	0.03	1
59311.34	−10.55	15.31	0.01	1
59311.63	−10.26	15.30	0.03	4
59311.65	−10.24	15.39	0.04	5
59312.17	−9.72	15.10	0.02	1
59312.36	−9.53	15.05	0.03	1
59312.53	−9.37	15.14	0.02	3
59312.73	−9.16	15.02	0.01	6
59313.23	−8.66	14.86	0.02	1

Table 2 (cont'd)

MJD	Phase (*day*)	Magnitude (*mag*)	σ_{Mag} (*mag*)	Telescope
59313.40	−8.50	14.83	0.02	1
59313.57	−8.32	14.90	0.03	5
59313.60	−8.29	14.93	0.02	3
59314.17	−7.72	14.72	0.02	1
59314.38	−7.52	14.65	0.03	1
59314.49	−7.40	14.77	0.03	3
59314.65	−7.24	14.69	0.03	4
59314.66	−7.24	14.77	0.03	3
59315.22	−6.67	14.57	0.01	1
59315.40	−6.50	14.54	0.02	1
59315.66	−6.24	14.57	0.01	6
59316.21	−5.68	14.44	0.02	1
59317.18	−4.72	14.36	0.02	1
59317.28	−4.62	14.38	0.02	1
59317.39	−4.50	14.34	0.01	1
59317.51	−4.39	14.43	0.03	5
59317.57	−4.32	14.43	0.02	2
59318.18	−3.71	14.28	0.02	1
59318.36	−3.53	14.27	0.02	1
59318.47	−3.42	14.32	0.04	2
59318.48	−3.41	14.31	0.02	4
59318.49	−3.41	14.37	0.04	3

Table 2 (cont'd)

MJD	Phase (*day*)	Magnitude (*mag*)	$\sigma_{\rm Mag}$ (*mag*)	Telescope
59318.50	−3.39	14.34	0.02	5
59318.65	−3.24	14.37	0.03	3
59319.36	−2.54	14.22	0.01	1
59319.48	−2.41	14.27	0.02	4
59319.49	−2.40	14.32	0.04	3
59319.49	−2.40	14.28	0.03	5
59319.59	−2.30	14.33	0.03	3
59319.68	−2.22	14.33	0.02	3
59320.19	−1.71	14.35	0.19	1
59320.67	−1.22	14.24	0.01	6
59321.18	−0.71	14.17	0.01	1
59321.36	−0.54	14.15	0.02	1
59321.49	−0.40	14.23	0.03	3
59321.57	−0.33	14.20	0.06	2
59321.60	−0.29	14.26	0.03	3
59321.69	−0.21	14.28	0.01	3
59322.19	0.30	14.14	0.02	1
59322.35	0.46	14.13	0.02	1
59322.49	0.60	14.24	0.03	3
59322.56	0.67	14.18	0.03	4
59322.59	0.70	14.25	0.02	3
59322.68	0.79	14.26	0.03	3

Table 2 (cont'd)

MJD	Phase (*day*)	Magnitude (*mag*)	$\sigma_{\rm Mag}$ (*mag*)	Telescope
59323.20	1.30	14.14	0.01	1
59323.36	1.47	14.12	0.02	1
59323.48	1.59	14.17	0.03	4
59323.49	1.59	14.23	0.04	3
59323.51	1.62	14.14	0.08	2
59323.58	1.69	14.20	0.03	5
59323.66	1.76	14.26	0.03	3
59324.36	2.46	14.13	0.01	1
59325.20	3.30	14.18	0.01	1
59325.36	3.47	14.12	0.02	1
59326.19	4.30	14.13	0.02	1
59326.36	4.46	14.15	0.01	1
59326.67	4.78	14.20	0.01	6
59327.19	5.30	14.16	0.01	1
59327.35	5.46	14.16	0.02	1
59328.19	6.30	14.17	0.02	1
59328.36	6.47	14.20	0.02	1
59329.18	7.29	14.22	0.02	1
59329.36	7.47	14.20	0.04	1
59330.19	8.30	14.24	0.03	1
59331.68	9.79	14.39	0.01	6
59332.38	10.48	14.37	0.02	1

Table 2 (cont'd)

MJD	Phase (day)	Magnitude (mag)	$\sigma_{\rm Mag}$ (mag)	Telescope
59332.72	10.83	14.44	0.02	6
59333.63	11.74	14.52	0.02	6
59334.28	12.38	14.50	0.01	1
59335.64	13.75	14.71	0.03	3
59336.23	14.34	14.62	0.02	1
59336.54	14.65	14.76	0.03	5
59336.57	14.67	14.77	0.02	3
59337.20	15.31	14.69	0.01	1
59338.15	16.26	14.75	0.01	1
59339.16	17.26	14.81	0.01	1
59339.49	17.60	14.90	0.03	5
59339.50	17.61	14.88	0.03	4
59340.18	18.29	14.86	0.02	1
59341.55	19.66	15.04	0.03	3
59342.19	20.30	14.96	0.03	1
59343.15	21.26	15.03	0.01	1
59343.56	21.66	15.14	0.03	3
59344.16	22.27	15.07	0.02	1
59345.16	23.27	15.11	0.03	1
59346.16	24.27	15.19	0.02	1
59346.55	24.65	15.22	0.03	5
59347.16	25.27	15.24	0.01	1

Table 2 (cont'd)

MJD	Phase (*day*)	Magnitude (*mag*)	$\sigma_{\rm Mag}$ (*mag*)	Telescope
59347.54	25.64	15.29	0.04	5
59347.70	25.81	15.31	0.02	6
59348.16	26.27	15.31	0.01	1
59350.16	28.27	15.43	0.02	1
		R band		
59256.85	-65.04	> 21.19	-	6
59258.78	-63.12	> 22.02	-	6
59259.84	-62.05	> 22.18	-	6
59260.77	-61.13	> 22.32	-	6
59261.72	-60.18	> 22.38	-	6
59262.74	-59.16	> 21.63	-	6
59274.23	-47.66	> 19.11	-	1
59275.28	-46.61	> 19.17	-	1
59276.54	-45.35	> 19.02	-	1
59277.29	-44.61	> 20.51	-	1
59280.29	-41.61	> 20.85	-	1
59283.35	-38.54	> 19.88	-	1
59288.38	-33.52	> 20.52	-	1
59295.15	-26.74	> 20.15	-	1
59298.49	-23.41	> 18.24	-	3
59301.19	-20.70	> 19.79	-	1
59302.21	-19.68	> 19.02	-	1

Table 2 (cont'd)

MJD	Phase (*day*)	Magnitude (*mag*)	σ_{Mag} (*mag*)	Telescope
59303.27	-18.62	> 19.44	-	1
59303.55	-18.34	> 18.57	-	5
59304.18	-17.71	> 19.62	-	1
59305.29	-16.60	18.59	0.09	1
59306.27	-15.62	17.85	0.05	1
59308.20	-13.69	16.75	0.04	1
59308.23	-13.66	16.74	0.04	1
59308.39	-13.50	16.68	0.04	1
59308.65	-13.24	16.54	0.04	4
59309.22	-12.68	16.26	0.05	1
59309.35	-12.55	16.16	0.04	1
59309.49	-12.41	16.20	0.03	3
59309.54	-12.35	16.19	0.03	5
59310.20	-11.69	15.81	0.03	1
59310.29	-11.60	15.77	0.03	1
59310.35	-11.55	15.77	0.03	1
59310.53	-11.36	15.80	0.01	2
59310.64	-11.25	15.71	0.03	4
59310.65	-11.25	15.76	0.01	3
59311.20	-10.69	15.47	0.03	1
59311.35	-10.55	15.42	0.04	1
59311.63	-10.26	15.41	0.03	4

Table 2 (cont'd)

MJD	Phase (*day*)	Magnitude (*mag*)	σ_{Mag} (*mag*)	Telescope
59311.64	−10.26	15.43	0.03	5
59312.17	−9.72	15.19	0.06	1
59312.36	−9.53	15.15	0.04	1
59312.53	−9.36	15.19	0.03	3
59312.73	−9.16	15.12	0.02	6
59313.24	−8.65	14.96	0.03	1
59313.40	−8.49	14.92	0.04	1
59313.57	−8.32	14.99	0.03	5
59313.61	−8.29	15.02	0.02	3
59314.17	−7.72	14.77	0.05	1
59314.38	−7.51	14.76	0.03	1
59314.50	−7.39	14.86	0.03	3
59314.65	−7.24	14.78	0.03	4
59314.66	−7.23	14.87	0.02	3
59315.23	−6.66	14.64	0.04	1
59315.40	−6.49	14.62	0.04	1
59315.66	−6.23	14.66	0.01	6
59316.22	−5.68	14.52	0.06	1
59317.18	−4.71	14.45	0.03	1
59317.29	−4.60	14.44	0.03	1
59317.39	−4.50	14.44	0.03	1
59317.51	−4.38	14.54	0.03	5

Table 2 (cont'd)

MJD	Phase (*day*)	Magnitude (*mag*)	σ_{Mag} (*mag*)	Telescope
59317.59	−4.30	14.52	0.02	2
59318.18	−3.71	14.38	0.03	1
59318.37	−3.53	14.37	0.03	1
59318.49	−3.41	14.48	0.03	2
59318.49	−3.40	14.48	0.03	3
59318.50	−3.40	14.39	0.03	4
59318.51	−3.39	14.48	0.02	5
59318.66	−3.23	14.49	0.02	3
59319.36	−2.53	14.32	0.04	1
59319.49	−2.41	14.35	0.02	4
59319.49	−2.40	14.42	0.03	5
59319.49	−2.40	14.44	0.03	3
59319.60	−2.29	14.45	0.03	3
59319.68	−2.21	14.46	0.02	3
59320.67	−1.22	14.35	0.01	6
59321.19	−0.71	14.23	0.03	1
59321.36	−0.53	14.24	0.03	1
59321.50	−0.40	14.36	0.03	3
59321.57	−0.32	14.37	0.03	2
59321.61	−0.29	14.38	0.03	3
59321.69	−0.20	14.37	0.02	3
59322.19	0.30	14.22	0.04	1

Table 2 (cont'd)

MJD	Phase (*day*)	Magnitude (*mag*)	σ_{Mag} (*mag*)	Telescope
59322.36	0.47	14.22	0.03	1
59322.50	0.60	14.35	0.03	3
59322.56	0.67	14.26	0.03	4
59322.60	0.71	14.36	0.02	3
59322.69	0.79	14.36	0.01	3
59323.20	1.31	14.21	0.04	1
59323.36	1.47	14.21	0.03	1
59323.48	1.59	14.25	0.02	4
59323.49	1.60	14.33	0.03	3
59323.52	1.63	14.34	0.05	2
59323.58	1.69	14.32	0.04	5
59323.66	1.77	14.37	0.02	3
59324.23	2.33	14.43	0.04	1
59324.36	2.47	14.21	0.04	1
59325.20	3.31	14.22	0.03	1
59325.36	3.47	14.23	0.04	1
59326.20	4.31	14.24	0.03	1
59326.36	4.47	14.23	0.03	1
59326.68	4.78	14.33	0.02	6
59327.20	5.30	14.28	0.04	1
59327.36	5.46	14.28	0.04	1
59328.20	6.31	14.31	0.04	1

Table 2 (cont'd)

MJD	Phase (*day*)	Magnitude (*mag*)	σ_{Mag} (*mag*)	Telescope
59328.36	6.47	14.32	0.04	1
59329.19	7.29	14.36	0.05	1
59329.37	7.48	14.37	0.06	1
59330.19	8.30	14.39	0.04	1
59331.69	9.79	14.58	0.02	6
59332.38	10.49	14.56	0.04	1
59332.72	10.83	14.66	0.01	6
59333.64	11.74	14.74	0.01	6
59334.28	12.39	14.70	0.04	1
59335.31	13.42	14.72	0.05	1
59335.65	13.75	14.93	0.02	3
59336.23	14.34	14.82	0.03	1
59336.54	14.65	14.95	0.02	5
59336.57	14.68	14.97	0.02	3
59337.20	15.31	14.86	0.03	1
59338.16	16.27	14.88	0.03	1
59339.16	17.27	14.91	0.03	1
59339.50	17.61	15.03	0.03	5
59339.50	17.61	14.97	0.02	4
59340.18	18.29	14.93	0.04	1
59341.50	19.61	15.00	0.03	4
59341.56	19.66	15.07	0.03	3

Table 2 (cont'd)

MJD	Phase (*day*)	Magnitude (*mag*)	σ_{Mag} (*mag*)	Telescope
59342.19	20.30	14.97	0.04	1
59343.16	21.27	14.97	0.04	1
59343.56	21.67	15.11	0.03	3
59344.16	22.27	14.99	0.03	1
59345.16	23.27	14.99	0.03	1
59346.16	24.27	15.01	0.04	1
59346.55	24.66	15.11	0.04	5
59346.64	24.74	15.11	0.02	2
59347.16	25.27	15.05	0.03	1
59347.50	25.61	15.11	0.03	4
59347.54	25.64	15.16	0.04	5
59347.70	25.81	15.12	0.01	6
59348.16	26.27	15.08	0.03	1
59350.17	28.27	15.15	0.03	1
59351.24	29.35	15.15	0.04	1
		I band		
59308.20	−13.69	17.15	0.06	1
59308.20	−13.69	17.15	0.06	1
59308.26	−13.63	17.13	0.06	1
59308.26	−13.63	17.13	0.06	1
59308.39	−13.50	17.05	0.06	1
59308.39	−13.50	17.05	0.06	1

Table 2 (cont'd)

MJD	Phase (*day*)	Magnitude (*mag*)	σ_{Mag} (*mag*)	Telescope
59308.62	−13.27	17.10	0.03	2
59309.22	−12.67	16.76	0.06	1
59309.22	−12.67	16.76	0.06	1
59309.35	−12.54	16.57	0.06	1
59309.35	−12.54	16.57	0.06	1
59309.49	−12.40	16.68	0.02	3
59310.21	−11.69	16.37	0.07	1
59310.21	−11.69	16.37	0.07	1
59310.32	−11.58	16.23	0.05	1
59310.32	−11.58	16.23	0.05	1
59310.57	−11.33	16.19	0.01	2
59310.66	−11.23	16.21	0.01	3
59311.20	−10.69	15.88	0.06	1
59311.20	−10.69	15.88	0.06	1
59311.35	−10.54	15.76	0.07	1
59311.35	−10.54	15.76	0.07	1
59312.18	−9.71	15.62	0.07	1
59312.18	−9.71	15.62	0.07	1
59312.37	−9.53	15.58	0.06	1
59312.37	−9.53	15.58	0.06	1
59312.54	−9.35	15.59	0.03	3
59313.24	−8.65	15.37	0.05	1

Table 2 (cont'd)

MJD	Phase (*day*)	Magnitude (*mag*)	σ_{Mag} (*mag*)	Telescope
59313.24	−8.65	15.37	0.05	1
59313.41	−8.49	15.37	0.06	1
59313.41	−8.49	15.37	0.06	1
59313.61	−8.28	15.42	0.02	3
59314.18	−7.71	15.21	0.07	1
59314.18	−7.71	15.21	0.07	1
59314.39	−7.51	15.20	0.06	1
59314.39	−7.51	15.20	0.06	1
59314.51	−7.38	15.27	0.02	3
59314.67	−7.22	15.28	0.02	3
59315.23	−6.66	15.09	0.05	1
59315.23	−6.66	15.09	0.05	1
59315.41	−6.49	15.08	0.07	1
59315.41	−6.49	15.08	0.07	1
59317.19	−4.71	14.98	0.05	1
59317.19	−4.71	14.98	0.05	1
59317.31	−4.58	14.95	0.04	1
59317.31	−4.58	14.95	0.04	1
59317.40	−4.49	14.96	0.06	1
59317.40	−4.49	14.96	0.06	1
59318.19	−3.70	14.95	0.06	1
59318.19	−3.70	14.95	0.06	1

Table 2 (cont'd)

MJD	Phase (*day*)	Magnitude (*mag*)	σ_{Mag} (*mag*)	Telescope
59318.37	−3.52	14.95	0.05	1
59318.37	−3.52	14.95	0.05	1
59318.50	−3.39	15.03	0.02	3
59318.50	−3.39	14.92	0.01	2
59318.67	−3.22	15.04	0.02	3
59319.36	−2.53	14.93	0.06	1
59319.36	−2.53	14.93	0.06	1
59319.50	−2.39	15.03	0.03	3
59319.60	−2.29	15.04	0.01	3
59319.69	−2.20	15.04	0.02	3
59321.19	−0.70	14.91	0.05	1
59321.19	−0.70	14.91	0.05	1
59321.37	−0.53	14.93	0.05	1
59321.37	−0.53	14.93	0.05	1
59321.50	−0.39	15.01	0.03	3
59321.58	−0.31	14.95	0.02	2
59321.61	−0.28	15.02	0.03	3
59321.70	−0.19	15.07	0.04	3
59322.20	0.31	14.95	0.05	1
59322.20	0.31	14.95	0.05	1
59322.36	0.47	14.92	0.06	1
59322.36	0.47	14.92	0.06	1

Table 2 (cont'd)

MJD	Phase (*day*)	Magnitude (*mag*)	σ_{Mag} (*mag*)	Telescope
59322.50	0.61	15.05	0.01	3
59322.61	0.71	15.06	0.03	3
59322.69	0.80	15.07	0.02	3
59323.21	1.31	14.96	0.05	1
59323.21	1.31	14.96	0.05	1
59323.37	1.48	14.94	0.05	1
59323.37	1.48	14.94	0.05	1
59323.50	1.61	15.06	0.03	3
59323.54	1.65	14.97	0.03	2
59323.67	1.78	15.08	0.03	3
59324.21	2.31	14.99	0.06	1
59324.21	2.31	14.99	0.06	1
59324.26	2.37	15.01	0.05	1
59324.26	2.37	15.01	0.05	1
59324.37	2.47	14.96	0.05	1
59324.37	2.47	14.96	0.05	1
59325.21	3.31	14.99	0.05	1
59325.21	3.31	14.99	0.05	1
59325.37	3.47	15.01	0.04	1
59325.37	3.47	15.01	0.04	1
59326.20	4.31	15.03	0.05	1
59326.20	4.31	15.03	0.05	1

Table 2 (cont'd)

MJD	Phase (*day*)	Magnitude (*mag*)	σ_{Mag} (*mag*)	Telescope
59326.37	4.47	15.04	0.07	1
59326.37	4.47	15.04	0.07	1
59327.20	5.31	15.07	0.10	1
59327.20	5.31	15.07	0.10	1
59327.36	5.47	15.05	0.06	1
59327.36	5.47	15.05	0.06	1
59328.20	6.31	15.10	0.06	1
59328.20	6.31	15.10	0.06	1
59328.37	6.48	15.12	0.05	1
59328.37	6.48	15.12	0.05	1
59329.19	7.30	15.15	0.07	1
59329.19	7.30	15.15	0.07	1
59329.38	7.48	15.13	0.07	1
59329.38	7.48	15.13	0.07	1
59330.20	8.31	15.19	0.06	1
59330.20	8.31	15.19	0.06	1
59332.39	10.49	15.34	0.07	1
59332.39	10.49	15.34	0.07	1
59334.28	12.39	15.37	0.05	1
59334.28	12.39	15.37	0.05	1
59335.29	13.39	15.40	0.05	1
59335.29	13.39	15.40	0.05	1

Table 2 (cont'd)

MJD	Phase (*day*)	Magnitude (*mag*)	σ_{Mag} (*mag*)	Telescope
59335.34	13.45	15.41	0.05	1
59335.34	13.45	15.41	0.05	1
59335.65	13.76	15.54	0.03	3
59336.24	14.35	15.39	0.06	1
59336.24	14.35	15.39	0.06	1
59336.58	14.69	15.52	0.02	3
59337.21	15.31	15.41	0.05	1
59337.21	15.31	15.41	0.05	1
59338.16	16.27	15.43	0.05	1
59338.16	16.27	15.43	0.05	1
59339.17	17.27	15.36	0.06	1
59339.17	17.27	15.36	0.06	1
59340.19	18.30	15.38	0.07	1
59340.19	18.30	15.38	0.07	1
59341.25	19.36	15.35	0.09	1
59341.25	19.36	15.35	0.09	1
59341.31	19.42	15.35	0.07	1
59341.31	19.42	15.35	0.07	1
59341.56	19.67	15.40	0.02	3
59342.20	20.31	15.30	0.07	1
59342.20	20.31	15.30	0.07	1
59343.16	21.27	15.29	0.07	1

Table 2 (cont'd)

MJD	Phase (*day*)	Magnitude (*mag*)	σ_{Mag} (*mag*)	Telescope
59343.16	21.27	15.29	0.07	1
59343.57	21.68	15.37	0.03	3
59344.17	22.28	15.25	0.06	1
59344.17	22.28	15.25	0.06	1
59345.17	23.28	15.21	0.06	1
59345.17	23.28	15.21	0.06	1
59346.17	24.28	15.21	0.06	1
59346.17	24.28	15.21	0.06	1
59347.17	25.28	15.18	0.06	1
59347.17	25.28	15.18	0.06	1
59348.17	26.28	15.21	0.04	1
59348.17	26.28	15.21	0.04	1
59350.17	28.28	15.13	0.05	1
59350.17	28.28	15.13	0.05	1
59351.21	29.32	15.19	0.07	1
59351.21	29.32	15.19	0.07	1
59351.27	29.38	15.18	0.04	1
59351.27	29.38	15.18	0.04	1

Appendix C

Early color evolution of SN 2021hpr: Other results

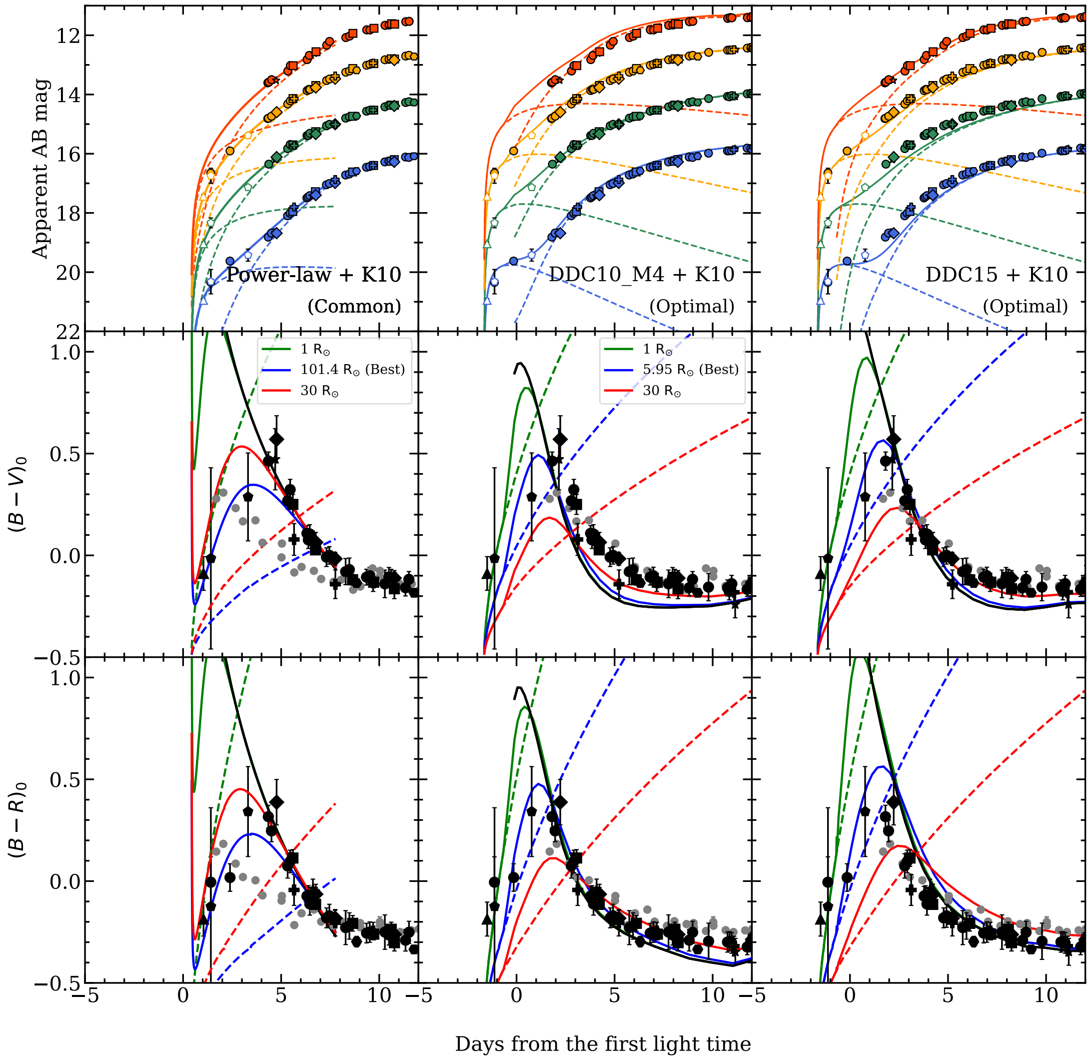

Figure C.1. Same as Figure 6 with different configurations. (Left column) Companion+power-law fit, but note that it is for a common viewing angle. Since the first light time is slightly earlier, the very early part of model lines is plotted in rapidly red-warded but its value is within the error. (Middle & right columns) It is other results for the optimal viewing angle using DDC10_M4 (middle) and DDC15 model (right).

요 약

Ia형 초신성은 항성 진화의 마지막 단계에서 나타나는 폭발 현상의 하나로, 그 원형별은 백색왜성으로 알려져 있다. 백색왜성의 탄소 핵이 열핵융합 폭발에 의하여 붕괴되면서 철보다 무거운 원소들을 만들며, 광도 곡선은 니켈56과 같은 철계열 원소들의 방사성 붕괴로부터 나오는 에너지를 원천으로 밝아진다. 폭발 과정에서 핵합성은 초신성 원형별의 주변 환경의 원소 함량을 풍부하게 하며, 별탄생과 은하 진화까지 이끈다. 특히, Ia형 초신성은 표준 광원의 좋은 후보 천체로서 먼 천체까지의 거리를 측정하는 "거리 측정자"로서 표준 우주론의 검증에도 중요한 역할을 해왔다. 그러나, Ia형 초신성의 원형별계가 무엇인지에 대하여 여전히 분명하지 않다. 현재 대립 중인 주된 원형별계의 모형으로는 백색왜성과 비축퇴 동반성의 근접 쌍성계(단일 축퇴 모형)와 백색왜성 쌍성계(이중 축퇴 모형)가 있다. 이 모형들을 구분하는 한가지 방법은 폭발 초기에 초신성 분출물과 동반성 표면과의 충돌(동반성 모형)로 발생한다고 예측되는 "충격파-가열 냉각 복사" 현상의 흔적을 검출하는 것이다. "근거리 은하들의 집중 모니터링 탐사 (Intensive Monitoring Survey of Nearby Galaxies; IMSNG)"는 이러한 충격파-가열 냉각 복사를 검출하기 위해 10대 이상의 소형 망원경의 네트워크인 "소형망원경 네트워크 (소망넷)"를 활용하여 하루 이내의 매우 짧은 간격의 시계열 관측을 수행해왔다. 본 학위 연구에서는 먼저 소형 망원경 네트워크 시스템을 개선하기 위하여 추가적인 망원경 시스템을 구축하였고, 그 특성과 성능을 조사한 내용을 기술한다. 다음으로, IMSNG 탐사에서 폭발 초기에 관측한 초신성들 중 두 개의 Ia형 초신성인 SN 2019ein과 SN 2021hpr의 초기 광도 곡선 분석 결과를 제시한다.

첫번째 연구는 2020년 3월 칠레 딥스카이칠레 관측소에 설치한 0.36미터 고등과학원 참눈 망원경(KCT)의 자동화 관측과 성능을 소개한다. KCT의 목적은 어두운 칠레 하늘을 이용하고, 다른 소형 망원경과 함께남반구에서의 관측 간격을 더 촘촘히 함으로써 변광 천체들을 중심으로 시계열 관측을 수행하는 것이다. KCT는 "관측소 제어판 (ACP)"으로 불리는 상용 소프트웨어를 사용하여 관측자가 미리 업로드한 스크립트를 기반으로 스케쥴링 관측을 수행해준다. 지금까지의 관측 이미지들은 약간 늘어나있기는 하지만 시야각 ($49\farcm4 \times 49\farcm4$) 전반에 걸쳐 균일한 점퍼짐함수(PSF)를 보여주며, 매우 짧은 노출 시간에서도 셔터 패턴의 영향을 받지 않았다. 또한 약한 달빛 영향 하에 맑은 하늘(3초 시상)에서 10분의 노출시간으로 얻은 g 필터 이미지에 대한 5시그마 한계 등급은 18.9 AB등급으로 계

산되었다. KCT 시스템 운영에 있어 관측 계획을 개량하여, 앞으로 변광천체를 더 빠르게 후속 관측하는 방향으로 개선하고자 한다.

두번째 연구에서는 IMSNG에서 관측한 일반적이나 약간 어두운 Ia형 초신성인 SN 2019ein의 광학/근적외선 광도 곡선을 분석한 결과를 제시하고, 원형별계에 대하여 논의하였다. NGC 5353은 IMSNG 프로그램의 관측 타겟인 NGC 5350과 함께 있는 천체이므로, SN 2019ein의 폭발 초기 자료를 얻을 수 있었다. 초기광도곡선에서는 충격파-가열 냉각 복사의 흔적이 보이지 않았으며, 동반성 모형에 단순멱함수를 결합한 적합 분석 결과, 동반성의 크기는 태양 반경의 약 1.0배이었다. 이러한 결과는 해당 초신성의 동반성으로 적색거성과 같은 큰 항성은 배제할 수 있는 것이다. 색지수 변화에서도 초기에 푸른 색을 보이지 않았으며, 얇은 헬륨 껍질을 갖는 백색왜성에서의 폭발 모형인 이중 폭발 모형과도 상반되는 관측 결과였다.

세번째 연구는 NGC 3147 은하에서 발생한 일반적인 Ia형 초신성인 SN 2021hpr의 초기 광도 곡선과 추가적인 자료 분석 결과를 제시한다. 이 초신성에서 가장 흥미로운 부분은 초기 광도 곡선의 푸른색의 뚜렷한 초기 초과 현상이었다. 이를 동반성 모형으로부터 기인한 충격파-가열 냉각 복사로 간주했을 때 동반성의 크기는 약 6 태양반경의 항성으로 발생한 것으로 생각할 수 있다. 추가적으로 폭발 이전에 깊게 촬영된 허블 우주 망원경의 고분해능 이미지에서는 원형별계가 발견되지 않았다. 이미지의 관측 한계 등급으로부터 적어도 원형별계가 태양 질량의 12배보다 가벼운, 즉 태양 반경의 300배보다는 작을 것으로 추정할 수 있었다. 또한 폭발 당시 분출물에 의하여 벗겨진 동반성 표면의 물질이 폭발 200일 이후 후기 성운상 단계에서 Hα 방출선으로 검출될 것이라 예측된다. 그러나 맥도날드 천문대 하비-에벌리 망원경(Hobby-Eberly Telescope; HET)의 긴슬릿 관측 자료에서는 동반성의 벗겨진 물질의 흔적이 관측되지 않았다. 이것은 앞서 초기 광도 곡선 연구와 상반되는 결과이다. 여러 설명들 중 약한 초신성 폭발 에너지이기 보다는 오히려 주성과 동반성 간의 거리가 멀면 벗겨지는 물질의 질량이 작을 가능성으로 단일 축퇴 모형에서도 이러한 미검출이 설명 가능해 보인다. 본 연구의 결과는 다른 원형별계의 가능성도 시사하는데, 일부 이중 폭발 모형에서는 폭발 초기에 보이는 붉은 색지수의 봉우리를 설명할 수 있으나, 최대 밝기 이후의 B-밴드에서의 광도 곡선이 너무 빠르게 어두워지는 부분과 맞지 않는다. 또한 니켈56이 분출물에 과도하게 분포한 경우도 하나의 가능성이 될 수 있으나, 매우 붉은 ($B - V > 1$) 색지수 봉우리를 만드는 B-밴드 플럭스 강하가 SN 2021hpr에서는 보이지

않는다. 이중 축퇴 모형에서는 동반성 물질의 원반을 가지고 있는 백색왜성이 폭발하면서 푸른 초기 초과를 방출하는 모형이 가능할 것으로 보인다. 앞으로의 더 구체적인 모형을 이용한 후속 연구가 SN 2021hpr의 특이한 초기 측광학적 특성을 설명할 수 있을 것이며, 이러한 SN 2021hpr의 특성은 다양한 초신성 원형별계 모형을 검증하는 데에 좋은 표본이 된다.

본 학위 연구의 결론의 요약은 다음과 같다.

다수의 소형 망원경 이용한 짧은 간격의 관측은 여전히 초신성의 초기 광도 곡선을 얻는 데에 강력한 방법이다. IMSNG 탐사에서 얻은 Ia형 초신성의 초기 광도 곡선은 현재까지 제안된 초신성의 원형별계 모형들을 검증하는 데에 중요한 관측적 증거를 제공한다. Ia형 초신성의 원형별계에서 반경이 큰 (적색거성, 적색초거성) 항성은 기존에 알려져 있던 것과 다르게 동반성으로서 매우 제한적으로 가능해 보인다. 이것은 초기 초과 현상을 갖는 Ia형 초신성이 적고, 후기 성운상 단계에서 수소 방출선이 거의 관측되지 않는 점으로 알 수 있다. 본 학위 논문의 결과도 분리각이 매우 클 때의 적색거성 동반성의 가능성을 열어두었으나, 이전 연구 결과들을 지지한다고 할 수 있다.

앞으로의 IMSNG 관측에 대하여 한계등급을 조금 더 깊게($R \sim 20.4\,AB$)한다면, 단일 축퇴 모형과 이중 축퇴 모형을 더 명확히 구분할 수 있을 것이다. $0.1\,R_{\odot}$ 크기의 항성으로부터 발생하는 가열 냉각 복사의 최대 광도는 $R \sim -12$등급으로 훨씬 어둡지만, 가까운 ($D < 30\,Mpc$) 표본에 대하여 $R \sim 20.4\,\mathrm{AB}$ 등급의 한계등급에 도달함으로써 가능할 것이다.

특히 초기 초과 현상이 관측된 초신성의 경우, 색지수, 스펙트럼, 고분해능 딥 이미징과 같은 추가적인 자료들이 이러한 모형들을 구분하는 데에 있어 필수적이라고 할 수 있다. 여기에 제임스 웹 우주 망원경, 루빈 천문대, 거대마젤란망원경과 같은 차세대 대형 망원경의 고분해능 이미지와 소형 망원경의 빠른 후속 관측은 Ia형 초신성과 다른 변광천체들의 원형별계의 본질을 이해하는 데에 더 많은 시너지 효과를 가져올 수 있다.

주요어: 은하: 거리와 적색이동 – 초신성:일반 – 초신성:개별 (SN 2019ein) – 초신성:개별 (SN 2021hpr) – 방법론:관측 – 망원경 – 기술:측광

학 번: 2015-20364